2020

Assessment of White Matter Hyperintensity, Cerebral Blood Flow, and Cerebral Oxygenation in Older Subjects Stratified by Cerebrovascular Risk

Ahmed A. Bahrani
University of Kentucky, ahmed.bahrani@uky.edu
Author ORCID Identifier:
https://orcid.org/0000-0003-1809-0879
Digital Object Identifier: https://doi.org/10.13023/etd.2020.140

STUDENT AGREEMENT:

I represent that my thesis or dissertation and abstract are my original work. Proper attribution has been given to all outside sources. I understand that I am solely responsible for obtaining any needed copyright permissions. I have obtained needed written permission statement(s) from the owner(s) of each third-party copyrighted matter to be included in my work, allowing electronic distribution (if such use is not permitted by the fair use doctrine) which will be submitted to UKnowledge as Additional File.

I hereby grant to The University of Kentucky and its agents the irrevocable, non-exclusive, and royalty-free license to archive and make accessible my work in whole or in part in all forms of media, now or hereafter known. I agree that the document mentioned above may be made available immediately for worldwide access unless an embargo applies.

I retain all other ownership rights to the copyright of my work. I also retain the right to use in future works (such as articles or books) all or part of my work. I understand that I am free to register the copyright to my work.

REVIEW, APPROVAL AND ACCEPTANCE

The document mentioned above has been reviewed and accepted by the student's advisor, on behalf of the advisory committee, and by the Director of Graduate Studies (DGS), on behalf of the program; we verify that this is the final, approved version of the student's thesis including all changes required by the advisory committee. The undersigned agree to abide by the statements above.

Ahmed A. Bahrani, Student

Dr. Guoqiang Yu, Major Professor

Dr. Sridhar Sunderam, Director of Graduate Studies

ASSESSMENT OF WHITE MATTER HYPERINTENSITY, CEREBRAL BLOOD FLOW, AND CEREBRAL OXYGENATION IN OLDER SUBJECTS STRATIFIED BY CEREBROVASCULAR RISK

DISSERTATION

A dissertation submitted in partial fulfillment of the
requirements for the degree of Doctor of Philosophy in the
College of Engineering
at the University of Kentucky

By
Ahmed Ali Bahrani
Lexington, Kentucky
Director: Dr. Guoqiang Yu, Professor of Biomedical Engineering
Lexington, Kentucky
2020

https://orcid.org/0000-0003-1809-0879

ABSTRACT OF DISSERTATION

ASSESSMENT OF WHITE MATTER HYPERINTENSITY, CEREBRAL BLOOD FLOW, AND CEREBRAL OXYGENATION IN OLDER SUBJECTS STRATIFIED BY CEREBROVASCULAR RISK

Objective: Cerebrovascular disease (CVD) is the fifth most common cause of mortality in the United States. Diagnosis of CVD at an early stage is critical for optimal intervention designed to prevent ongoing and future brain injury. CVD is commonly associated with abnormalities of the cerebral microvasculature leading to tissue dysfunction, neuronal injury and death, and resultant clinical symptoms, which in turn, further impacts cerebral autoregulation (CA). This series of studies aims to test the hypothesis that white matter hyperintensities (WMH) and cerebral hemodynamics (quantified by magnetic resonance imaging (MRI) and an by innovative hybrid near-infrared diffuse optical instrument) can be used as biomarkers to distinguish cognitively healthy older subjects with high or low risk for developing CVD.

Methods: Using functional MRI, WMH and cerebral blood flow (CBF) were quantified in 26 cognitively healthy older subjects (age: 77.8 ± 6.8 years). In a follow-up study, significant variability in WMH quantification methodology was addressed, with sources of variability identified in selecting image center of gravity, software compatibility, thresholding techniques, and manual editing procedures.

Accordingly, post-acquisition processing methods were optimized to develop a standardized protocol with less than 0.5% inter-rater variance. Using a novel laboratory-made hybrid near-infrared spectroscopy/diffuse correlation spectroscopy (NIRS/DCS) and a finger plethysmograph, low-frequency oscillations (LFOs) of CBF, cerebral oxygenation, and main arterial pressure (MAP) were simultaneously measured before, during, and after 70° head-up-tilting (HUT). Gains (associated with CAs) to magnify LFOs were determined by transfer function analyses with MAP as the input and cerebral hemodynamic parameters as the outputs. In a follow-up study, a fast software correlator for DCS and a parallel detection technique for NIRS/DCS were adapted to improve the sampling rate of hybrid optical measurements. In addition, a new DCS probe was developed to measure CBF at the occipital lobe, which represents a novel application of the NIRS/DCS technique.

Results: MRI measurements demonstrate that deep WMH (dWMH) and periventricular WMH (pWMH) volumetric measures are associated with reduced regional cortical CBF in patients at high-risk of CVD. Moreover, CBF in white matter (WM) was reduced in regions demonstrating both pWMH and dWMHs. NIRS/DCS optical measurements demonstrate that at resting baseline, LFO gains in the high-risk group were relatively lower compared to the low-risk group. The lower baseline gains in the high-risk group may be attributed to compensatory mechanisms that allow the maintenance of a stronger steady-state CA. However, HUT resulted in smaller gain reductions in the high-risk group compared to the low-risk group, suggesting weaker dynamic CA in association with increased CVD risks. A noteworthy finding in these experiments was that CVD risk more strongly influenced CBF than cerebral oxygenation.

Conclusions: Regional WMH volumes, cortical and WM CBF values, and LFO gains of cerebral hemodynamics demonstrate specific associations with CA and may serve as important potential biomarkers for early diagnosis of CVD. The high spatial resolution, large penetration depth, and variety of imaging-sequences afforded by MRI make it an appealing imaging modality for evaluation of CVD, although MRI is costly, time-limited, and requires transfer of subjects from bed to imaging facility. In contrast, low-cost, portable, mobile diffuse optical technologies provide a complementary alternative for early screening of CVD, that can further allow continuous monitoring of disease attenuation or progression at the subject's bedside. Thus, development of both methodologies is essential for progress in our future understanding of CVD as a major contributor to the morbidity and mortality associated with CVD today.

KEYWORDS: Near-infrared Spectroscopy/Diffuse Correlation Spectroscopy, Magnetic Resonance Imaging, Cerebrovascular Diseases, White Matter Hyperintensities, Low-Frequency Oscillation, Cerebral Blood Flow and Oxygenation.

Ahmed Ali Bahrani

04/15/2020

ASSESSMENT OF WHITE MATTER HYPERINTENSITY, CEREBRAL BLOOD FLOW, AND CEREBRAL OXYGENATION IN OLDER SUBJECTS STRATIFIED BY CEREBROVASCULAR RISK

By
Ahmed Ali Bahrani

Dr. Guoqiang Yu
Director of Dissertation

Dr. Sridhar Sunderam
Director of Graduate Studies

04/15/2020
Date

DEDICATION

To the memory of my father, and to my mother, wife, children, sisters and brothers.

ACKNOWLEDGMENTS

First, I would like to thank my advisor, Dr. Guoqiang Yu, for his constant guidance and invaluable mentorship with valuable feedback throughout my graduate education in developing and applying near-infrared diffuse optical technologies in human subjects. I would also like to thank Dr. Gregory A. Jicha for all his tremendous supports and guidance for doing my neuroimaging research on the aging population. Also, I am grateful for the scholarship that he provided me to finalize my Ph.D. study.

Especial thanks to Drs. Charles D. Smith and David K. Powell for the time and effort that they spent on training and guiding me in the track of neuroimage analysis.

I am also grateful to the complete Dissertation Committee, and the external examiner, respectively: Drs. Abhijit Patwardhan, Sridhar Sunderam, Yang Jiang, Gregory Jicha, and Damodar Pokhrel.

I would like to acknowledge Dr. Donna Wilcock and Dr. Brian Gold for their supports and advice. Also, I would acknowledge my lab mates for the wonderful collaboration and friendship during the time that I have spent with them, especially Drs. Yu Shang, Chong Huang, Mingjun Zhao, and Daniel Irwin.

Also, I would like to acknowledge Dr. Arjun's lab (University of Pennsylvania) for providing me the original code of the fast software correlator.

I gratefully acknowledge my sponsor, the Higher Committee for Education Development in Iraq (HCED).

I acknowledge the partial funding from the National Institutes of Health (NIH): UH2-NS100606 (2016 - 2018), R01-NR014189 (2012 - 2017), R01-AG042419 (2013 - 2016), P30-AG028383 (2017), 5P30-AG028383 (2013 - 2014), 1R21-HD091118-01A1

(2018 - 2020), 3R21-HD091118-02S1 (2019 - 2021), 1R21-AR062356 (2012), and 1R01-AG062480 (2019 - 2024), American Heart Association (AHA): 16GIA30820006 (2016 - 2019) and National Science Foundation (NSF): EPSCoR-1539068 (2015 - 2020). The content herein is solely the responsibility of the author(s) and does not necessarily represent the official views of the NIH, AHA, NSF or EPSCoR.

I would like to thank my family, especially my mother, my wife, and my children (Abdullah and Ayman) for their supports, love, and being patient with me to finish my degree.

Thanks for the participants who gave their time and effort to participate in the studies of this project.

TABLE OF CONTENTS

LIST OF TABLES

LIST OF FIGURES

CHAPTER 1. INTRODUCTION

1.1 Cerebrovascular Disease (CVD)

Cerebrovascular disease (CVD) is a global term for cerebrovascular injuries that may arise from a variety of different causes. CVD in the aging population is most commonly due to cerebral small vessel ischemic disease (CSVD), although both lacunar and large vessel ischemic infarcts contribute significantly as well as microvascular infarcts, cerebral amyloid angiopathy, and overt subcortical and cortical hemorrhagic stroke [1]. CVD is the fifth most common cause of mortality in the United States (0.14 million in 2017) [2, 3], and the second worldwide (17.6 million in 2016) [4]. Risk factors for CVD include aging, atherosclerosis, smoking, hypertension, high cholesterol, and diabetes, among others [5-8]. Advanced age represents the major risk factor for the development of CVD, irrespective of cause [9]. The present dissertation will focus on the development of new and refined biomarkers to detect CSVD, which is a major cause of the cognitive decline and loss of function in the aging population today [10].

CSVD is a general term that refers to injury affecting the cerebral arterioles, venules, capillaries, and small vessels through a variety of pathological processes. These pathological processes are thought to contribute to approximately 45% of the total burden of dementia seen in the aging population today [11]. CSVD is considered the most prevalent cause for the development of vascular dementia, which is regarded as the second most common type of dementia in the United States [12, 13] after Alzheimer's disease (AD) according to the Alzheimer's Association (https://www.alz.org/alzheimers-dementia/what-is-dementia). Cerebral blood flow (CBF) impairment, cerebral microbleeds, micro-and other small vessel infarcts, and lacunar infarctions, all lead to

increased white matter hyperintensities (WMH) seen on magnetic resonance imaging (MRI) derived T2 sequences. Beta-amyloid, associated with the development of AD, can also lead to vascular abnormalities via aggregation within small vessels and capillaries that may be responsible for some of the WMH seen in routine imaging studies suggesting that CSVD may not be due solely to traditional cerebrovascular disease risk factors (**Fig. 1-1**).

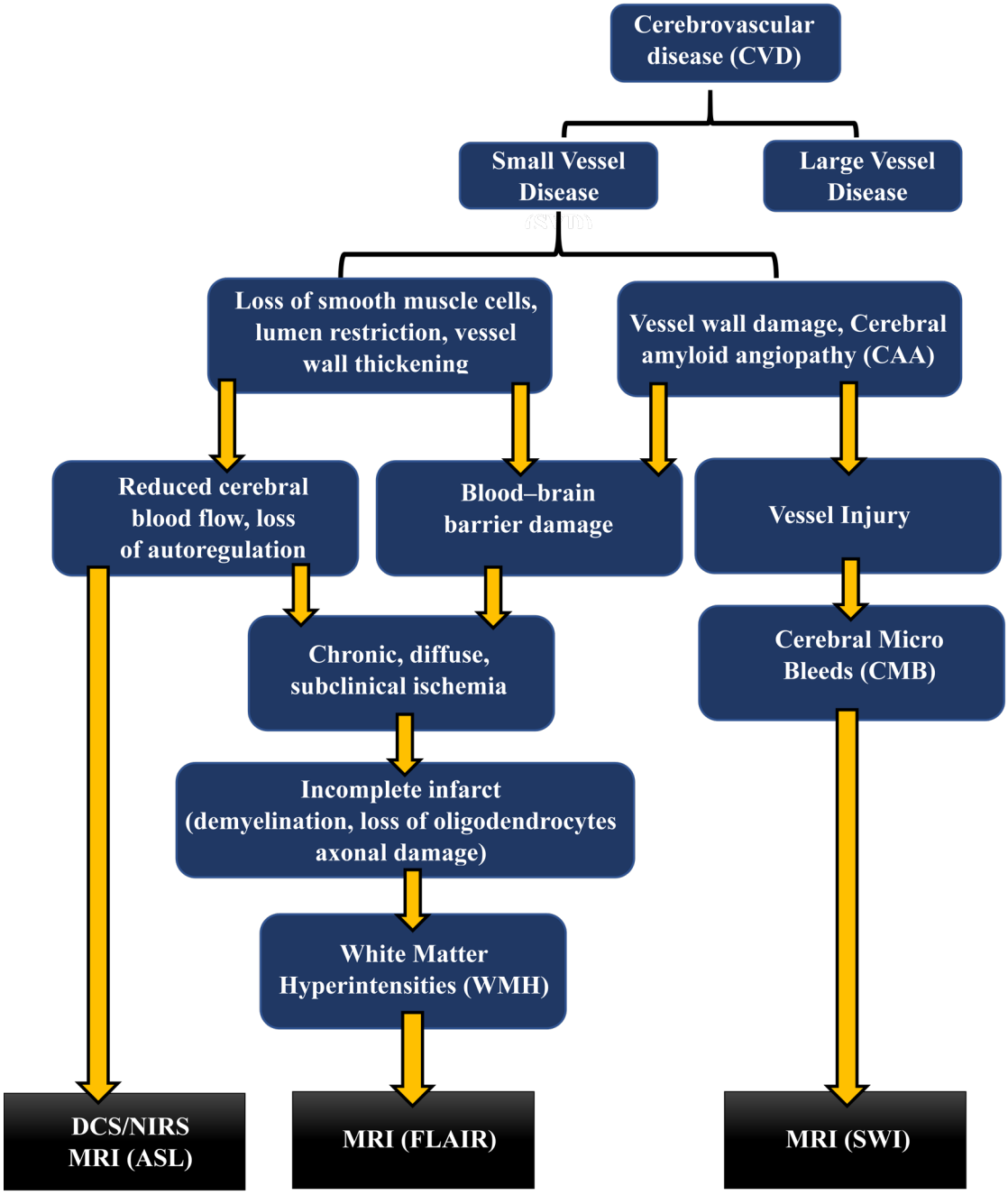

Figure 1-1: A schematic diagram focuses on the pathogenesis of CSVD that results in irreversible brain injury.

This diagram is modified from the prior work of Leonardo Pantoni [1]. The cartoon diagram highlights the leading causes of cerebral autoregulation failure, with resultant WMH, and microbleeds, and the techniques that were used in these studies (black blocks).

1.2 Noninvasive Diagnosing Techniques for Cerebral Small Vessel Disease

The diagnosis of CSVD in its earliest stage is considered critical in regard to the timing of interventions that may prevent further complications. Ideal diagnostic tests should be noninvasive, low-cost, and have high diagnostic accuracy for CSVD even in the earliest clinical or preclinical stages of the disease. Several techniques have been used to study CSVD. Alternative means to assess CSVD include pathological assays that may be invasive, as they are dependent on the collection of blood or cerebral spinal fluid (CSF) [14].

Neuroimaging is a critical tool for diagnosing neurodegenerative disease states [15], such as vascular dementia and Alzheimer's disease. WMH can be visualized through MRI imaging sequences and CT-scan although MRI with fluid attenuated inversion recovery (FLAIR) sequence has a higher contrast [16]. Moreover, CT-scan has noise artifacts at the regions that close to the bone structures as well as the ionized radiation risk issue [17]. Thus, MRI is more recommended than CT-scan for diagnosing WMH lesions.

CBF can be quantified using a wide range of techniques including positron emission tomography (PET) [18], single positron emission computed tomography (SPECT) [19], and noninvasive arterial-spin-labeling (ASL) MRI [20]. Although PET and SPECT techniques are considered gold standard techniques for imaging CBF [21, 22], both require injection of a radioactive contrast agent that has side effects [18, 19].

Transcranial Doppler ultrasound (TCD) has been used to measure cerebral blood flow velocity (CBFV) in major arteries, which may not be consistent with CBF in the microvasculature [23]. Moreover, TCD cannot be performed in ~10% of subjects who do not have adequate acoustic windows [24].

Spectral techniques have been used for the detection of CSVD, including diffusion correlation spectroscopy (DCS) for CBF measurement [25, 26], and near-infrared spectroscopy (NIRS) for cerebral oxygenation measurement [27]. Since CBF and cerebral blood oxygenation are usually coupled and interactive, it is desirable to measure both quantities and investigate their complicated relationship.

In summary, the high spatial resolution, large penetration depth, and variety of imaging-sequences afforded by MRI make it an appealing imaging modality for evaluation of CSVD, although MRI is costly, time-limited, and requires transfer of subjects from bed to imaging facility. In contrast, low-cost, portable, mobile NIRS/DCS diffuse optical technologies provide a complementary alternative for early screening of CSVD, that can further allow continuous monitoring of disease attenuation or progression at the subject's bedside. Thus, development of both methodologies is essential for progress in our understanding of CSVD as a major contributor to the morbidity and mortality associated with CVD.

1.3 Chapter Organization

This dissertation consists of six chapters that are organized as follows:

Chapter 1 presents an introduction to basic concepts necessary to understand CVD and the historical context and techniques that have been used for diagnosing and studying CSVD.

Chapter 2 presents a study with functional MRI that aims to add clarity to the relationship between deep and periventricular brain WMHs, CBF, and cerebrovascular risk in older persons. Deep and periventricular WMHs and regional gray matter (GM) and white matter (WM) blood flow from arterial spin labeling were quantified from MRI scans

of 26 cognitively normal older subjects stratified by CVD risk. FLAIR images were acquired using a high-resolution 3-dimensional (3D) sequence that reduced partial volume effects seen with slice-based techniques. Deep WMHs but not periventricular WMHs were increased in patients at high risk of CVD; periventricular WMHs but not deep WMHs were associated with decreased regional cortical GM blood flow. We also found that blood flow in WM was decreased in regions of both periventricular WMH and deep WMH, with a greater degree of decrease in periventricular WMH areas. WMHs are usefully divided into deep WMH and periventricular WMH regions because they demonstrate differential associations with the experimental variables studied and have discrete implications for human disease related to CVD risks. We conclude that 3D regional WMH volume is a potentially valuable marker for CSVD based on the demonstrated associations with cortical and WM CBF.

Chapter 3 focuses on methodologic improvements for the post-processing volumetric analytic protocols that were introduced in **Chapter 2**. Disparate research sites using identical or near-identical MRI acquisition techniques often produce results that demonstrate significant variability regarding volumetric quantification of WMH in the aging population. The sources of such variability have not previously been fully explored. 3D FLAIR sequences from a group of randomly selected aged subjects were analyzed to identify sources-of-variability in post-acquisition processing that can be problematic when comparing WMH volumetric data across disparate sites. The methods developed focused on standardizing post-acquisition protocol processing methods to develop a protocol with less than 0.5% inter-rater variance. A series of experiments using standard MRI acquisition sequences explored post-acquisition sources-of variability in the quantification of WMH

volumetric data. Sources-of-variability included: the choice of image center, software suite and version, thresholding selection, and manual editing procedures (when used). Controlling for the identified sources-of-variability led to a protocol with less than 0.5% variability between independent raters in post-acquisition WMH volumetric quantification. Comparison with existing method(s): Post-acquisition processing techniques can introduce an average variance approaching 15% in WMH volume quantification despite identical scan acquisitions. Understanding and controlling for such sources-of-variability can reduce post-acquisition quantitative image processing variance to less than 0.5%. Considerations of potential sources-of-variability in MRI volume quantification techniques and reduction in such variability is imperative to allow for reliable cross-site and cross-study comparisons.

Chapter 4 presents a low-frequency oscillation (LFO) method to test whether the cerebral autoregulation (CA) can be used as a biomarker to distinguish two groups of cognitively intact older adults with high or low risk for developing CVD. A novel hybrid near-infrared diffuse optical instrument and a finger plethysmograph were used to simultaneously detect LFOs of CBF, oxy-hemoglobin concentrations ([HbO_2]), and deoxy-hemoglobin concentrations ([Hb]), and main arterial pressure (MAP) in older adults before, during, and after 70° head-up-tilting (HUT). LFOs were quantified in 4 frequency intervals: I (0.005-0.0095 Hz), II (0.0095-0.02 Hz), III (0.02-0.07 Hz), and IV (0.07-0.2 Hz). The LFO transfer function gains were determined by transfer function analyses with MAP as the input, and CBF, [HbO_2] and [Hb] as the outputs. In general, CAs correlate inversely with LFO gains. At resting baseline, LFO gains in the high-risk group (n = 11) were relatively lower compared to the low-risk group (n = 13). Particularly at Interval-IV,

intergroup gain differences reached significance for all measured cerebral variables (CBF, [HbO_2] and [Hb]). The lower baseline gains in the high-risk group may attribute to compensatory mechanisms to maintain stronger steady-state CAs. However, HUT resulted in smaller gain reductions at Interval-III and Interval-IV in the high-risk group compared to the low-risk group, suggesting weaker dynamic CAs. In addition, cerebrovascular risk was a stronger predictor of CBF than of [HbO_2] and [Hb]. Cerebrovascular risk affects neurogenic and myogenic activities (Interval III and Interval-IV) more than endothelial activities (Interval-I and Interval-II). LFO gains are potentially valuable biomarkers for early detection of CSVD based on associations with CAs.

Chapter 5 focuses on the methodologic improvements of NIRS/DCS techniques that were presented in **Chapter 4.** The improved NIRS/DCS technologies with parallel detection, high sampling rates, and new probe design allow us, for the first time, to measure both CBF and cerebral oxygenation at frontal and occipital lobes in two order subjects.

Chapter 6 presents a summary of this dissertation and points out future perspectives. This thesis includes a diverse set of work and experiments with a primary focus on improving optical measurement techniques and developing MRI post-processing imaging protocols that maximize our potential for the future study of CSVD.

Overall, the main focus of this dissertation was to test whether WMH and cerebral hemodynamics quantified respectively by the MRI and hybrid NIRS/DCS can be used as biomarkers to distinguish two groups of cognitive healthy older subjects who evaluated as high or low risk for developing CVD. We demonstrated WMH volumes based on associations with cortical and WM CBF values and LFO gains of cerebral hemodynamics based on associations with CAs are potential biomarkers for early detection of CVD.

CHAPTER 2. WHITE MATTER HYPERINTENSITIES ASSOCIATIONS WITH CEREBRAL BLOOD FLOW IN OLDER SUBJECTS STRATIFIED BY CEREBROVASCULAR RISK

2.1 Introduction

Cerebrovascular disease (CVD) is a common medical morbidity in the United States, with high rates of disability through stroke and dementia [28, 29]. Detection and characterization of existing cerebrovascular disease, therefore, remains an important medical issue. An understudied aspect of cerebrovascular disease is the relationship between cerebral blood flow (CBF) and white matter hyperintensities (WMH, [30, 31]). WMH are periventricular and deep regions of abnormal signal commonly seen on MRI scans of older and high vascular risk patients [32, 33]. It has been found that WMH embody an ischemic component with functional consequences including cognitive decline and dementia, but due to the underlying complexity of these lesions a full formulation of their significance has not been achieved [34, 35]. In this study we analyzed the relationship between WMH and CBF in subjects stratified by cerebrovascular risk. The aim of this study was to find relationships between WMH, CBF and CSVD risk, expecting that WMH would increase with increased CSVD risk and with decreased CBF.

2.2 Materials and Methods

2.2.1 Participants

Twenty-six healthy subjects were recruited by the Center for Clinical and Translational Science (CCTS) and the Sanders-Brown Center on Aging at the University of Kentucky. Written consent was obtained from each individual before participation

Published Study: Bahrani et.al, Journal of Stroke and Cerebrovascular Diseases, 26 (4), 779–786 (2017)

according to an approved protocol from the Institutional Review Board (IRB) at the University of Kentucky.

A CVD risk score, based on Framingham risk estimation modified for stroke prediction [36], was assigned to each patient by study neurologists. The Framingham study risk score is based on several parameters, e.g., gender, age, history of diabetes, blood pressure, smoking history, and cholesterol level, and used to predict CVD over ten years for each subject. The Framingham scoring scale range is 1 - 30 points. Subjects were divided, based on their risk score, into two groups: high-risk (n = 12) and low-risk (n = 14) for CVD, based on a cutoff of 15 points. Image analysis was blind to age and CVD risk status.

2.2.2 MRI Acquisition

A Siemens 3T TIM Trio MRI scanner at the University of Kentucky magnetic resonance imaging and spectroscopy center (MRISC) equipped with a 32-channel head coil was used to scan subjects. Acquisition sequences were: (1) T1-weighted magnetization-prepared rapid acquisition gradient echo (MPRAGE), echo time (TE) 2.3 ms, repetition time (TR) 2530 ms, inversion recovery time (IR) 1100 ms, flip angle (FA) is 7º, 1 x 1 x 1 mm resolution full brain coverage (2) Fluid attenuated inversion recovery (FLAIR), TE 388 ms, TR 6000 ms, IR is 2200 ms, 3D 1 x 1 x 1 mm with no gap between slices, and (3) Pulsed arterial-spin-labeling (PASL) TE 12 ms, TR 3400 ms, IR_1 700 ms, IR_2 1900 ms, 4 x 4 x 4 mm resolution with 1 mm gap between slices, full brain coverage excluding the cerebellum.

2.2.3 Image Processing

MRI image processing used semi-automated methods to quantitate regional WMH volume and CBF flow values. These methods are summarized in **Fig 2-1**. Two images were registered and averaged to increase the signal-to-noise ratio. Scalp and bone tissue were stripped using the FSL FMRIB software library (FSL v5.0.8) Brain extraction tool (BET) (http://fsl.fmrib.ox.ac.uk/fsl/fslwiki/BET). Slice by slice cleanup of unwanted tissue was performed using the medical image processing analysis and visualization (MIPAV v7.2.0) application (http://mipav.cit.nih.gov). The stripped brain image was converted to a mask by thresholding (brain mask). FLAIR and PASL images were registered to the image in SPM12 (http://www.fil.ion.ucl.ac.uk/spm) and stripped of extraneous tissue using the brain mask.

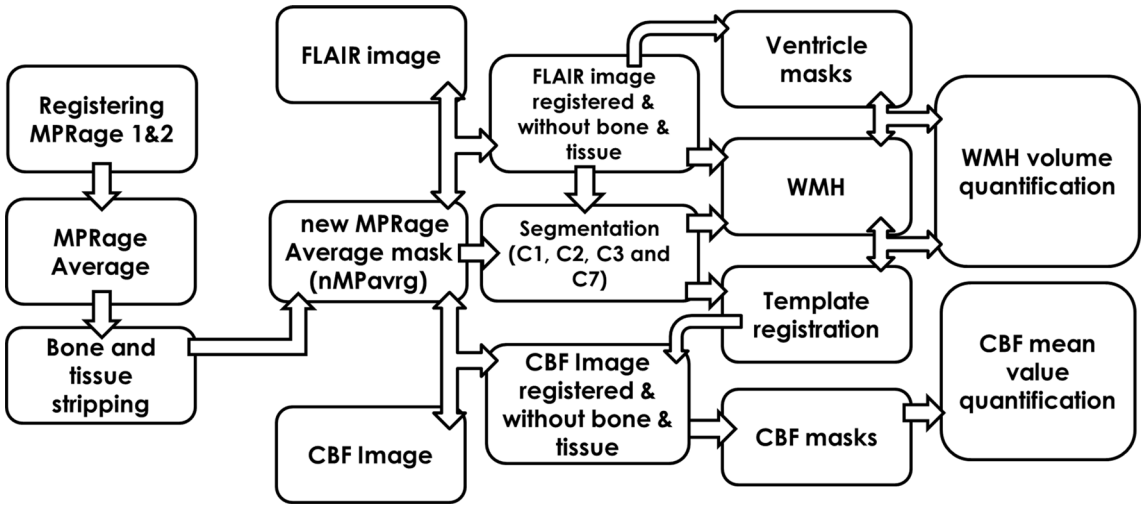

Figure 2-1: Diagrammatic overview of the processing workflow for quantitating WMH and cerebral blood flow using FLAIR and arterial spin-labeling images.

Segments: C1: gray matter; C2: WM tissue class 1; C3: cerebrospinal fluid; C7: WM tissue class 2. Abbreviations: FLAIR, fluid-attenuated inversion recovery; MPRAGE, magnetization-prepared rapid-acquisition gradient echo; WM, white matter; WMH, white matter hyperintensity.

Multimodal segmentation was performed on masked, FLAIR and ASL brain images in the SPM12 unified regime to create separate native-space images representing grey matter (GM; **Fig 2-2a**), white matter (WM) and cerebrospinal fluid (CSF) using an in-house segmentation template created from 145 images of normal subjects. WM was modeled as two separate tissue classes to represent variations due to WM intensities [37]. The international consortium for brain mapping (ICBM) atlas reference was registered to the segmentation template, and atlas regions combined to create masks representing the frontal, temporal, parietal and occipital brain regions for both GM (**Fig. 2-2b**) and WM (**Fig. 2-2c**).

2.2.4 Cerebral Blood Flow (CBF) Quantification

The ICBM lobar masks were registered to each subject's native-space ASL image using the inverse transform generated during segmentation. Median CBF values were extracted from each grey matter template region (**Fig. 2-2d**).

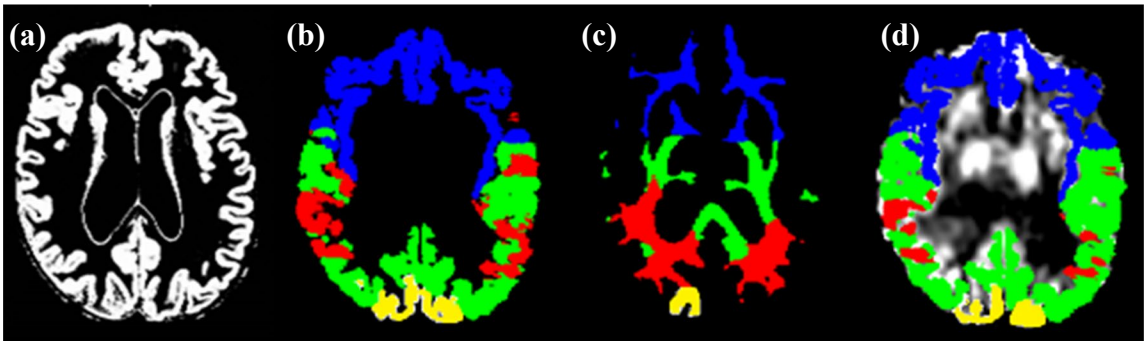

Figure 2-2: Gray matter and white matter masks.
(a) Native-space GM segmented image. (a and c) International Consortium for Brain Mapping template masks of white matter and GM transferred to the standard space of the subject (compare with a). (d) GM template masks applied to the registered arterial spin-labeling image. Abbreviation: GM, gray matter.

2.2.5 White Matter Hyperintensity (WMH) Quantification

The two WM segmentation images (**Fig. 2-3a and Fig. 2-3b**) were summed (**Fig. 3c**) and converted to a binary WM mask in native space (**Fig. 2-3d**). In a few instances WM voxels were misclassified in an extraneous tissue segment, likely due to partial volume effects; in these cases, these voxels were added to the two WM segments before

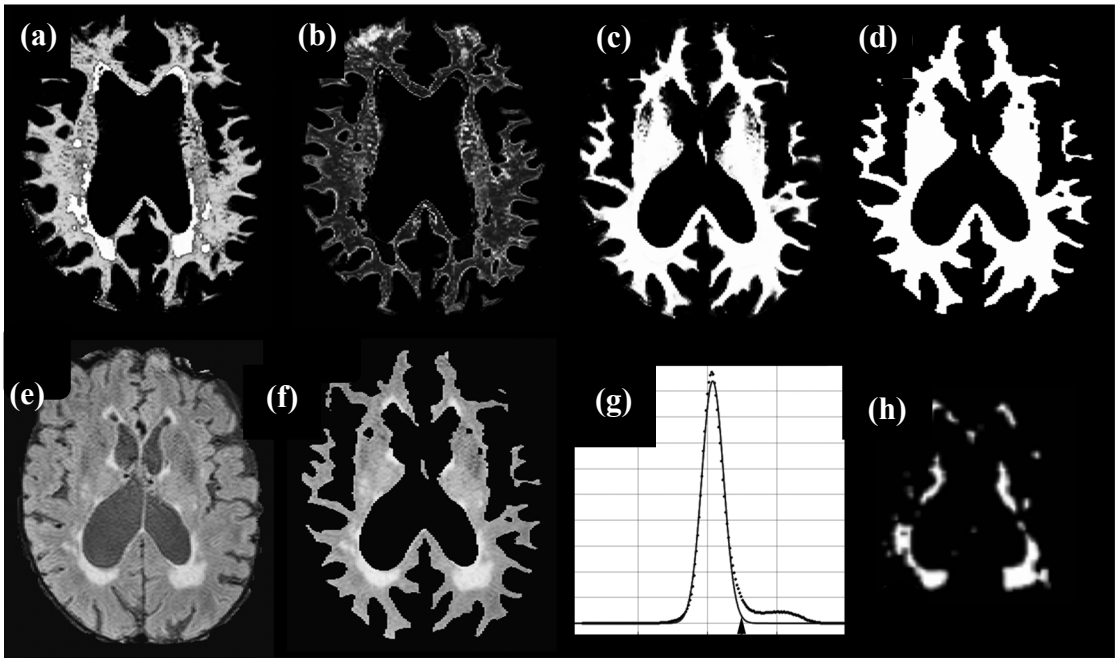

Figure 2-3: Sequential steps of the segmentation process to quantitate WMH.
(a and b) Segmented images representing 2 tissue classes of WM; (c) total WM (a + b); (d) WM mask from thresholding of (d); (e) FLAIR image; (f) FLAIR image masked by d (FLAIR, WM voxels); (g) histogram of (e) showing Gaussian fit and threshold of 3.0 standard deviation (arrowhead); (h) WMH image obtained by applying threshold to (f). Abbreviations: FLAIR, fluid attenuated inversion recovery; WM, white matter; WMH, white matter hyperintensity.

binary conversion. The unitary WM mask isolated WM in the FLAIR image (**Fig. 2-3e**) by multiplication, (**Fig. 2-3f**). The Gaussian fit to the histogram of WM voxels was used to set the threshold for WMH (**Fig. 2-3g**), as the mean plus 3 x SD, corresponding to a p-value of 0.01. The threshold values were applied to each FLAIR image and 1 mm Gaussian filtered to remove noise, creating a WMH image for each subject (**Fig. 2-3h**).

A final quality-control procedure used a high-contrast display of the FLAIR image at the Gaussian-fit mean center and window value of 10 x standard deviation (SD), side by side with the WMH image, comparing slice by slice for correspondence between isolated WMH and FLAIR hyperintensities. Manual editing of extraneous pixels due to pulsation and flow artifacts was needed occasionally, resulting in the final WMH image (Fig. 2-3h), quantitated by calculating total voxels and total WMH voxel volume [37]. Voxels in the WMH image were divided into pWMH and dWMH using the following method designed to produce a reproducible and consistent definition of pWMH and dWMH: (1) the CSF segment (**Fig. 2-4a**) was used to generate a mask by thresholding at 0.33 (**Fig. 2-4b**). Connected voxels were morphologically identified as belonging to ventricles (**Fig. 2-4c**) and isolated (**Fig. 2-4d**). The ventricular volume was intensity-inverted (**Fig. 2-4e**) and multiplied by the FLAIR image (**Fig. 2-4f**) to exclude the CSF (**Fig. 2-4g**), (2) the border

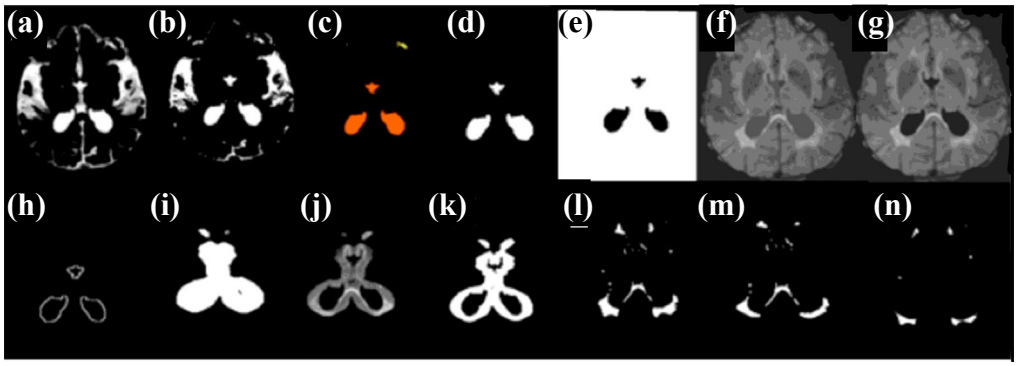

Figure 2-4: Sequential steps in obtaining deep WM and periventricular WM binary masks. (a) CSF isolated from other tissues. (b) Binarized CSF. (c) Ventricular CSF cluster identified. (d) Ventricular tissue voxels. (e) Reversing the intensity of (d) and multiplying by fluid-attenuated inversion recovery image (f) to remove the CSF (g). (h) The edge of (d) that is dilated by 5 × 5 × 5 voxels (i). (i) and (g) are multiplied to obtain the periventricular tissue (j), which is converted to a binary image (k). (l) WMH image; multiply by (k) once and the reverse intensity of (k) once to obtain periventricular WMH and deep WMH, respectively (m and n). Abbreviations: CSF, cerebrospinal fluid; WM, white matter; WMH, white matter hyperintensity.

of the ventricular mask was morphologically identified (**Fig. 2-4h**) and dilated (5^3 voxels; **Fig. 2-4i**), then multiplied by the CSF-excluded FLAIR image to identify periventricular tissue (**Fig. 2-4j**). Ten percent of the mean value from periventricular tissue voxel histogram was set as minimum threshold level to obtain the periventricular binary mask (**Fig. 2-4k**), and (3) this mask was multiplied by the total WMH mask (**Fig. 2-4l;** cf. **Fig. 2-3h**) to obtain pWMH (**Fig. 2-4m**), and the negative of this periventricular binary mask multiplied by the total WMH mask to obtain dWMH (**Fig. 2-4n**).

2.2.6 Statistical Methods

Multivariate analysis of variance (MANOVA) models used log-transformed measured WMH volumes as repeated independent variables because of their typical skewed distributions (JMP v9, SAS Institute). Dependent variables were risk group (high versus low vascular risk) and total intracranial volume (TIV) to control for head size. Post hoc contrasts of dWMH and pWMH versus risk group relationships were performed. A similar model was used for ASL cerebral blood flow in three defined WM regions: the two containing either dWMH or pWMH, and one without WMH. Age, risk group and TIV were used as covariates in this model. To test relationships between dWMH and pWMH, a standard least squares model was constructed with log dWMH as the dependent variable, and risk group nested within log pWMH as independent variables, with TIV as control for head size. A p-value of 0.05 was considered significant; a p-value < 0.10 marginally significant.

2.3 Results

The 26 subjects had a mean age of 77.8 ± 6.8 years (range 66 - 88). There were twenty-three females (mean age 77.8 ± 6.9) and three males (mean age 77.0 ± 7.9). There

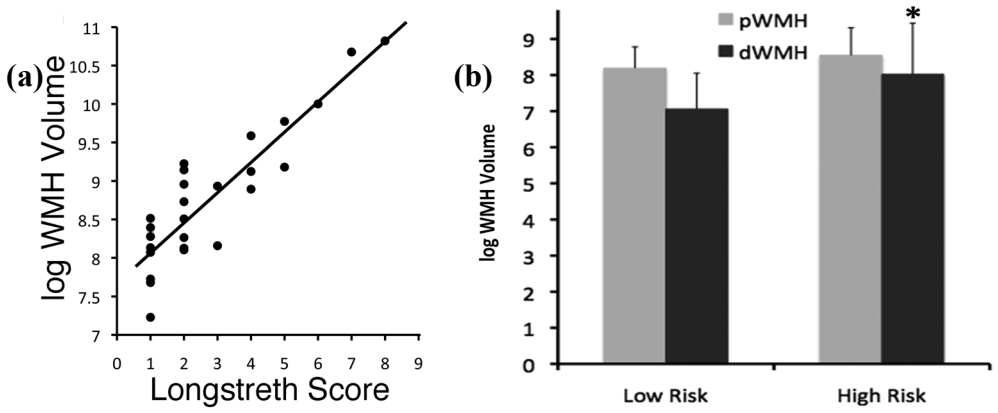

Figure 2-5: White matter hyperintensity volume results.

(a) Linear regression of Longstreth visual rating scale (0-9) for all patients on log WMH total volume, demonstrating the face validity of the WMH volume measurement (adjusted $r^2 = 0.88$, p-value < 0.0001), (b) log WMH volume in low- and high-risk groups; overall volume is higher in high-risk patients (p-value = 0.02), but only the dWMH volume is significant (*p-value = 0.03, error bars = standard deviation). Abbreviations: dWMH, deep white matter hyperintensity; pWMH, periventricular white matter hyperintensity; WMH, white matter hyperintensity.

was a significant difference in age between risk groups: the low-risk group had a mean age of 72.7 ± 4.2 and the high-risk group had a mean age of 83 ± 4.6 (p < 0.0001).

2.3.1 White Matter Hyperintensities

Total WMH volume positively correlated with independent visual ratings using the Longstreth scale [38], confirming that volumes correspond to what a trained neurologist interprets as WMH (**Fig. 2-5a**). There was a significant correlation between pWMH and dWMH in the regression model, but the relationship between pWMH and dWMH was different for high and low-risk subjects: the slope of regression was higher in the high-risk group (1.26 ± 0.22 SE; t = 5.5, p-value < 0.0001) compared to low-risk (0.86 ± 0.34, t = 2.5, p-value = 0.02). The mean dWMH volume was higher in the high-risk group compared to low risk (t = 2.3, p-value = 0.03; **Fig. 2-5b**).

MANOVA analysis confirmed that WMH volume was higher in the high-risk group (F = 5.8, p-value = 0.02). Further analysis demonstrates that dWMH volume was higher in the high-risk group (t = 2.2, p-value = 0.04), but pWMH volume was not significantly different (t = 1.0, p-value = 0.34) between groups. Age correlated with total WMH (p-value = 0.04) and dWMH (p-value = 0.03) but not pWMH volume (p-value = 0.10). There was a strong correlation seen between age and risk score ($r^2 = 0.56$; p-value < 0.0001).

2.3.2 Cerebral Blood Flow

There were no differences in global or in regional cortical GM CBF between risk groups. There was no association between CBF and age. We analyzed associations between WMH volume and regional CBF. Results are shown in **Table 2-1**. Correlations were significant between parietal WMH volume and posterior frontal, parietal, temporal, and occipital CBF, and marginally significant with total CBF. Occipital pWMH volume was significantly correlated with CBF in the medial temporal GM (**Table 2-1**).

Table 2-1 Spearman rank correlations for the pWMH and CBF for different brain regions

Mean (SD)	Total	Frontal (Ant.)	Frontal (Post.)	Occipital	Parietal	Temporal	Temporal (Medial)
Total WMH	-0.28 (0.15)	-0.16 (0.41)	-0.33 (0.09)	-0.37 (0.06)	-0.37 (0.06)	-0.37 (0.06)	-0.31 (0.11)
Frontal	-0.16 (0.41)	-0.16 (0.41)	-0.24 (0.23)	-0.21 (0.29)	-0.17 (0.37)	-0.23 (0.23)	-0.25 (0.20)
Occipital	-0.06 (0.73)	0.13 (0.50)	-0.006 (0.97)	-0.08 (0.66)	-0.07 (0.72)	-0.25 (0.19)	-0.42 (0.03) §
Parietal	-0.34 (0.08)	-0.28 (0.15)	-0.39 (0.04) §	-0.39 (0.04) §	-0.44 (0.02) §	-0.38 (0.05) §	-0.30 (0.13)
Temporal	-0.13 (0.49)	0.004 (0.98)	-0.09 (0.63)	-0.23 (0.24)	-0.18 (0.36)	-0.23 (0.24)	-0.29 (0.14)

Average white matter CBF was calculated for three WM regions containing dWMH, pWMH or neither lesion ($F = 53.5$, p-value < 0.0001; **Fig. 2-6**). Age, risk group and TIV did not significantly affect CBF. Post-hoc paired comparisons showed significantly decreased CBF in dWMH ($t = 5.7$, p-value < 0.001) and pWMH ($t = 11.0$, p-value < 0.0001) regions compared to normal appearing white matter. CBF in pWMH was less than in dWMH areas ($t = 3.1$, p-value = 0.003).

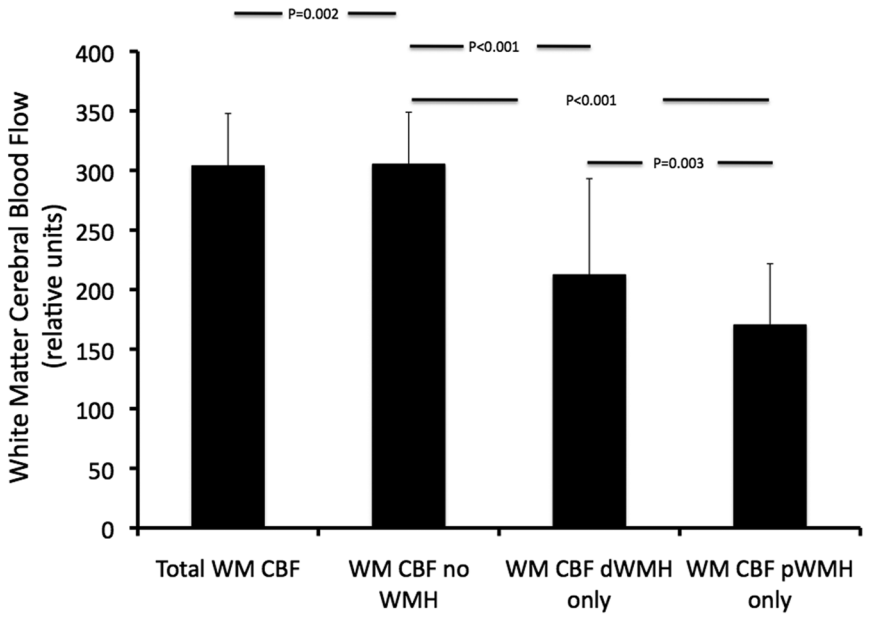

Figure 2-6: Arterial spin-labeling blood flow in the WM (left to right).

Total WM including WMH, total WM but excluding WMH, dWMH regions, and pWMH regions. Paired comparisons are significantly different as shown. Lowest CBF is in the pWMH regions. Bar height: mean CBF; error bars: standard deviation. Abbreviations: CBF, cerebral blood flow; dWMH, deep white matter hyperintensity; pWMH, periventricular white matter hyperintensity; WM, white matter; WMH, white matter hyperintensity.

2.4 Discussion

The aim of this study was to find relationships between WMH, CBF and CVD risk in older patients. CVD risk was assessed by the Framingham CVD stroke risk score assigned to each patient. Fourteen subjects with low-risk were compared to twelve subjects

with high-risk. We used a 3D FLAIR WMH imaging technique that improved resolution and registration and reduced partial volume effects compared to slice-based techniques. The main findings are that dWMH but not pWMH are increased in high-risk patients, and that pWMH but not dWMH are associated with decreased regional cortical GM blood flow. We also found blood flow in white matter is decreased in regions of both pWMH and dWMH, with a greater degree of decrease in pWMH areas.

The underlying origin of WMH remains controversial, perhaps because different mechanisms responsible for their appearance and pathologies can be found at autopsy that so far are not distinguishable using current MRI methods [29, 34, 39-45]. The strongest and most consistent associations with WMH are age and certain cerebrovascular risk factors including diabetes, hypertension, hypercholesterolemia, and cigarette smoking [35, 36, 46-53]. These factors are included in vascular risk measures such as the Framingham score used in this study. A genetic component may be involved in cases where evidence of CVD is lacking [54-58].

Age associations with WMH are likely explained by the accumulation of vascular disease over time together with other changes in cerebral white matter that may be unrelated to small vessel cerebrovascular disease per se, such as cerebral amyloid angiopathy or AD-related changes [59, 60]. Nonetheless, WMH are taken with much supporting evidence to represent a marker of classical small vessel cerebrovascular disease in white matter. CSVD is increasingly recognized as an important pathological contributor to clinical decline in our aging US population, showing strong associations with both gait disorders and vascular dementia [10, 61, 62]. Vascular dementia can occur as a pure form,

or often together with more common dementias including Alzheimer's disease (where it is termed mixed vascular dementia) [63].

We divided WMH into dWMH and pWMH for several reasons [37, 64-68]. First, the white matter tracts adjacent to the ventricles encompassed by pWMH are limbic (cingulum) and motor (corticospinal and related tracts), whereas dWMH are more likely to involve long association tracts and thus long-range inter-regional connectivity. The possibility that clinical correlates of dWMH and pWMH may be different is also supported by the association of dWMH but not pWMH with vascular dementia [37, 69]. Finally, the small-vessel circulation in white matter may be different between deep and periventricular zones, with a greater vulnerability of the periventricular region to large-vessel disease [70]. This is consistent with our finding that low cortical CBF is associated with greater pWMH.

We found that the relationship between pWMH and dWMH was different depending on risk group: the increase in dWMH per given change in pWMH was higher in the high-risk group, even though pWMH volume was the same. This suggests that vascular risk factors are associated with more widespread small vessel disease in white matter, whether directly or indirectly via large vessel flow compromise. Other evidence of CVD in our data was decreased white matter CBF in both dWMH and pWMH regions. However, these differences were not related to age or to CVD risk status.

There are several caveats to the interpretation of our data. The first is the association of age with risk status in our patients. Age is strongly associated with CVD, but there may be other independent effects of age on WMH we aren't able to discern in our analysis. Better selection of subjects and larger recruitment would have helped overcome this limitation. Another caution is the relatively low proportion of patients with high grades of

WMH. We were able to offset this problem by normalizing distributions of WMH and using non-parametric correlations for CBF, still achieving significant results, but these findings should be confirmed in future studies. Additional methodologic analysis considerations include our planned use of a 3D ASL acquisition for better comparison with 3D WMH volumes.

2.5 Conclusions

We find evidence that WMH are usefully divided into dWMH and pWMH regions because they demonstrate differential associations with CVD and demographic risk factors. 3D WMH volume is a potentially valuable marker for CVD that is able to differentiate associations of pWMH and dWMH with risk factor profiles as well as cortical and white matter CBF. Further studies using such methods in distinct and larger cohorts are needed to conform and extend the present findings.

CHAPTER 3. POST-ACQUISITION PROCESSING CONFOUNDS IN BRAIN VOLUMETRIC QUANTIFICATION OF WHITE MATTER HYPERINTENSITIES

3.1 Introduction

Neuroimaging is a critical tool for diagnosing neurodegenerative disease states [15], such as vascular dementia and Alzheimer's disease. The wide-spread availability, high spatial resolution, and variety of imaging-sequences afforded by magnetic resonance imaging (MRI) make it the ideal imaging modality for evaluation of cerebrovascular contributions to cognitive decline. Significant effort has gone into standardizing acquisition sequences for multi-site studies such as the Alzheimer's disease neuroimaging initiative (ADNI) [71], and the adoption of such consensus acquisition sequences beyond ADNI has allowed a greater degree of cross-study comparisons than afforded previously.

Despite such standardization in acquisition protocols, post-acquisition processing techniques for subcortical white matter hyperintensity volume quantification (WMH-VQ) remain variable across studies and research sites. Few studies have examined the reliability and reproducibility of volumetric MRI post-acquisition processing methods [72]. The few studies addressing post-acquisition variability in MRI have focused exclusively on structural segmentation methods. Schnack et al. performed a multi-center MRI study focused on structural segmentation, where the image processing was performed at a single site to reduce anticipated variability [73]. The study suggested that adding a thresholding calibration to the processing algorithm might allow more uniform segmentation across sites. However, this study did not assign multiple raters to verify their protocol, nor did they validate the contention that a protocol, including a standardized thresholding calibration, would reduce cross-site or inter-rater variability.

Published Study: Bahrani et.al, Journal of Neuroscience Methods, 327, 1 November (2019), 108391.

Ramirez et.al. further addressed volumetric protocol reliability using three raters and two repeat scans (interval ~30 min – 50 days) for twenty subjects [74]. However, the study did not examine variability between raters, although they did comment on the issue of variance in the output volumes, which they proposed to be related to brain structure changes during the long interval between the repeated scans, rather than inherent variability in the post-acquisition processing directly. No such studies have as of yet focused on assessing the inter-rater reliability of WMH-VQ techniques.

Visual rating scales have been developed for assessing WMH burden, and while these are reasonable choices for clinical evaluation given their ease of use in facilities lacking modern post-acquisition image processing facilities, they are limited by floor and ceiling effects and do not allow precise quantification necessary for detecting subtle changes in imaging characteristics over time [75]. For this reason, semi-automated and automated techniques have been developed as more reliable and sensitive measures for WMH-VQ [76]. Despite the inherent benefits of automated post-acquisition WMH-VQ techniques, the mean values of WMH volume derived from distinct studies often demonstrate significant variability with mean volumes ranging from 0.5 – 11.2 cc^3 (~5% of the average WMH-VQ across subjects), across otherwise comparable cohorts [77-84]. While such differences are frequently assumed to be due to differential cohort characteristics, it is also possible that inherent sources-of-variability in post-acquisition image processing techniques are responsible for such error given the large number of competing protocols in widespread use [77].

Despite advances in the field of quantitative neuroimaging, no universally agreed upon or standardized methodologies for WMH-VQ post-acquisition processing exist today,

nor have the potential sources-of-variability in such protocols been systematically identified and addressed. In general, protocols for WMH-VQ use the same basic concepts regardless of differences in processing tools (software and algorithms), type of algorithm (semi or fully automated), or study design (cross-sectional or longitudinal) including: 1) image registration, 2) nonbrain tissue stripping, 3) intensity estimation and thresholding, and 4) manual editing (as deemed necessary), yet such differences may influence variability in WMH-VQ. As such, an understanding of the sources-of-variability inherent in WMH-VQ is critical for comparisons of findings across centers and for the integrity of multi-site studies that do not utilize a centralized processing site or standardized, validated, multi-site post-acquisition processing protocol. Furthermore, such understanding of WMH-VQ variability is essential for interpretation of longitudinal studies examining within-subject change, as the potential variability inherent in different quantification protocols (due to advances in software or other scientific/technologic factors), whether semi- or fully automated, can exceed the annual rate of change in WMH volumes for any given subject. The present study systematically analyzed potential sources-of-variability in WMH-VQ procedures that may potentially confound cross-center comparisons, limit the reliability of multi-center studies, and further preclude an accurate understanding of longitudinal within-subject WMH-VQ change.

3.2 Materials and Methods

3.2.1 Participants

MRI acquisitions for 71 subjects (65 – 85 years old, spanning the cognitive continuum from normal through mild cognitive impairment (MCI) to dementia) from the Sanders-Brown Center on Aging (University of Kentucky) research cohort were collected using a standard protocol. A random sample of scans from 21 participants was used for the discovery phase of the study with the remaining 50 participant scans used for validation. Details of the clinical characterization of this cohort have been published previously [85]. This study was approved by the University of Kentucky Institutional Review Board under the protocols used to acquire the clinical data and MRI images.

3.2.2 MRI Acquisition

All MRI scans were acquired at the University of Kentucky, MRISC using a Siemens 3T TIM-Trio MRI scanner (Siemens Healthcare, Erlangen, Germany). A 32-channel head coil was used to scan the subjects. Two acquisition sequences were executed for this study: 1) 3D MPRAGE, TE 2.3 milliseconds, TR 2,530 milliseconds, IR 1,100 milliseconds, FA 7°, 1×1×1 mm resolution full-brain coverage; 2) FLAIR image, TE 388 milliseconds, TR 6,000 milliseconds, IR 2,200 milliseconds, 3D 1×1×1 mm. No gap between slices. All studies presented used identical imaging acquisition protocols, along with the same scanner and head coil.

3.2.3 Image Processing

MRI images were processed using an automated WMH-VQ method, described previously [20]. Briefly, all MRI images were normalized for intensity. Two MPRAGE images were acquired and co-registered using statistical parametric map software (SPM8 or SPM12) (http://www.fil.ion.ucl.ac.uk/spm) and averaged. The averaged-MPRAGE were then registered to the single 3D FLAIR image. Nonbrain tissue was stripped from the registered averaged-MPRAGE image using a brain extraction tool (FSL-BET), FSL-FMRIB software library (FSL v5.0.9) (http://fsl.fmrib.ox.ac.uk/fsl/fslwiki/BET). Remaining scalp tissue was removed slice-by-slice manually, as needed, using the medical image processing analysis and visualization (MIPAV v7.4.0) application (http://mipav.cit.nih.gov). FLAIR images were generated from the binary mask of the stripped averaged-MPRAGE and were further segmented using the SPM unified regime. Five segmented images including, GM, two WM subsegments, CSF, and the unclassified tissue masks were created in a native-space using an in-house segmentation template created from 145 images of healthy normal adult subjects, demographically similar to the subjects in this study [86]. The two WM masks were generated for different WM classes that cannot be captured by one mask (tissue class) and were further summed to create a binary WM mask that was multiplied by the FLAIR. This step isolates all of the classified white matter voxels in the FLAIR image. The intensity distribution of these voxels was then fit with a Gaussian curve. The maximum and minimum threshold values were computed from the Gaussian distribution mean and standard deviation. The threshold value was then applied to the stripped FLAIR images to obtain the final WMH-VQ mask.

3.2.4 Study Design

MRI images were used for both discovery and validation arms of the project as follows: twenty-one scans were used for analyzing the variability associated with software and system compatibility, choice of the center of gravity (CoG), threshold calculations, and manual editing procedures as part of the discovery dataset (**Fig. 3-1**). An independent sample of 50 MRI images was used to analyze the validation dataset after controlling for sources-of-variability identified in the discovery phase of the study.

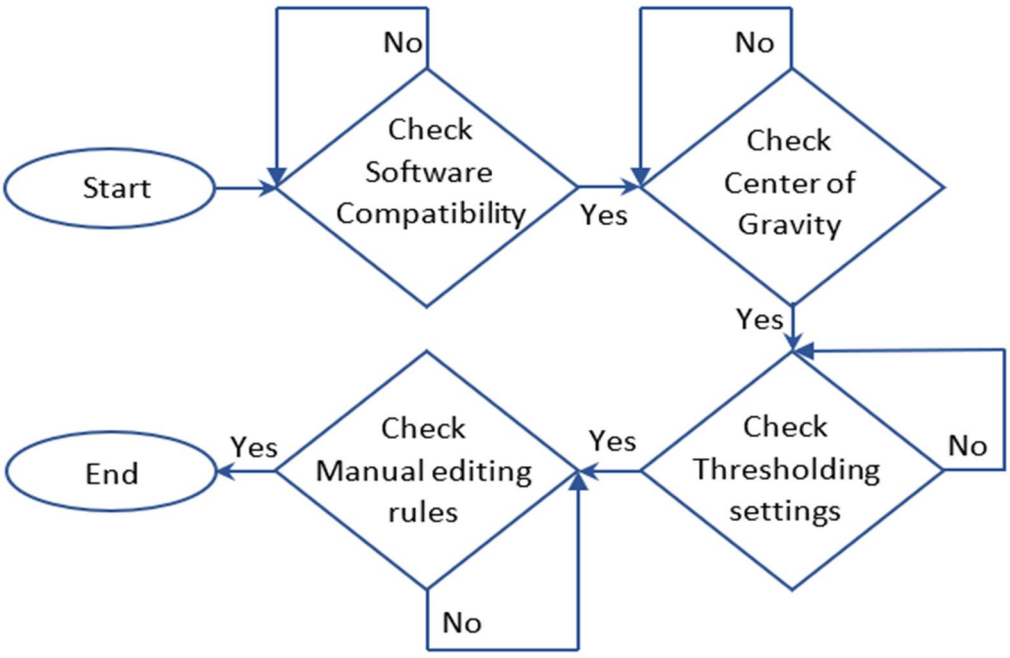

Figure 3-1: Flow chart summarizing the use of the discovery dataset.
A total of 21 scans were examined for discovering the distinct sources-of-variability inherent in white matter hyperintensity volumetric quantification (WMH-VQ) processing techniques.

3.2.5 Software Compatibility

The computers for this study are Linux operating systems and have the same software versions, MATLAB a2015b (MathWorks, Inc), MIPAV v7.4.0, and FSL 5.0.9. Two versions of SPM, including SPM8 and SPM12, were used to examine variance inherent in specific software versions. For this experimental aim, we did not vary other software programs and so recognize that our findings may not generalize across all software systems and version discrepancies. Variability was assessed by comparing the WMH-VQ measurements from identical scans using both SPM8 and SPM12-based analyses.

3.2.6 Center of Gravity

The center of gravity (CoG) is linked to the nonbrain extracting process [87]. An accurate CoG enables a smooth stripping process with virtually no additional manual editing required. To allow assessment of potential variance that is associated with a differential selection of the CoG, two random CoGs were selected for each subject in addition to the systematic CoG. The systematic CoG was chosen by displaying; the registered averaged T1-weighted image using the Triplaner display module in MIPAV to locate the CoG visually (C1), using the cursor (estimating the brain center as one half the brain anterior-posterior, left-right, and inferior-superior distances). The second CoG (C2) was selected using the default CoG of the Triplaner display. The third CoG (C3) was randomly chosen manually by the post-acquisition analyst, but its location was restricted to within a 0.5 cm diameter of C1. Variability was assessed by comparing the WMH-VQ measurements from identical scans using C1, C2, and C3 as the independent variables.

3.2.7 Threshold Calculation and WMH Volume Quantification

To extract the WMH volume, the WMH distribution must be defined [88, 89]. Variability in WMH-VQ are exacerbated when the minimum WMH intensity distribution overlaps with the normal appearing WM intensity distribution, leading to either to over- or under-estimating WMH-VQ due to inconsistent thresholding. We used 10% of the maximum FLAIR WM voxel intensity as the minimum value to obtain the histogram distribution of the WM tissue. This lower limit is flexible and does not appear to contribute significant error in the fitting procedure. However, the upper threshold value is a critical factor for quantifying WMH volume. A two-Gaussian curve fit to the distribution (MATLAB curve-fitting tool) was used for computing the mean and standard deviation (SD). The mean and SD were applied to the thresholding equations to calculate the maximum and minimum thresholds. The thresholds were $mean + 3\ x\ SD$ for the lower bound and $mean + 15\ x\ SD$ for the upper bound [20]. The upper bound eliminated extreme values occasionally seen as intensity artifacts in FLAIR images. All threshold values were expressed to the second decimal place. WMH mask artifacts were reduced using a Gaussian filter (1 x 1 x 1 mm). Total WMH volume was calculated from the final WMH mask.

We tested two parameters in our experiment to study their influence on the thresholding values and in turn on the WMH-VQ. First, we compared the mean and SD of the histogram distribution of the WM voxels extracted from the FLAIR image using voxel intensity and position on the Gaussian curve, versus voxels intensity and volume in mm^3 rather than position on the Gaussian curve. Second, we tested the impact of the precision of the mean and standard deviation on the calculation of the thresholding values. We choose the mean and the SD using the systematic algorithm described above carried to two significant digits (decimal places) as increasing the precision beyond this (i.e., adding additional significant digits (decimal places) did not further contribute to accuracy in the resultant WMH-VQ derived. This threshold was then compared to setting the same mean and SD threshold at a single or no significant digits (an integer).

3.2.8 Manual Editing

The sources-of-variability assessed above are all operator independent, but do not consider artifact removal, which can be an additional source-of-variability that may require one or more manual editing steps. In order to define the variability associated with manual editing, two manual editing steps were included in the protocol to ensure that artifact did not confound the conclusions drawn regarding post-acquisition processing variability. Manual editing was performed on: 1) the whole brain mask after the nonbrain tissue extraction process and 2) the final WMH mask.

Manual editing was performed independently without standardization of procedures and again after developing a standard editing protocol to minimize operator-dependent error in these steps as follows. Extraneous voxels of T2 hyperintensity that are generated due to pulsation and flow artifacts were removed manually, guided by the original FLAIR image. A FLAIR image was displayed with a standard Gaussian-fit mean center and $ten\ x\ SD$ grey scale window value side-by-side with the WMH mask, and the second image was kept with its original values, to allow maximal recognition of false positive and negative voxels. **Fig. 3-2** demonstrates the spectrum of false hyperintensity signals that were removed from the GM, lateral sulcus and pineal gland, the voxels between

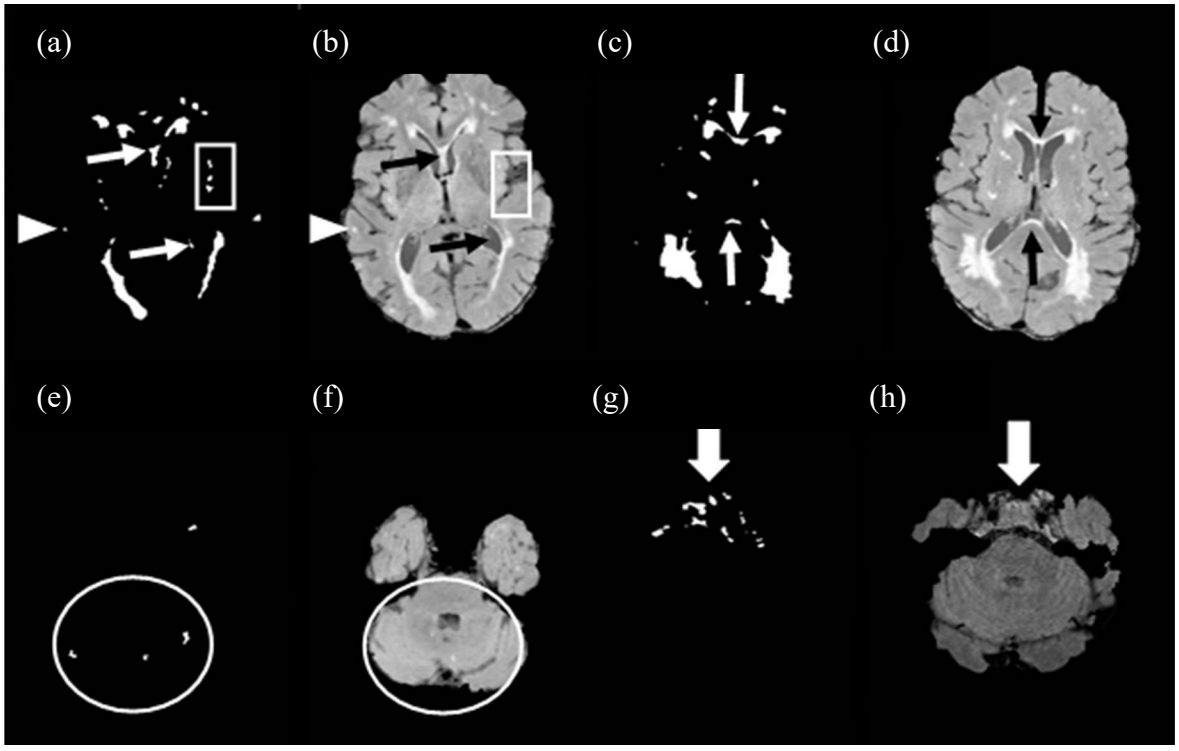

Figure 3-2: Common hyperintensity signal artifacts in the white matter hyperintensity (WMH) mask.
The possible artifacts include: Grey matter signals (GM), (a), and (b), (arrowhead); Lateral sulcus and pineal gland, (a), and (b), (rectangle); Voxels in between and inside the ventricles, a, b, c, and d, (narrow arrow); Voxels in cerebellum (e) and (f) (circle); Voxels in the pons and lower slices (g) and (h) (large arrow).

and inside the ventricles, voxels in the cerebellum, and the voxels in the pons and lower brainstem. A synopsis of our manual protocol guidelines is presented in **Table 3-1**.

Table 3-1. Manual editing protocol developed to systematically reduce sources of variation in the assessment of subcortical small vessel ischemic disease. Sources-of-variability and areas of analysis that require increased diligence and further development of standardized methodology are identified.

Areas to systematically review for T2 artifact	Rationale	Illustrations in Fig. 3-2
Common extraneous voxels	False intensities identified compared to original FLAIR image	a and b
Cortical GM	Extends beyond anatomic boundaries of subcortical disease, but may be considered important for some studies	a and b, (arrowhead)
Lateral sulcus/insular cortex and pineal gland	Signal artifact due to CSF boundary	a and b, (rectangle)
Areas of contrast with GM and CSF between and inside the ventricles	Artifact due to CSF boundary and pulsation	a, b, c, and d, (narrow arrow)
Cerebellum	Prone to infra-tentorial artifact and extensive CSF boundaries, but may be considered important for some studies	e and f (circle)
Pons and lower slices	CSF pulsation from forth vertical may produce hyperintensity voxels in the pons. The extensive artifact in lower slices due to bone & CSF boundaries	g and h (large arrow)
Pituitary gland & cavernous sinus	Extensive artifact due to bone & CSF boundaries	g and h (large arrow)
Basal ganglia & thalamus	Deep GM artifacts due to homogeneous T2 signal need to be distinguished from true small vessel ischemic disease	Not shown

Variability due to manual editing was assessed by comparing the WMH-VQ measurements from identically processed scans using both unstandardized and standardized manual editing protocols as the independent variables.

3.2.9 Validation of a Standard Protocol to Reduce Variance

Controlling for selection of CoG, WM segmentation in SPM, curve fitting and threshold setting on the WM histogram, and manual editing produced a final protocol that was validated in an independent set of 50 MRI scans. We set the threshold for success at 0.5% variability as an acceptable limit of variability well within the range of anticipated within-subject annual longitudinal change. The current variability for WMH-VQ was calculated as a mean of the variability assessed across all parameters studied at ~15%, based on the assumptions that inter-study, and intra-site inter-rater reliability would represent an average rather than cumulative (additive) effect on WMH-VQ assessments.

3.2.10 Statistical Analysis

Using the 21 discovery images, WMH volumes were calculated in a four-step process as follows. First, two raters assessed WMH volume under the protocol described in **Section 2.3** above, one using SPM8 (OA) and one using SPM12 (AB). Variability in ratings was measured by the percent difference in the two raters' ratings, as given below. Next, the software package was fixed (SPM12), and one of the two raters (AB) calculated WMH volume based on different CoG (as described in **Section 2.6**). Then, both software and CoG were fixed, and the rater (AB) calculated WMH volumes under different thresholding conditions, as described in **Section 2.7**. The distribution of the WM voxel intensity and position on the curve was visualized using histograms.

Finally, software, CoG, and threshold were fixed, and manual editing was applied by both raters. The percentage difference (PD) for each set of ratings for each image, which was defined as the difference between the two sets of measurements divided by the average value of the two methods, for each source of variability (i.e., software compatibility, CoG, thresholding, and manual editing):

$$\text{Percentage Difference (PD)} = \left| \frac{Rating\ 1 - Rating\ 2}{\frac{Rating\ 1 + Rating\ 2}{2}} \right| x\ 100$$

These summary PDs were used to quantify the approximate measurement error associated with each source of variability. The overall PD for each discovery image was calculated by taking the average of the four individual PDs. The WMH volumes obtained after implementing all four steps are referred to hereafter as "standardized" WMH.

Once the analyses based on the discovery data were completed, the two raters each calculated WMH volume for the set of 50 validation images based on the unstandardized and standardized protocols. Interrater agreement was assessed using the Pearson correlation coefficient and the Interrater Reliability. SigmaPlot 13 (Systat Software Inc., San Jose, California) was used for statistical data analysis.

Additionally, the permutation test (aka randomization test; MATLAB function https://www.mathworks.com/matlabcentral/fileexchange/63276-permutation-test) was applied to the 50 standardized WMH volumes to test whether mean WMH volume was different between raters (50,000 permutations). Finally, the Dice similarity test (using MATLAB) was utilized to find the similarity and dissimilarity of the WMH final masks before and after the manual editing between the two raters.

3.3 Results

3.3.1 Participants

The mean age of this cohort was (74.1 ± 8.0) years, the mean educational attainment was (16.9 ±3.3) years, and the mean WMH volume was (14.5 ± 23.0 cc^3). In addition, 54% were female, 66% were hypertensive, 26% were diabetic, 10 were smokers, and 56% had hyperlipidemia. Finally, 30% of the cohort were cognitively normal, and the remaining 70% had the diagnosis of mild cognitive impairment at the time of the scan. There were no significant demographic or clinical differences between the discovery and validation data set participants in this study.

3.3.2 Software Versions and Compatibility

Different SPM software versions and software compatibility were found to be a significant source-of-variability. Analysis using SPM8 resulted in an overestimated WMH-VQ compared to analyses using SPM12, 36.44% before editing and 93.26% after editing (n = 21). **Fig. 3-3** shows the difference between the two processed WMH masks in contrast to the FLAIR image (**Fig. 3-3a**). **Fig. 3-3b** is the WMH mask resulting from the use of

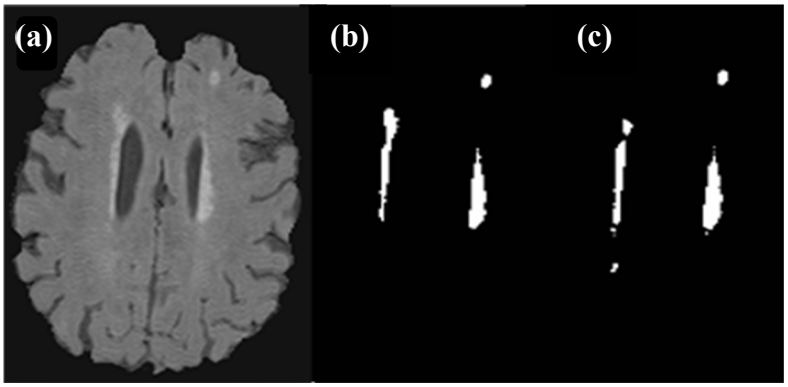

Figure 3-3: WMH masks differ based on SPM versions used.
(a) is the original T2 FLAIR image. (b) WMH mask using MATLAB 2015 and SPM8. It shows an overestimate volume comparing to the FLAIR image and (c), which is the WMH mask that quantified using MATLAB 2015 and SPM12.

SPM8, while **Fig. 3-3c** is the mask utilizing SPM12. These data demonstrate the importance of software version (even from the same source) in affecting variability in WMH-VQ.

3.3.3 Selection of Center

The use of different CoGs introduced a variability of approximately 11% in final WMH volumes. The percentage error in WMH-VQ (mean ± standard error of the mean (SE) in mm^3) determined using C2, (28360 ± 7460), and C3, (33235 ± 8036), compared to C1, (33755 ± 7907), were 20.9% and 16.1%, respectively (n = 21). **Fig. 3-4** demonstrates the artifacts leading to increased WMH-VQ variability as a result of the choice of CoG.

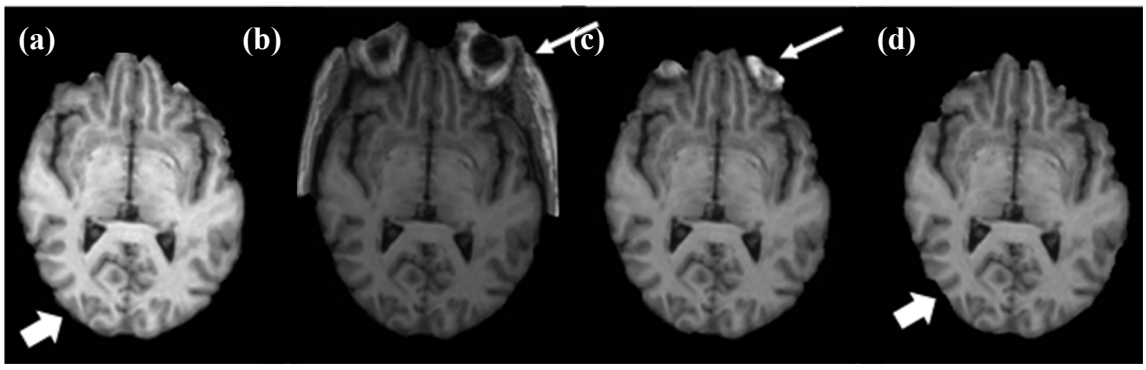

Figure 3-4: The effect of the center of gravity (CoG) on bone extraction method using BET-FSL tools.
(a) demonstrates optimal bone extraction with almost clean brain tissue. (b) and (c) show non-brain tissue remaining (narrow arrows) due to choosing an alternate CoG. (d) demonstrates a loss of a portion of GM due to the non-tissue extraction process as a result of choosing an alternate CoG.

3.3.4 Thresholding

Fitting the histogram distribution of the WM intensities to the Gaussian curve was also shown to contribute to interrater reliability variance in WMH volume before and after manual editing. The percentage variance of fitting the WM histogram distribution of the

WM voxel intensities and volume, mean ± SE (39427 ± 8299), versus the WM voxel intensities and position, (39759 ± 8237) on the Gaussian curve was found to be 2.5% (n = 21). Thresholding the FLAIR mask to compute the WMH volume was also shown to be a significant source-of-variability. The percentage error between the thresholding values carried to either none or one significant digit, versus the maximal selection of two significant digits, was -19.9% and 10.2%, respectively. This percentage error is maximally evident whenever the distribution is not corrected for the natural left-handed skew deviation inherent in community-based samples such as ours and the many others that have been studied to date.

3.3.5 Manual Editing

All steps in the WMH-VQ protocol represent automated processes that can be standardized to reduce variability. While the protocol is fully automated, artifacts can create erroneous volume estimates, and so manual editing may be desired in order to remove artifacts when present. Variability due to non-systematic manual editing was 1.7% (rater-I, 28503 ± 8683 and rater-II, 28394 ± 8667) compared to systematic manual editing. Using this systematic manual editing protocol, the variability in WMH-VQ was reduced to 0.34% overall.

3.3.6 Validation of a Standardized Protocol

In order to investigate whether controlling for these sources of variability could result in a protocol with a minimal acceptable variability (defined as < 0.5% WMH-VQ) could be developed, we studied the performance characteristic of standardized protocol using identical acquisitions, with post-processing performed by independent raters using independent workstations, Inter-rater analysis, using Spearman correlations and linear

regression models for WMH masks before and after editing (**Fig. 3-5**), demonstrated r^2 values = 0.999, with SE = 118.7 and 68.1 respectively, and p-value < 0.001 for the 50 scans used in the validation study. WMH volume variance in the refined protocol was 0.23% before manual editing (all processes automated) and this increased only slightly to 0.34% after manual editing once all sources-of-variability were addressed in a systematic fashion. The permutation test showed the observed mean difference in WMH volume before manual editing was 12.37, and p-value = 0.998; the observed mean difference was 0.97 and p-value = 0.999 after editing, which again shows a good concordance between the raters. As well, the Dice similarity test confirmed that result with 0.99 (dissimilarity: 0.009) before editing and 0.98 (dissimilarity: 0.018) after manual editing.

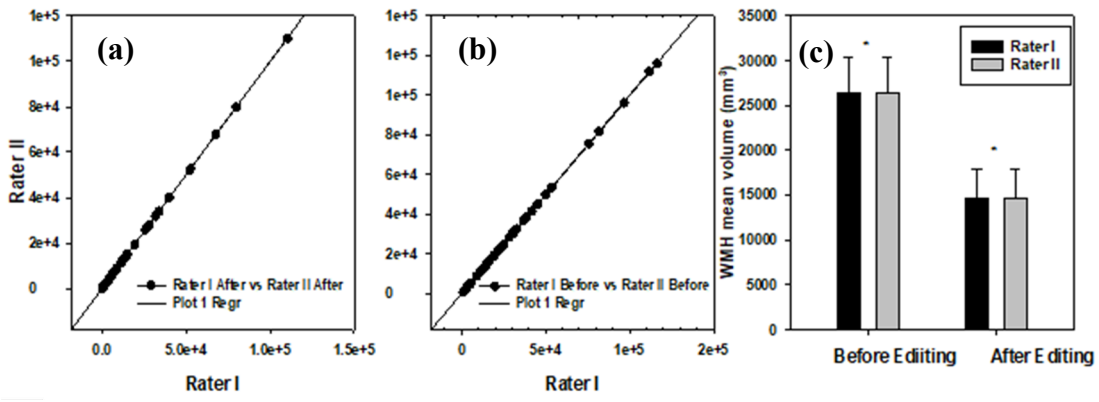

Figure 3-5: WMH rater inter-rater results.
Regression curve for WMH volumes after and before editing (a) and (b), respectively, (n = 50)). (c), the mean value of WMH volume for both raters before and after editing (n = 50). r^2 = 0.999, Standard error estimation before editing 118.7 and after editing 68.1. (p-value < 0.001).

3.4 Discussion

This study demonstrates that even automated post-acquisition WMH-VQ techniques have several inherent sources-of-variability that can lead to discrepant results

between raters and centers using different post-acquisition protocols. The importance of this finding should not be understated, as the data generated and the conclusions drawn from different raters and centers, even when using standardized data acquisition and source images such as those acquired in ADNI or other large multi-center collaboratives, can be quite discrepant if post-acquisition protocols have not been refined and such sources-of-variability addressed.

The present data further demonstrate that systematically identifying and addressing potential sources-of-variability inherent in post-acquisition WMH-VQ techniques can result in a dramatic reduction in intra-scan variability from ~15% to less than 0.5%. Sources-of-variability identified in the present study, and methods to overcome these confounds, include the selection of CoG, thresholding effects, software versions, and manual editing procedures (as included in the protocol). Specific discussion focused on each identified source-of-variability and methods developed to reduce such variability are presented below.

The present data demonstrate the importance of software compatibility for any longitudinal, multi-center study lacking: 1) a central uniform post-acquisition processing center, 2) central processing centers that undergo software upgrades between acquisitions and processing of images, or 3) for between-study comparisons using different post-acquisition processing regimens. SPM is based on the use of MATLAB scripts. Updating one of these software packages without updating the other produced significant variability in intra-scan WMH-VQ. As software versions are constantly evolving, it is necessary to re-evaluate potential sources-of-variability introduced with each new software version employed both within and across sites. As such, one should also consider the issue of

variability introduced when combining legacy data with recently acquired data if software versions are upgraded (as they are likely to be) over time. While such upgrades are important for enabling technological progress in WMH-VQ measurements, unless legacy scan data is reprocessed with the same software, drawing conclusions regarding longitudinal datasets from post-acquisition data derived from protocols using different software versions may be problematic. The present data demonstrate that considerations of increased variability in such samples could be at least partially responsible for changes in longitudinal trajectories or analyses examining historical or birth cohort effects.

Another source of variability lies in the selection of the CoG, which can affect non-brain tissue extraction. Nonbrain tissue extraction is essential for optimal brain segmentation [90]. The BET stripping tool is a common brain extraction tool that is easy to use and to script [91, 92]. In order to obtain an accurate non-tissue extraction result with BET, the CoG should be consistently and uniformly assigned across protocols [93, 94]. The closer the CoG is to the center of the brain (tissue to be analyzed), the less non-brain tissue artifact will be seen (see **Fig. 3-4**). Random estimation of the CoG or variability in such estimation that differs by protocol could increase the sources-of-variability due to the inclusion of residual of nonbrain tissue. This problem may be solved by either performing manual editing, increasing the number of BET iterations [95], or editing the CoG manually to ensure uniformity. The selection of three distinct CoGs isolated as independent variables, allowed us to examine the variability associated with such selection independent of other procedures. While many automated protocols select identical CoGs, the exact CoG selected often differs by protocol, and many protocols do not take into account differences in brain center coordinates that may vary from subject to the subject due to subject positioning in

the scanner. Certain CoG selections can increase artifacts related to excess inclusion of nonbrain tissue. Standardized selection of CoG, necessary to develop uniform protocols across disparate raters, centers, and studies will require the development of consensus best-practices in the field of post-acquisition processing.

The selection of an appropriate threshold is critical for specifying the volume of WMH to include in the mask. If the threshold is set too high, it will reduce the sensitivity of WMH detection, while setting the threshold too low can increase the presence of WMH artifacts that may necessitate the inclusion of burdensome manual editing processes. The highest sensitivity to thresholding value effects exists for subjects with large WMH volumes and is less important for those with low levels of such imaging findings. The present analysis found that two independent Gaussian curves provided the most consistent principal fit to the mean of the hyperintensity distribution. Even though the histogram distribution of WM using intensity and voxel position vs. voxel volume showed a relatively small variance < 3%, it still remained one of the sources-of-variability in excess of the acceptable threshold set in our study aims.

Manual editing may be necessary for accurate WMH-VQ assessment, as the WMH mask will likely contain at least some FLAIR artifact. The decision to include a manual editing step(s) may be dependent on the protocol specifics that either limit or increase artifact representation in the WMH-VQ assessment. The present data demonstrate that WMH-VQ can be overestimated by as much as 42% using an automated process without manual editing. While such overestimates due to artifact may exhibit regression to the mean when analyzing large samples, they prohibit accurate assessments of the true WMH-VQ and further prevent accurate analyses when working with smaller samples or when

considering within-subject change in WMH-VQ. While machine learning techniques are being developed to address editing procedures systematically, manual editing may still be required for many studies depending on the sample size and the nature of the hypothesis being tested. It is important also to note that machine learning techniques often require the "ground truth" in the training set. Therefore, obtaining an accurate "ground truth" was the main purpose of the present study. Given these considerations, manual editing remains a common necessity for WMH-VQ protocols until improved automated machine learning techniques are introduced into the field.

While introducing human bias with manual editing procedures, the present data demonstrate that the development of standard rules for manual editing can significantly reduce intra-scan variability in the final WMH masks and WMH-VQ results, despite such procedures. Specific editing rules that proved useful for reducing inter-rater variability included: 1) removal of T2 hyperintensity artifacts in CSF/GM junctions, especially those involving the septum pellucidum; 2) removal of all T2 hyperintensities below the level of the midbrain, including the cerebellum, as this area is highly prone to significant pulsation and other artifacts; 3) removal of T2 signal hyperintensities in the cortical GM; and 4) editing of the supratentorial deep GM structures (including the basal ganglia and thalamus) that require special attention as these structures are in end-arterial zones that are both subject to high levels of small vessel ischemic disease and are also prone to significant artifact. [96, 97] Irrespective of the specific rules for manual editing standardization that are applied to a given protocol, it is clear that specifying such procedures and standardizing them across raters, sites, and studies would help reduce the variability in WMH-VQ seen within and across disparate studies.

While the present findings and method developed to focus on a cross-sectional analysis, the reduction in sources-of-variability suggested in the present methods are critically important for any studies assessing longitudinal change in WMH-VQ. As changes in WMH-VQ are estimated at ~5%/year, any protocol that introduces a greater degree of variability in cross-sectional findings is likely to generate inaccurate longitudinal results. Our analyses of both the findings reported in the literature and those described within our study suggest that current variability demonstrated in WMH-VQ assessment is 10-15%, a simply unacceptable figure. As study protocols and software versions are constantly being modified for improvement overtime, re-grounding legacy data and longitudinal data collection based on the principles described are critical for scientific discovery in the field of WMH-VQ.

This new method of addressing post-acquisition sources-of-variability overcomes this limitation and may further prove to be even more useful if integrated with other acquisition methods to reduce variability, e.g., longitudinal data is acquired with the same imaging sequence and protocol on the same scanner.

Study limitations include our focus on a largely Caucasian, highly educated, aged, study population that may limit the generalizability of our findings to such populations. Minority and underserved health-disparity populations at even greater risk for cerebrovascular disease and WMH accumulation are an important focus of future studies that we did not address directly in this study. In addition, caution should be used in interpreting these data in regards to disease processes that may affect younger populations such as those with multiple sclerosis, as such subjects were not studied in our experimental design. Further limitations include the use of specific software programs that were analyzed

and a statistical threshold-based analysis approach, and it is possible that the present considerations studied may not be applicable to all software programs and version upgrades. In addition, we did not fully explore how the region of interest (ROI) analyses would be impacted by the use of standardized methodologies, although it is assumed that such analyses would benefit from the standardized approach presented. Further work in this area is clearly indicated. Despite such caveats, the present data suggest that careful attention to what may seem to be simple changes in software version (incidental upgrades) or selection of post-acquisition analysis parameters (selection of CoG and thresholding limits), and standardization of operator-dependent steps (manual editing) may improve cross-site, cross-study and longitudinal WMH-VQ assessments in order to advance the field.

Future directions include analyzing the potential sources-of-variability in WMH-VQ across-sites to identify better which variables are most important for establishing cross-center reliability. A further focus on sources-of-variability that exist within subjects in longitudinal studies also need to be pursued before we can possibly use within-subject change in WMH-VQ as a reliable outcome measure for imaging findings related to vascular cognitive impairment or vascular dementia. Data from the present study are also being used currently as the "ground truth" in our collaborative development in advance artificial intelligence machine learning approaches to WMH-VQ.

The final validation study attempted to determine if addressing all the sources-of-variability identified in the study in composite would lead to a protocol with overall reduced WMH-VQ variability that we considered acceptable (defined as variability < 0.5%). This was important as the field is in need of protocol development adequate to study

within subject WMH-VQ change accurately in the setting of an average WMH-VQ change that is approximately 5% of the total WMH-VQ measurement. This goal was achieved, on the basis of the present set of experiments, demonstrating a post-acquisition WMH-VQ variance well under our target of < 0.5%. While the standardized protocol used in this study may not be ideal for many researchers, dependent on their needs and practical implementation of the data derived, the lessons learned in addressing potential sources-of-variability in WMH-VQ assessment techniques can be applied universally to help limit the methodologic variability that confounds the present literature.

3.5 Conclusions

The present study sought to systematically identify sources-of-variability in WMH-VQ techniques that can confound both within-site as well as cross-site data comparisons and conclusions. This exercise allowed the development of a standardized protocol, minimizing potential sources of bias and variability in the determination of WMH-VQ measurements in our study sample. While the developed protocol was found to be optimal for use in the present dataset for the detection of subcortical white matter disease, many other protocols exist in the field and may have unique attributes that make them optimal for their specific study purposes. Such protocols should, in light of the present data, systematically evaluate the sources-of-variability inherent in their methodologies to move the field of post-acquisition processing of WMH-VQ into a more rigorous and standardized arena where data may be able to be better compared across studies and sites. In addition, data on WMH-VQ that may represent a more reliable “ground truth” is critical for the development and training of machine learning algorithms that may allow future artificial intelligence approaches to WMH-VQ assessment.

These data strongly support the notion that consensus “best-practices” should be developed in the field to aid such discovery. Only through such initiatives can we hope to advance our understanding of the risks, diagnosis, study outcome measures, and treatment modality considerations that might mitigate the impact of small vessel ischemic disease on the population today and in our future scientific endeavors.

CHAPTER 4. DIFFUSE OPTICAL ASSESSMENT OF CEREBRAL AUTOREGULATION IN OLDER ADULTS STRATIFIED BY CEREBROVASCULAR RISK

4.1 Introduction

Cerebrovascular disease (CVD) is the fifth most common cause of mortality in the United States (0.14 million in 2017) [2, 3], and the second worldwide (17.6 million in 2016) [4]. Risk factors for CVD include aging, atherosclerosis, smoking, hypertension, high cholesterol, and diabetes [5, 6, 8, 98]. Among others, aging represents the major risk factor for the development of CSVD. Diagnosis of CSVD at early stages is essential for preventing sequential complications. Ideal diagnostic tests should be noninvasive, low-cost, and have high diagnostic accuracy for CSVD in early stages of the disease.

CSVD is often associated with abnormal microvasculature and tissue dysfunction in the brain, which may impact cerebral autoregulation (CA) [99, 100]. CA is a physiological mechanism maintaining stable cerebral blood flow (CBF) within a certain range of blood pressure variations [100, 101] . CA has been assessed by quantifying the relationships (gains) of spontaneous low-frequency oscillations (LFOs) between the mean arterial pressure (MAP) and cerebral hemodynamic parameters such as CBF and cerebral blood oxygenation [102]. In general, smaller LFO gains correspond to better CAs [103, 104]. Although the origin of LFOs remains controversial in the literature, studies have found that the endothelial, neurogenic, and myogenic controls are the main mechanisms responsible for maintaining CBF constant during blood pressure fluctuations [105]. Previous studies have classified LFOs into four frequency intervals: I (0.005-0.0095 Hz), II (0.0095-0.02 Hz), III (0.02-0.07 Hz), and IV (0.07-0.2 Hz) [106-112]. Interval-I and Interval-II reflect respectively nitric oxide dependent and independent endothelial

Submitted for publication: Bahrani et.al (2020)

metabolic activities [107, 109, 110]. Interval-III and Interval-IV correspond respectively to neurogenic and myogenic related metabolic activities [106, 111, 112].

In study of LFOs, MAP is often monitored by a noninvasive finger plethysmography technique, which was used in this study. Functional MRI has been used to image cerebral hemodynamics with high spatial resolution, although the high cost, low sampling rate, and non-portability limits its frequent use. Transcranial Doppler ultrasound (TCD) has been used to measure cerebral blood flow velocity (CBFV) in major arteries, which may not be consistent with CBF in the microvasculature [23]. Also, TCD cannot be performed in ~10% of subjects who do not have adequate acoustic windows [24]. Near-infrared spectroscopy (NIRS) provides a noninvasive, rapid, portable, and low-cost alternative for continuous monitoring of cerebral blood oxygenation in the microvasculature, although it does not directly measure CBF [113]. Since CBF and cerebral blood oxygenation are usually coupled and interactive, it is desirable to measure both quantities and investigate their complex relationship.

TCD/NIRS has been used to measure LFOs in CBFV/cerebral blood oxygenation for CA assessment [114-117]. Different orthostatic protocols were applied to induce MAP fluctuations for evaluating dynamic CA including a sit-stand maneuver [118] and tilting bed [114]. The selected LFO frequency intervals varied in different studies [109, 115, 117, 118], and study cohorts included age-matched older healthy subjects and patients with symptomatic carotid occlusion, ischemic stroke, or Alzheimer's disease (AD) [104, 116, 119, 120]. Previous studies have found that CAs (associated with LFO gains) were impaired in patients with symptomatic carotid occlusion or ischemic stroke [104, 119, 120], but preserved in patients with AD [116].

Previously, we conducted a preliminary study in young healthy subjects using an innovative hybrid near-infrared spectroscopy/diffuse correlation spectroscopy (NIRS/DCS) instrument to simultaneously quantify LFOs of CBF and cerebral blood oxygenation at rest, during and after 70° head-up-tilting (HUT) [105]. The hybrid instrument consists of a laboratory-made DCS device for CBF measurements and a commercial frequency-domain NIRS device (Imagent, ISS) for cerebral blood oxygenation measurements including oxy-hemoglobin and deoxy-hemoglobin concentrations ([HbO_2] and [Hb]). HUT was performed to enhance LFOs at ~0.1 Hz. Results from this pilot study demonstrated the feasibility and reliability of using NIR diffuse optical technologies to simultaneously quantify LFOs of multiple cerebral hemodynamic parameters including CBF, [HbO_2] and [Hb].

This study used the hybrid NIRS/DCS instrument to simultaneously detect LFOs of cerebral hemodynamics in cognitively healthy older subjects with high or low-risk for developing CVD. Cerebral hemodynamic data were continuously collected at rest, during, and after 70° HUT. LFO intensities were extracted from the measured variables (MAP, CBF, [HbO_2], and [Hb]) using power spectral analyses in four frequency intervals (Interval-I to Interval-IV) [106-112]. The LFO transfer function gains were quantified by transfer function analyses with MAP as the input and cerebral hemodynamic variables (CBF, [HbO_2], and [Hb]) as the outputs [105]. Since LFO gains correlate inversely with the CAs [103, 104], we hypothesized that they can be used as biomarkers for diagnosis of CVD at early stages, i.e., distinguishing two groups of subjects with high or low-risk for developing CVD.

4.2 Materials and Methods

4.2.1 Participants

This study was approved by the University of Kentucky (UK) Institutional Review Board (IRB). The written IRB consent was obtained from each subject before participation. Twenty-six cognitively healthy older adults (23 females and 3 males) with a mean age of 77.7 ± 6.8 years (mean ± standard deviation) were recruited from a well-characterized aging cohort, followed by the Alzheimer's Disease Center (ADC) at the UK Sanders-Brown Center on Aging. Subjects with at least one of the following criteria were excluded from the study: unstable cardiac diseases, orthostatic symptoms during upright standing, non-CVD causes of cognitive decline, and AD risk factors such as APOE4 allele, atrial fibrillation, and other coexisting brain disorders.

The level of individual's risk for developing CVD was evaluated based on clinical diagnosis by neurologists and ADC databases. The Framingham study risk scores were adapted to predict CVD over 10 years including gender, age, history of diabetes, blood pressure, smoking, and cholesterol level [20, 36]. The scoring scale of Framingham ranged from 1 to 30 points. The 26 subjects with risks for CVD were classified into two groups based on the cutoff of 15-points: low-risk group (n = 14) and high-risk group (n = 12).

4.2.2 Experimental Protocols

Following our established experimental protocol [105], the participant was asked to lie in a supine-position on a tilting bed (Hausmann). Two Velcro strips were used (one over the chest and another over the knee) to protect the subject from falling during HUT (**Fig. 4-1a**). A hybrid NIRS/DCS probe (**Fig. 4-1b**) was fixed with a medical tap on the middle of the forehead about 1-cm above the eyebrows to avoid frontal air sinuses. Another

layer of elastic bandage was wrapped around the subject's head to secure the probe and

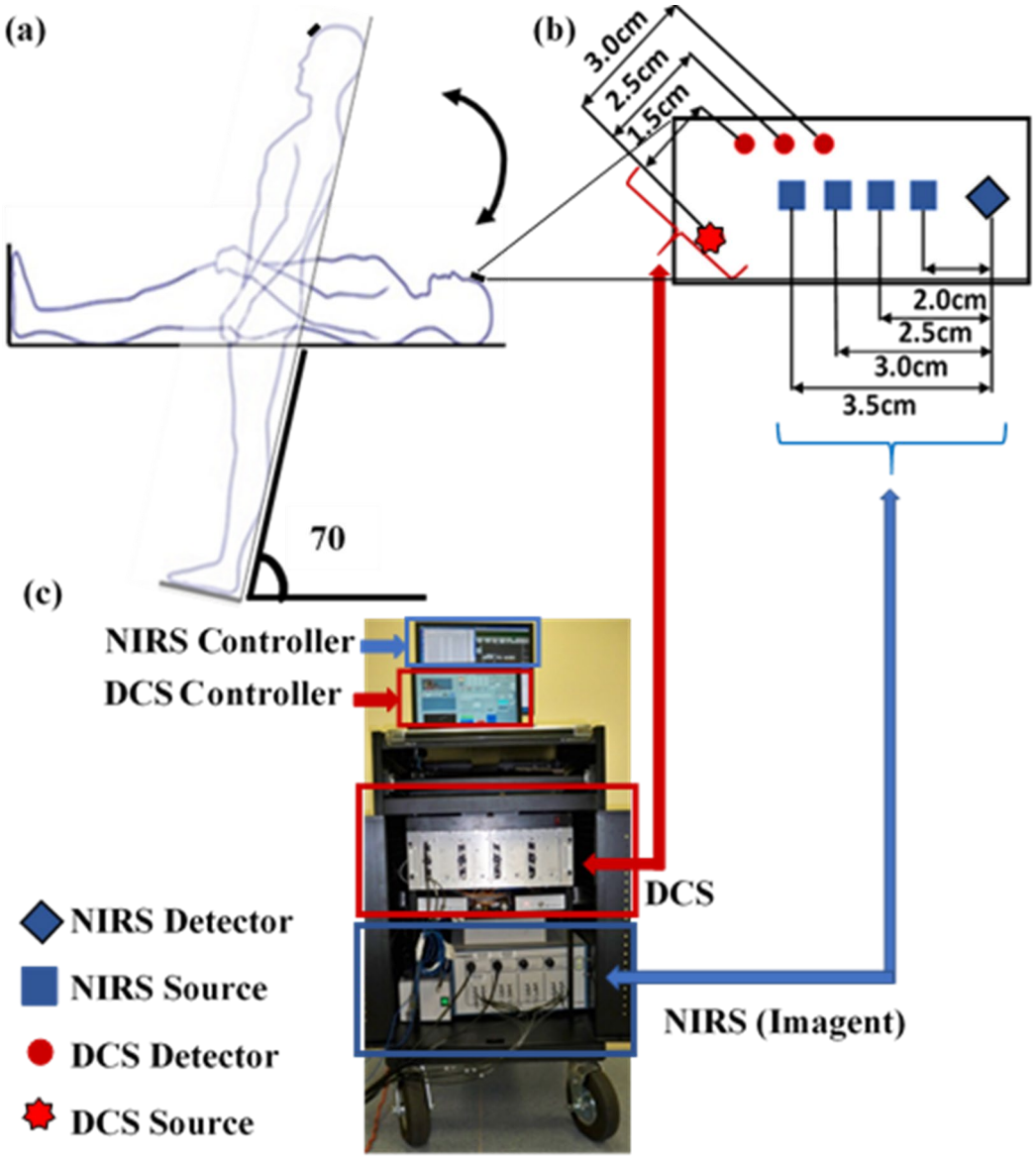

Figure 4-1: A hybrid NIRS/DCS instrument for continuous and simultaneous measurements of $\Delta[HbO_2]$, $\Delta[Hb]$ and rCBF before, during and after head-up-tilting (HUT).

(a) Illustration of a titling bed. and baseline, HUT, and recovery positions. **(b)** A hybrid NIRS/DCS probe with multiple S-D separations. **(c)** A hybrid instrument integrating a commercial NIRS device (Imagent, ISS) and a laboratory-made DCS device.

eliminate the influence of ambient light. The hybrid optical probe was connected to the hybrid NIRS/DCS instrument for cerebral hemodynamic monitoring (**Fig. 4-1c**). A finger

photoplethysmography sensor (Portapres, Netherlands), calibrated by a regular pressure-cuff on the subject's upper arm, was used to record MAP continuously. Optical data were continuously recorded by the hybrid NIRS/DCS instrument throughout the entire experimental protocol, which included a 10-min baseline at rest, 10-min HUT (70°), and 10-min recovery after HUT back to 0°. A physician stayed at the bedside of the testing room for safety monitoring during experiments.

4.2.3 Hybrid NIRS/DCS Instrument for [HbO_2], [Hb] and CBF Measurements

Details about our innovative hybrid NIRS/DCS instrument for simultaneous measurements of [HbO_2], [Hb] and CBF have been reported previously [105]. Briefly, a commercial frequency-domain NIRS device (Imagent, ISS) was used for cerebral blood oxygenation measurements. The Imagent device measured changes in amplitudes and phases of frequency-modulated light (110 MHz) at two wavelengths (690 and 830 nm, < 10 mW) resulting from tissue absorption and scattering using four source-detector (S-D) with separations of 2.0, 2.5, 3.0, and 3.5 cm. A simplified solution based on a semi-infinite geometry for the photon diffusion equation revealed linear relationships between the measured phases and logarithmic amplitudes versus S-D separations. The wavelength-dependent tissue absorption coefficient μ_a and reduced scattering coefficient μ_s' were then extracted by fitting the slopes of these linear relationships. The absolute baseline values of [HbO_2] and [Hb] were calculated from the measured μ_a at the two wavelengths. However, due to the instability of phase slopes over time, phase data were ignored from our analysis. The amplitudes at the two wavelengths from a single S-D separation (2.5 cm) were eventually used to calculate the relative changes in cerebral blood oxygenation (i.e., Δ[HbO_2] and Δ[Hb]) based on the Modified Beer-Lambert law [121, 122].

A laboratory-made DCS device was used for CBF measurements [105, 123-125]. The DCS device used a long-coherence laser diode at 830 nm (100 mW, CrystaLaser) as the source and 16 single-photon-counting avalanche photodiode detectors (APDs, PerkinElmer) as the detectors with S-D separations of 1.5, 2.5, and 3.0 cm. The laser diode transmitted long-coherent light through a source fiber (diameter = 200 μm) into the tissue. The APDs detected temporal light intensity fluctuations in a single speckle area on the tissue surface through single-mode fibers (core diameter = 5.6 μm), resulting primarily from the motions of red blood cells in the microvasculature (i.e., CBF). Signals collected by eight APDs at the S-D separation of 2.5 cm were averaged to improve the signal-to-noise ratio (SNR). The relative change in CBF (rCBF) was calculated by normalizing data to its baseline value (assigned to be 100%) before HUT.

The laser diodes for DCS and Imagent measurements were turned on alternately to avoid the light interference between the flow and oxygenation measurements. The acquisition time for collecting one frame of cerebral hemodynamic data was ~1.4 seconds (equivalent to a sampling rate f_s = 0.7 Hz), which included ~0.8 seconds for Imagent measurement, ~0.5 seconds for DCS measurement, and ~0.1 seconds for switching between the two measurements.

4.2.4 Extraction of Low-Frequency Oscillation (LFO) Intensities/PSDs

LFO intensities of MAP, rCBF, $\Delta[HbO_2]$ and $\Delta[Hb]$ under three physiological conditions (i.e., at rest, during HUT, and during recovery after HUT) are extracted from their power spectral densities (PSDs), calculated by Welch's method [105]. Briefly, 10-min time course dataset under each physiological condition (~420 data points at the sampling rate f_s = ~0.7 Hz) is first detrended to remove the baseline shift. The detrended data are

divided into eight segments with 50% overlap in two adjacent segments, producing a data length of ~93 (420 × 2/9) points for each segment. The PSD_x (f) and PSD_y (f) are generated by MATLAB function of "pwelch". Here, x denotes to the MAP signal, y denotes to other physiological signals (CBF, $[HbO_2]$, and [Hb]), and f is the frequency with a resolution of ~0.0075 Hz ($f_s/93$) in the range of 0.005 to 0.2 Hz. The cross-spectral density CSD_{xy} (f) is calculated by MATLAB function of "cpsd".

4.2.5 Assessment of LFO Gain and Cerebral Autoregulation (CA)

CA has been assumed to be a linear system with MAP as the input and cerebral hemodynamic parameters as the outputs. The gain G(f) of a linear system is quantified by transfer function analysis $G(f) = \frac{CSD_{xy}(f)}{PSD_{xx}(f)}$ [105]. Here, G(f) is classified into 4 frequency intervals: Interval-I = 0.005-0.095 Hz, Interval-II = 0.095-0.02 Hz, Interval-III = 0.02-0.07 Hz, and Interval-IV = 0.07-0.2 Hz. The mean value of G(f) in each frequency interval is calculated as a biomarker to assess CA: $CA \propto 1/G(f)$ [103, 104].

4.2.6 Statistical Analysis

Independent t-tests are conducted to test intergroup differences in LFO gains between the two groups at each frequency interval under each physiological condition using IBM SPSS (SPSS, 2019). Wilcoxon signed ranks tests are performed to test the intragroup differences between the baseline and other physiological conditions (i.e., during and after HUT). A p-value of < 0.05 is considered significant.

4.3 Results

4.3.1 Subjects Characteristics and Valid Measurements

Although 26 cognitively healthy older subjects (23 females and 3 males) were measured, one female subject from the high-risk group was excluded from data analysis due to failure of optical measurements. One male subject from the low-risk group was also excluded due to the occurrence of syncope during HUT. In addition, one female subject from the low-risk group had an abnormal MAP measurement during the recovery. Accordingly, 13 female subjects (73.0 ± 4.3 years) were included in the low-risk group for data analysis (13 at baseline, 13 during HUT, and 12 after HUT for recovery). Nine females and two males (84.2 ± 4.0 years) were included in the high-risk group (n = 11). The significant difference in age between the two groups ($P < 0.001$) had been considered in Framingham risk scores.

4.3.2 Time-Course Cerebral Hemodynamic Response to Head-Up Tilting

Fig. 4-2 shows the time-course data taken from two subjects with high or low-risk for CVD before, during, and after HUT. All measured parameters at the resting baseline were relatively stable. As expected, rCBF decreased during HUT due to the decrease of cardiac output and the increase of cerebrovascular resistance induced by the orthostatic stress. The reduced rCBF affected oxygen delivery, thus led to variations in $\Delta[HbO_2]$ and $\Delta[Hb]$. Most of subjects (22 out of 24) had a trend similarly to these two subjects. However, two subjects in the low-risk group exhibited an increase in rCBF (data not shown). After recovery, all measured physiological parameters tended to return to their baseline levels.

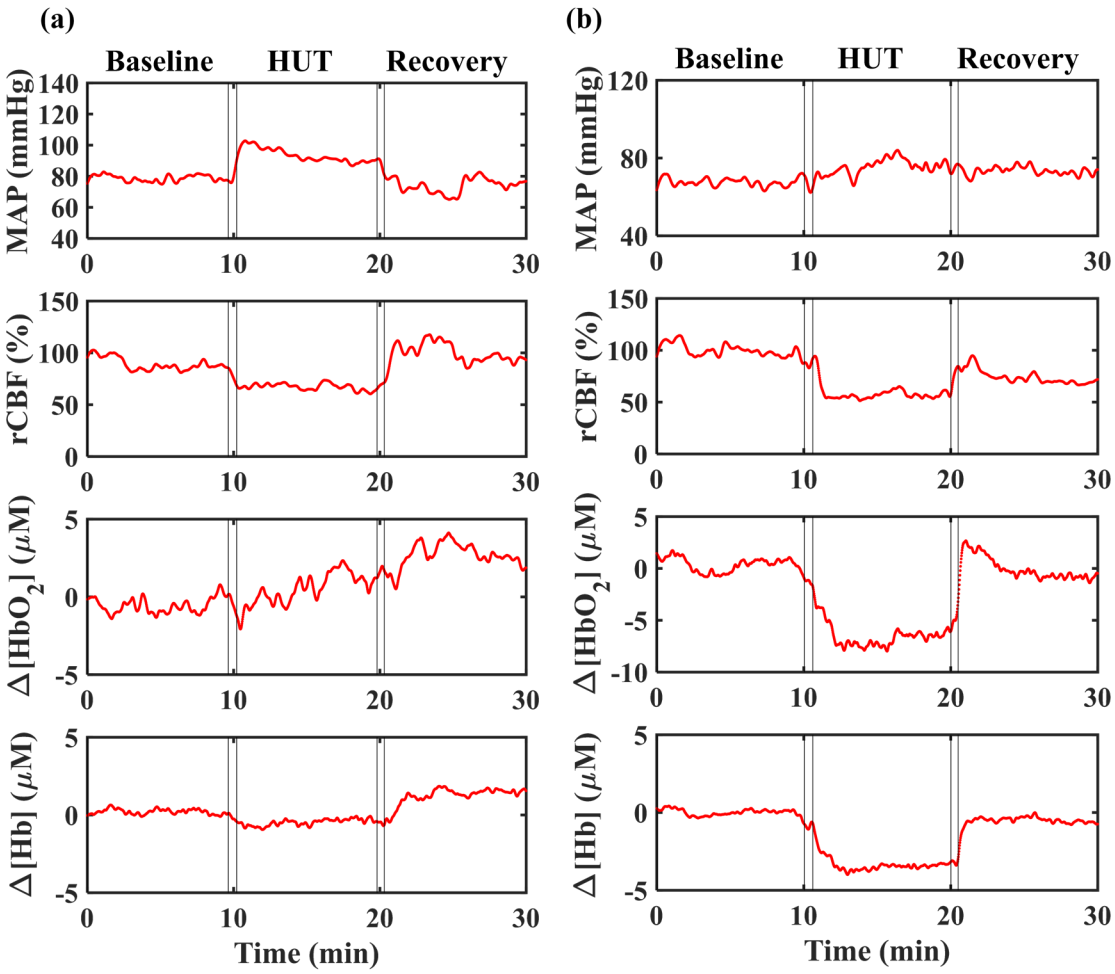

Figure 4-2: Illustrative time-course responses of MAP (mmHg), rCBF (%), Δ[HbO_2] and Δ[Hb] (μM) in two subjects.

The hemodynamic parameters were measured continuously at resting baseline (10 minutes), during HUT (10 minutes) and after HUT for recovery (10 minutes). **(a)** A 68 years-old female subject with low-risk for developing CVD. **(b)** A 84 years-old female subject with high-risk for developing CVD.

4.3.3 LFOs of MAP, rCBF, Δ[HbO_2] and Δ[Hb]

Fig. 4-3 shows the PSD data calculated from the same two subjects with high or low-risk for CVD (**Fig. 4-2**). For both subjects, PSDs of MAP, rCBF, Δ[HbO_2] and Δ[Hb] varied during HUT and recovered towards their baseline levels after HUT.

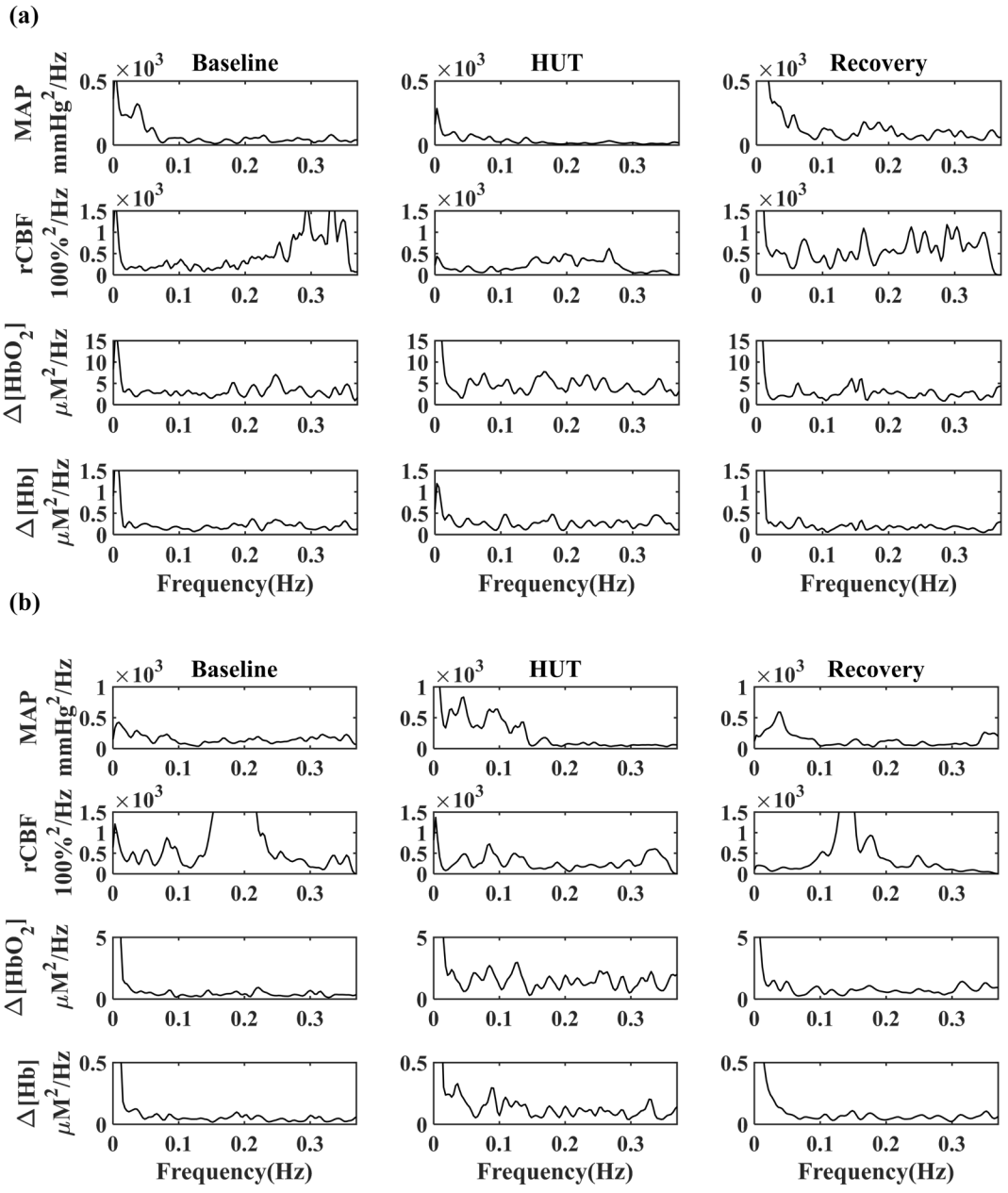

Figure 4-3: LFO intensities of MAP, rCBF, Δ[HbO_2] and Δ[Hb] in two subjects before, during and after HUT.

(a) A 68 years-old female subject with low-risk for developing CVD. **(b)** A 84 years-old female subject with high-risk for developing CVD.

4.3.4 Intergroup and Intragroup Differences in LFO Gains

Fig. 4-4 shows the LFO gain values of different variables (MAP, rCBF, $\Delta[HbO_2]$ and $\Delta[Hb]$) in four frequency intervals (Interval-I to Interval-IV) for two groups (high or low-risk for CVD) under three physiological conditions (at rest, during, and after HUT).

Overall, all LFO gains in the high-risk group were lower than those in the low-risk group, although only some intergroup gain difference reached significance (marked with * and p-values in **Fig. 4-4**, independent t-test).

During HUT, intragroup gains at Interval-I and Interval-II varied (increased or decreased) from their resting baselines. However, most of intragroup gains at Interval-III and Interval-IV reduced, except that the gain of $\Delta[Hb]$ at Interval-III in the high-risk group elevated slightly. Moreover, HUT-induced gain reductions in the high-risk group are generally smaller than those in the low-risk group, although most of these intragroup gain reductions did not reach significance, except the rCBF gain reduction at Interval-IV in the high-risk group (marked with § in **Fig. 4-4**, Wilcoxon signed ranks test, p-value = 0.026).

During recovery, most of LFO gains did not completely recover to their baseline levels, except those at Interval-IV. Interestingly, intragroup and intergroup gain variations across all measured cerebral variables (i.e., rCBF, $\Delta[HbO_2]$ and $\Delta[Hb]$) at Interval-IV were highly consistent. LFO gains decreased during HUT and recovered to their baselines after HUT. Significant intergroup gain differences were observed at rest and during recovery. Moreover, the HUT caused smaller intragroup gain reductions in the high-risk group

compared to the low-risk group, which changed the intergroup gain differences from significant at rest to insignificant during HUT.

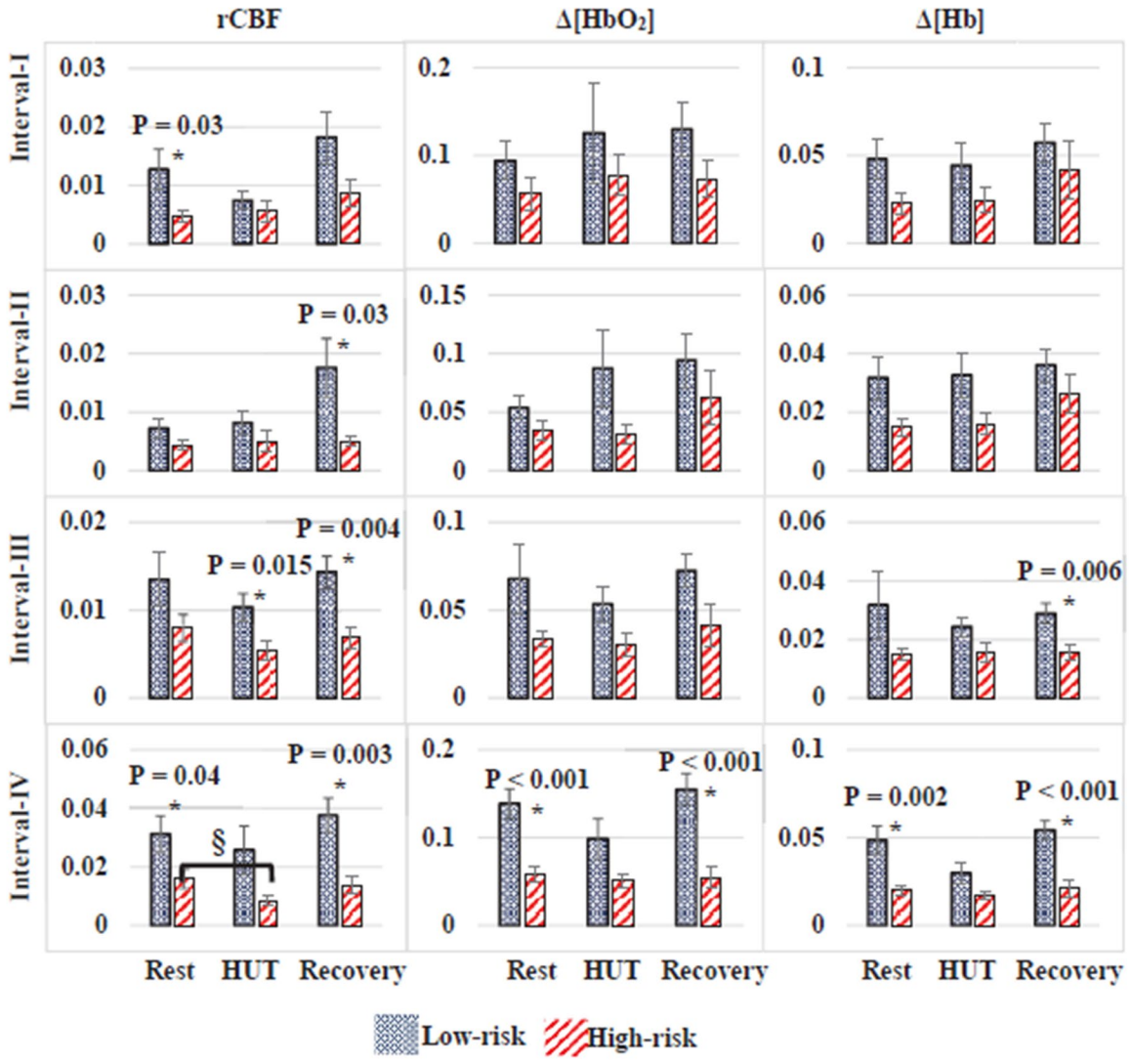

Figure 4-4: LFO gains of MAP, rCBF, Δ[HbO_2] and Δ[Hb] in 4 frequency intervals (Interval-I to Interval-IV).

The presented LFO gains are for two groups (high or low risk for CVD) under 3 physiological conditions (at rest, during resting baseline, HUT, and recovery). * indicates significant differences in intergroup gains (independent t-test). § refers to a significant difference in the intragroup gain (p-value = 0.026, Wilcoxon signed ranks test).

4.4 Discussion

4.4.1 Study Innovations

The goal of the present study is to test whether LFO gains of cerebral hemodynamic variables, quantified by our innovative hybrid optical instrument, are useful biomarkers to distinguish two groups of cognitively healthy older subjects with high or low-risk for developing CVD. Upon comparison with literature [104, 109, 114-120], we believe this study is innovative in that: (1) it used an innovative hybrid optical instrument to simultaneously measure multiple cerebral hemodynamic parameters including rCBF, $\Delta[HbO_2]$ and $\Delta[Hb]$ in cerebral microvasculature. Multiple cerebral functional parameters provided more comprehensive assessment of brain activities than a single parameter alone; (2) it studied a unique population: cognitively healthy older subjects stratified by cerebrovascular risk; and (3) it innovatively explored CAs (extracted from LFO gains of cerebral hemodynamics) as new biomarkers for diagnosis of CVD at preclinical stage.

4.4.2 Interpretation of Intergroup and Intragroup Differences in LFO Gains/CAs

At the resting baseline before HUT, all LFO gains in the high-risk group were relatively lower than those in the low-risk group (**Fig. 4-4**). Particularly, significant intergroup gain differences were observed in all measured cerebral variables (rCBF, $\Delta[HbO_2]$ and $\Delta[Hb]$) at Interval-IV and in rCBF at Interval-I. The relatively lower gains observed in the high-risk group may attribute to enhanced steady-state cerebrovascular reactivity, metabolic reserve, or oxygen diffusion [106, 118, 126, 127], which act as compensatory mechanisms to maintain the CA. HUT generated MAP fluctuations to challenge the CA. As a result, intragroup gains at Interval-I and Interval-II fluctuated (increased or decreased) from their resting baselines. However, most of intragroup gains at Interval-III and Interval-IV were reduced, suggesting potentially stronger dynamic CAs

during HUT compared to rest. Moreover, HUT-induced gain reductions at Interval-III and Interval-IV in the high-risk group are generally smaller than those in the low-risk group, suggesting potentially weaker dynamic CAs during HUT in this high-risk group [23].

Interestingly at Interval-IV, HUT-induced intragroup and intergroup gain variations were highly consistent across all measured cerebral variables (i.e., rCBF, $\Delta[HbO_2]$ and $\Delta[Hb]$): LFO gains decreased from their baselines during HUT and recovered to their baselines after HUT. Moreover, intergroup gain differences were significant at rest and during recovery. However, all intergroup gain differences became insignificant during HUT due to different degrees of intragroup gain reductions. These results confirmed weaker dynamic CAs (corresponding to smaller gain reductions) during HUT in the high-risk group compared to the low-risk group.

We speculate from these results that cerebrovascular risk affects primarily neurogenic and myogenic activities to regulate CA, as Interval-III and Interval-IV correspond respectively to neurogenic and myogenic related metabolic activities [106, 111, 112]. This speculation is supported by other studies in aging populations where neurogenic and myogenic activities at Interval-III and Interval-IV were the substantial regulatory factors for the CA in contrast to endothelial activities at Interval-I and Interval-II [109, 115]. In addition, cerebrovascular risk seems affecting rCBF more than $\Delta[HbO_2]$ and $\Delta[Hb]$, as more intergroup and intragroup differences were observed in rCBF than other two variables (**Fig. 4-4**).

One important finding from this study is that cerebrovascular risk alters steady-state and dynamic CAs differently in cognitively healthy older subjects. As a result, the high-risk group has stronger CA at rest but weaker dynamic CA during HUT. Interestingly,

previous studies have observed that CAs were impaired in patients with symptomatic carotid occlusion or ischemic stroke [104, 119, 120], but preserved in patients with AD [116]. Accordingly, one potential future application is to use the innovative technologies/protocols established in this study to investigate the differences in CAs as biomarkers to differentiate subjects under different conditions such as high-risk for CVD, CVD (e.g., symptomatic carotid occlusion or ischemic stroke), AD, and CVD plus AD. It is crucial to know whether the cognitive deficit is caused by AD or by related vascular problem, so that clinicians can make effective treatment plan accordingly. Unlike AD, there are treatments available for controlling vascular conditions.

4.4.3 Study Challenges and Limitations

One major limitation of this study is the small number of subjects, which affects our statistical analyses and study power. With only two male subjects included in this study, for example, it is impossible to test gender influence on our results. Moreover, the methodology – simultaneously measure multiple cerebral hemodynamic parameters with hybrid optical instrument during HUT to identify new biomarkers (LFO gains) for diagnosis of CVD at preclinical stage, is very unique to compare with other results. In addition, the sampling frequency of the hybrid NIRS/DCS instrument is relatively low (0.7 Hz), which limits the extraction of LFOs in other intervals with higher frequencies such as respiration (0.15-0.5 Hz) and cardiac (0.5-2 Hz) activities [111, 128, 129]. While HUT creates orthostatic stress to challenge the CA, it may also cause syncope, as observed from one participant in this study.

To improve the sampling rate of optical measurements, we recently worked on a fast DCS technique using a software correlator (instead of a conventional hardware

correlator) [130] to create a frame of CBF measurement within only 0.05 seconds. We also explored adding a 785 nm notch filter in front of the Imagent detector so that both DCS and Imagent data were collected concurrently without light interference across the two measurements. With these improvements, the sampling frequency of NIRS/DCS measurements reached 10 Hz. In addition, we are currently exploring other noninvasive stimuli (e.g., memory tests, CO_2 inhalations) for challenging the CA to avoid syncope during HUT. Ultimately, we expect to study more subjects with the improved instrument and experimental protocols in the future to draw solid conclusions.

4.5 Conclusions

A novel hybrid NIRS/DCS instrument was successfully used to simultaneously detect LFOs of MAP, CBF, [HbO_2] and [Hb] in cognitively healthy older subjects with high or low-risk for developing CVD. The intragroup and intergroup differences in LFO gains were characterized to evaluate CA differences between the low-risk and high-risk groups as CAs correlate inversely with LFO gains. At rest before HUT, LFO gains in the high-risk group were relatively lower than those in the low-risk group. Particularly at Interval-IV, intergroup gain differences reached significance for all measured cerebral variables. The lower baseline gains in the high-risk group may attribute to compensatory mechanisms to maintain stronger steady-state CAs. Moreover, HUT resulted in smaller gain reductions at Interval-III and Interval-IV in the high-risk group compared to the low-risk group.

Particularly at Interval-IV, intergroup gain differences for all measured cerebral variables were significant at rest and after HUT, but insignificant during HUT due to different degrees of intragroup gain reductions. These gain variations induced by HUT

suggest weaker dynamic CAs (corresponding to smaller intragroup gain reductions) in the high-risk group compared to the low-risk group. These results suggest that cerebrovascular risk affects neurogenic and myogenic activities (Interval-III and Interval-IV) more than endothelial activities (Interval-I and Interval-II). In addition, cerebrovascular risk affects rCBF more than $\Delta[HbO_2]$ and $\Delta[Hb]$. Taken together, LFO gains are potentially valuable biomarkers for early diagnosis of CVD based on associations with CAs.

CHAPTER 5. TECHNOLOGICAL IMPROVEMENTS IN THE NIRS/DCS SYSTEM FOR THE STUDY OF CVD

5.1 Introduction

In the previous studies (**Chapter 4**), I presented simultaneous measurements of multiple cerebral hemodynamic parameters with our innovative hybrid NIRS/DCS instrument for the detection of CVD at the preclinical stage. One constrain of that study is the low sampling rate (0.7 Hz), which limits the extraction of signals at the high-frequency band such as respiration (~0.5 Hz) and cardiac (~1 Hz) activities [111, 128]. Moreover, the hybrid fiber-optic probe was restricted to use in glabrate skin such as the forehead.

To improve the sampling rate, I adapted a software correlator in the DCS technique [130] to replace the conventional hardware correlator. I also explored adding a 785 nm notch filter in front of the Imagent detector so that both DCS and Imagent data were collected concurrently without light interference across the two measurements. With these improvements, the sampling frequency of NIRS/DCS measurements reached 10 Hz. Moreover, I designed a new fiber-optic probe with long fiber tips, which can be placed between hairs to collect DCS data from the occipital lobe region.

The new system and fiber-optic probes were tested on two healthy older subjects. CBF and cerebral oxygenation data taken from the frontal lobe and CBF data taken from the occipital lobe were collected continuously using the improved hybrid NIRS/DCS instrument with new fiber-optic probes, at resting baseline and during CO_2 alterations to alter cerebral hemodynamics.

The power spectrum density (PSD) was calculated from the measured variables (CBF, [HbO_2], and [Hb]). With the fast sampling rate (up to 10 Hz), our hybrid NIRS/DCS

instrument can detect respiratory (~0.5 Hz) and cardiac (~1 Hz) events. Also, I demonstrated the feasibility of DCS measurements at the occipital lobe (hirsute areas).

5.2 Materials and Methods

5.2.1 Participants

Two case studies were presented in this chapter to highlight these technical improvements of the hybrid NIRS/DCS system. This study was approved by the University of Kentucky (UK) Institutional Review Board (IRB). The written IRB consent was obtained from each subject before participation. Two cognitively healthy older adults (one female: 77 years and one male: 70 years) were recruited from a well-characterized aging cohort, followed by the Alzheimer's Disease Center (ADC) at the UK Sanders-Brown Center on Aging.

5.2.2 Experimental Protocols

The participant was asked to lie down on her/his left side for installing a DCS probe on the right occipital lobe area. Moreover, a hybrid NIRS/DCS probe was placed on the middle of the forehead (~1 cm) above the eyebrows to avoid frontal air sinuses. An elastic bandage was used to wrap around the head for securing the probe on the head and preventing ambient light influence (**Fig. 5-1a** and **Fig. 5-1b**). These probes were connected to the improved hybrid NIRS/DCS instrument with the fast sampling rate.

A 5%CO_2 protocol was integrated into this study to induce changes in cerebral hemodynamics relative to the baseline. The protocol consisted of a continuous recording of cerebral hemodynamics for a 6-minute baseline, followed by 4 sets of 5%CO_2

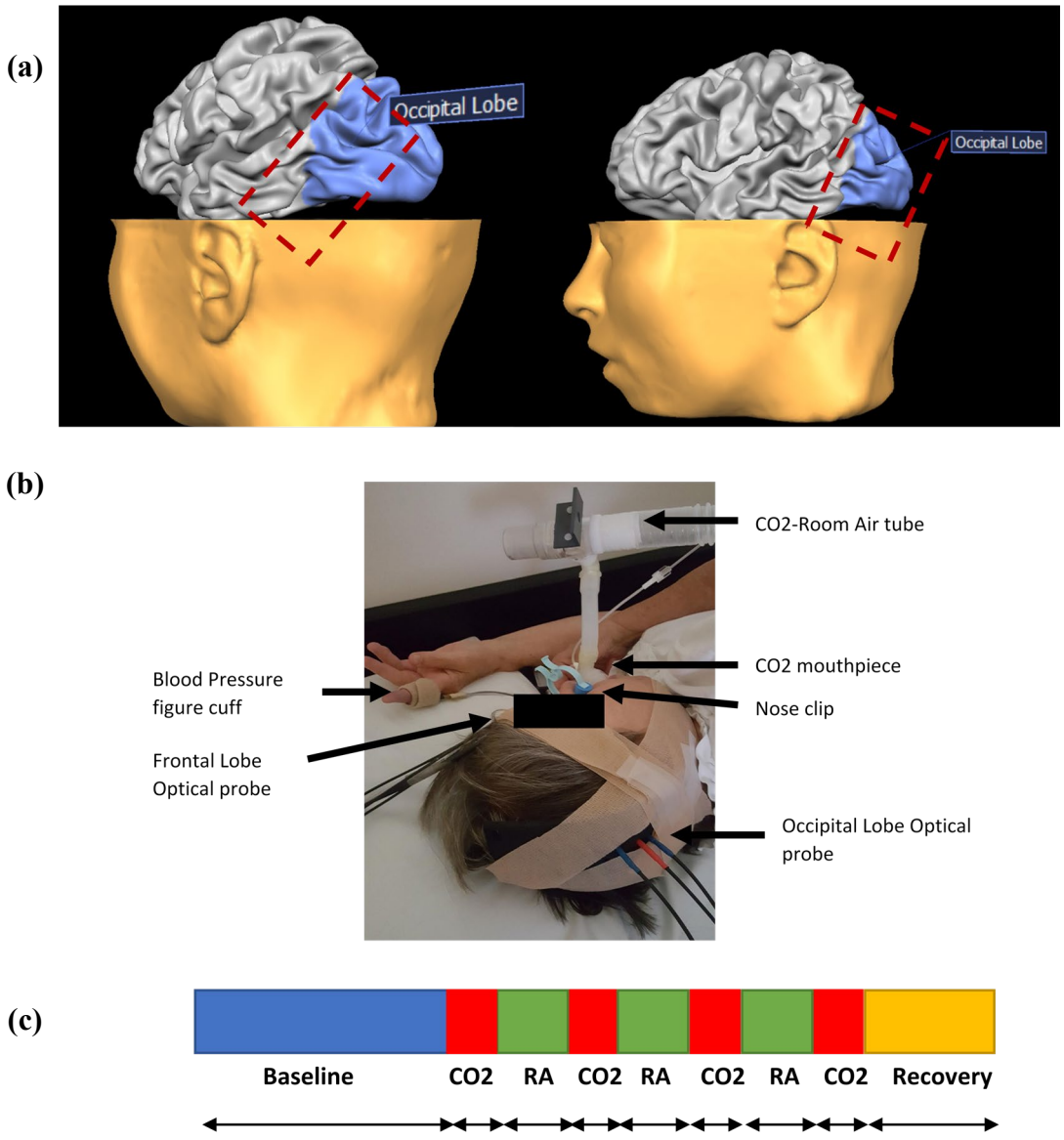

Figure 5-1: CO_2 experimental setup. **(a)** Demonstration of the occipital lobe. **(b)** Measurement setup. **(c)** CO_2 and room air (RA) inhalation protocol, including the baseline (6 minutes), each CO_2 (50 seconds), each RA (70 seconds), and the recovery (3 minutes).

sequentially with an interval of room air inhalation, and then a total of 3 minutes recovery (**Fig. 5-1c**). The CO_2 inhalation was done thorough a mouthpiece connected to an airbag with a mixture gas of 5%CO_2, 21%O_2, and 74%N_2. The alteration between inhaled room air and 5%CO_2 was controlled manually. A nose clip was used to ensure the inhalation and expiration through the mouth only. A CO_2 monitor (Philips NM3, Philips Healthcare) was used to monitor CO_2 end-expiration during the measurement period.

5.2.3 Fast DCS Software Correlator

DCS principle and instruments have been described in **Chapter 4**. Conventional DCS uses an autocorrelator board (Correlator.com, NJ, USA) to calculate the normalized light intensity temporal autocorrelation function (g_2) (**Fig. 5-2a**) [123, 131-133]. From g_2, the electric field temporal autocorrelation function (g_1) is derived via the Siegert relation. The blood flow index (BFI) is then obtained by fitting the measured g_2 to the calculated one based on the correlation diffusion equation [123, 131-133].

More recently, a new method with the software correlator was reported to improve the sampling rate of DCS up to 20 Hz [130]. Briefly, the intensity of speckle fluctuations on the tissue surface was collected and input to the computer via a fast counter board (PCIe-6612 with internal time-base 80 MHz, NI, USA). A shift-and-add analytical method substituted the hardware correlator to compute g_2 function. The g_2 computation depended only on a few delay timepoints (e.g., 40 points in the upper segment of g_2 curve) instead of the full dataset (> 250 points) with the hardware correlator, thus significantly reduced the sampling time. Studies have verified that the upper segment of g_2 curve carries sufficient information for CBF measurements in biological tissues [130, 134, 135]. With this

improvement, the sampling rate of our new DCS with software correlator reached up to 20 Hz.

I adapted and optimized the new software correlator method for my study. The original design utilized two counter boards: one for 8 detection channels and another for the sampling clock. In my design, I utilized one of the 8 channels on a counter board for the sampling clock and the remaining 7 channels on the same board for 7 parallel detections (**Fig. 5-2b**). Therefore, using two counter boards, the number of detection channels was increased from 8 to 15. This allowed us to connect two fiber-optic probes to these channels for simultaneous measurements of frontal and occipital lobes. I also modified the graphic interface (LabVIEW) to control the DCS instrument for multiple channel measurements.

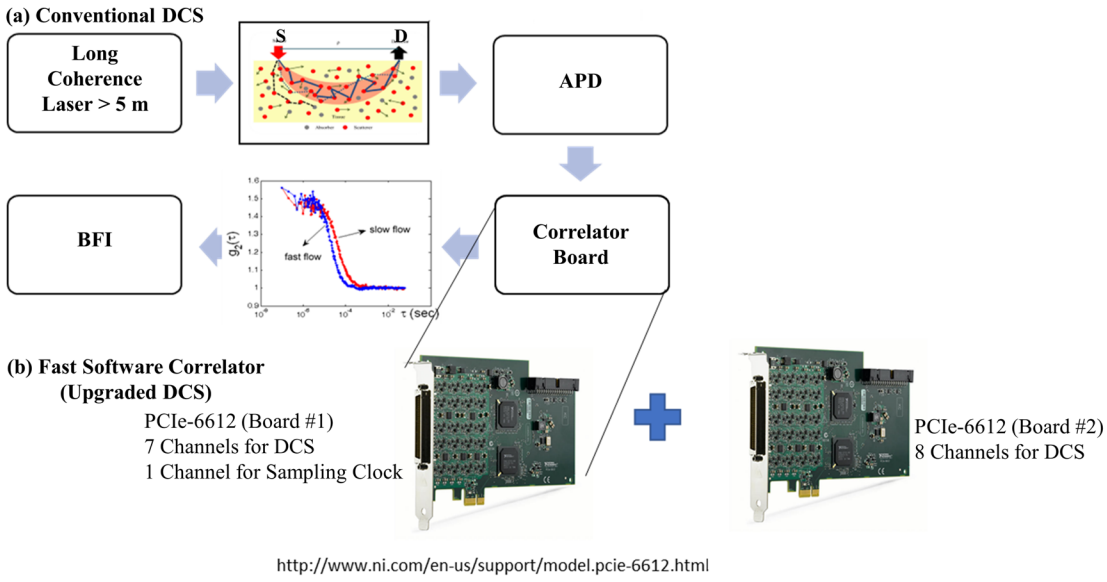

Figure 5-2: Schematic diagram for both conventional and improved DCS machines. (a) a block diagram for the traditional DCS. (b) a block diagram for the enhanced DCS.

5.2.4 Fast Hybrid NIRS/DCS Instrument with Parallel Detection

Previously, our hybrid NIRS/DCS collected data sequentially to avoid light interference between the blood flow and oxygenation measurements. The synchronization between NIRS and DCS devices was through transistor-transistor logic (TTL) triggers (**Fig. 5-3a**), which resulted in a low sampling rate of 0.7 Hz. In this study, I changed the synchronization from the sequential mode to parallel mode (**Fig. 5-3b**). To avoid interference of DCS light at 785 nm on NIRS measurements at 690 and 830 nm, a 780 nm notch filter (Edmund Optics Inc.) was added in front of the Imagent detector. Since Imagent

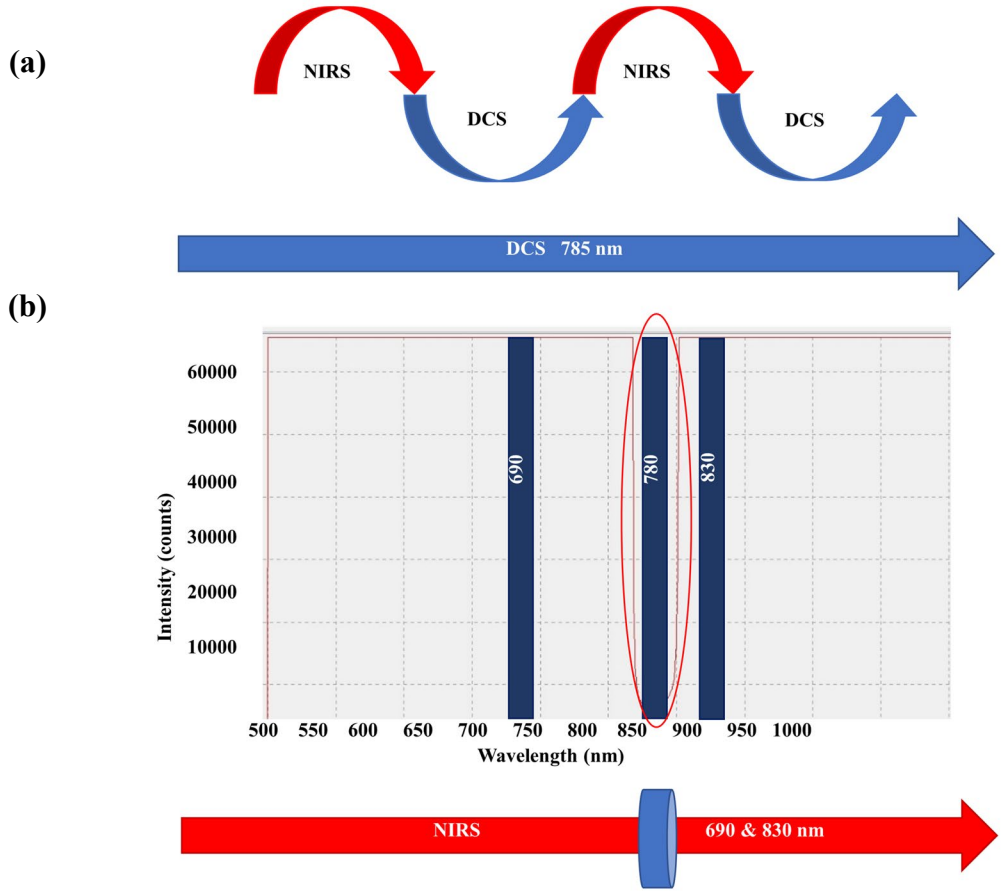

Figure 5-3: A schematic diagram for representing the synchronization modes of NIRS/DCS.

(a) represents the traditional NIRS/DCS sequential synchronization. (b) represents the new synchronization mode (Parallel Mode). The blue cylinder represents a notch filter (785 nm) for blocking the DCS laser source wavelength.

lights at 690 and 830 nm were relatively weak, their influences on DCS measurements were ignorable. With the parallel detection, the sampling rate of hybrid NIRS/DCS measurements reached 10 Hz.

5.2.5 Improved Hybrid NIRS/DCS Probe Design

Fig. 5-4 shows our previous (a) and improved (b) hybrid NIRS/DCS probes. Adding a notch filter to the Imagent detector allowed the DCS source to be placed closer to the Imagent detector, thus generating a better overlap area across the two measurements (NIRS and DCS).

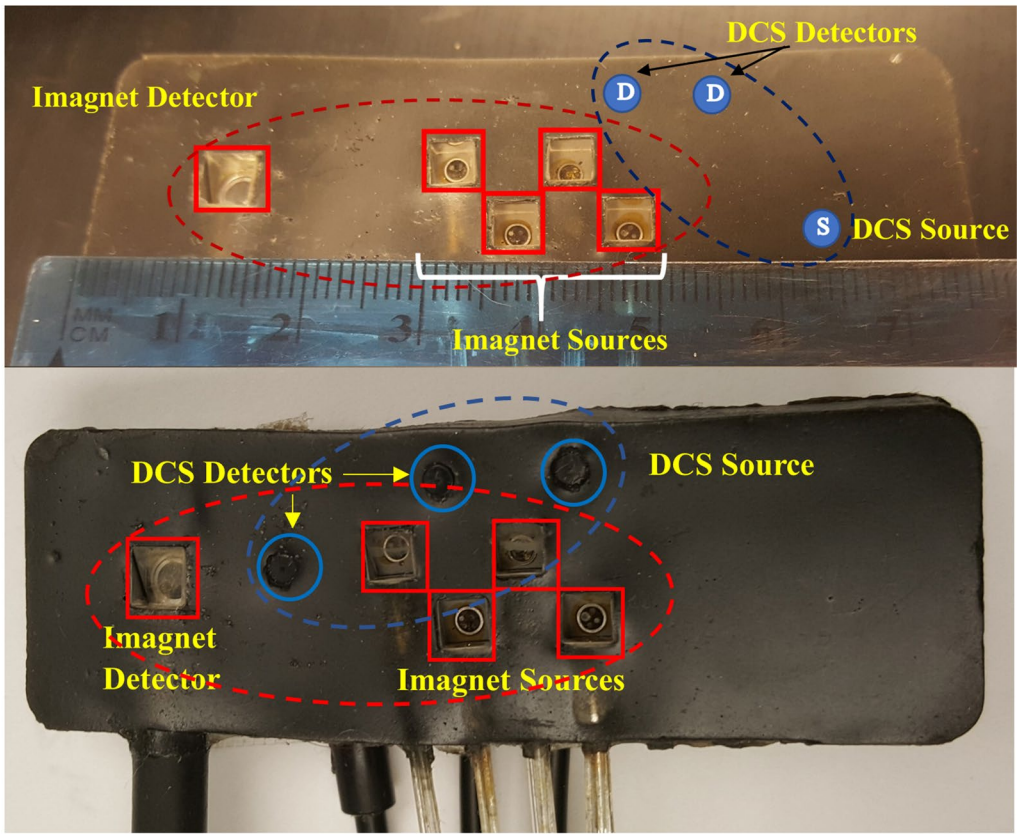

Figure 5-4: Hybrid NIRS/DCS probe design.
(a) Traditional NIRS/DCS probe. (b) Improved NIRS/DCS probe.

5.2.6 Improved DCS Probe Design for Measurement of Occipital Lobe with Hairs

Most of the previous studies including ours with DCS used fiber-optic probes placed on frontal heads without hairs (**Fig. 5-4)**. DCS usually used a single-mode fiber with a diameter of 5.6 μm to detect single speckle contrast on the tissue surface. Hairs could easily block light detected by this single mode fiber [136, 137]. To overcome hair influence, I designed a fiber-optic probe with long tips that can be used on the occipital lobe with hairs (**Fig. 5-5**). The probe had many holes for changing the source-detector separations. The design allowed optical fibers moving around on the occipital lobe to avoid hair blockage. The fiber tip diameter was increased from 2.5 to 5 mm to reduce the pressure of the fiber tip on the skin. Two Velcro taps were integrated into the probe for fixing the probe on the head.

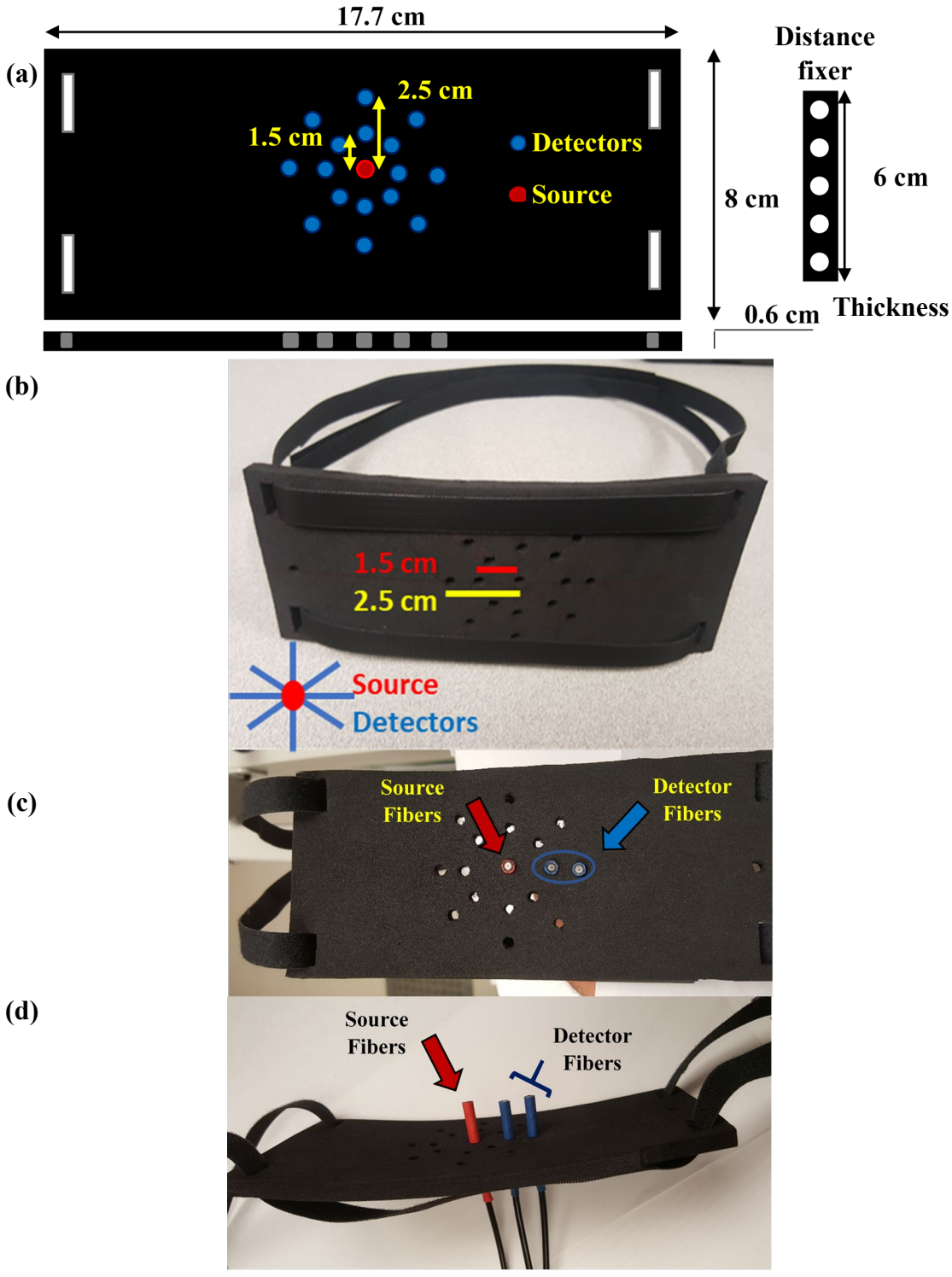

Figure 5-5: The new DCS probe for occipital lobe measurements.
(a) A schematic diagram of the probe design. (b) An overview of the probe. (c) Top view of the probe shows the source and detector fibers. (d) Side view of the probe shows the fibers sliding out the probe for a better visuality to place the fibers on a participant's head between hairs.

5.3 Results

5.3.1 Resting Baseline Autocorrelation Functions Measured by the Fast DCS

Fig. 5-6 shows the autocorrelation curves from two participants measured by our fast DCS devices with the source-detector separation of 2.5 cm on frontal (**Fig. 5-4**) and occipital (**Fig. 5-5**) lobes, respectively at a sampling rate of 3 Hz. Data were averaged respectively from 6 detectors in the frontal lobe and 7 detectors in the occipital lobe. Interestingly, autocorrelation curves collected from the occipital lobe in both two participants are smoother than those from the frontal lobe. That was partially due to the flexible occipital probe (**Fig. 5-5**), which allowed for a better fiber contact with the head. In addition, light intensities detected at occipital lobes were generally stronger than those at frontal lobes. These data demonstrated the feasibility of DCS measurements in the occipital lobe with hairs.

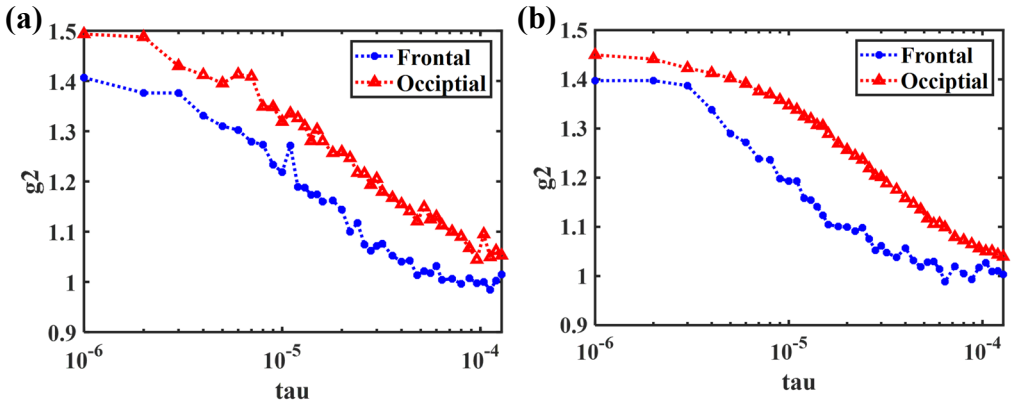

Figure 5-6: The autocorrelation curves (g_2) measured from two participants. (a) Participant 1 (female, 77 years). (b) Participant 2 (male, 70 years).

5.3.2 CBF Responses to CO_2

Fig. 5-7 shows the time-course rCBF data measured by the fast DCS from frontal and occipital lobes, respectively at a sampling rate of 3 Hz. Data were aligned based on CO_2 changes delivered to the participant. rCBF data were normalized to the 30-second baseline right before CO_2 inhalation.

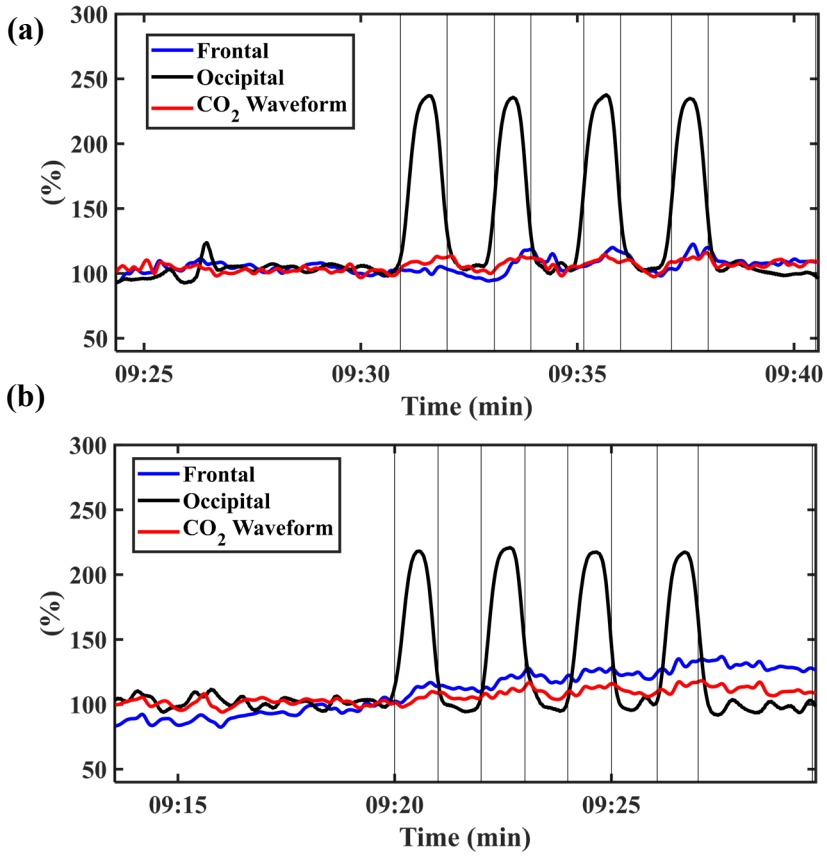

Figure 5-7: Time-course rCBF responses to CO_2 inhalations from two participants. (a) Participant 1 (female, 77 years). (b) Participant 2 (male, 70 years). The data were normalized to the first 30 second right before the first CO_2 cycle.

5.3.3 Cerebral Oxygenation Responses to CO_2

Fig. 5-8 shows the time-course cerebral oxygenation changes ($\Delta[HbO_2]$ and $\Delta[Hb]$) collected from the frontal heads of the two participants.

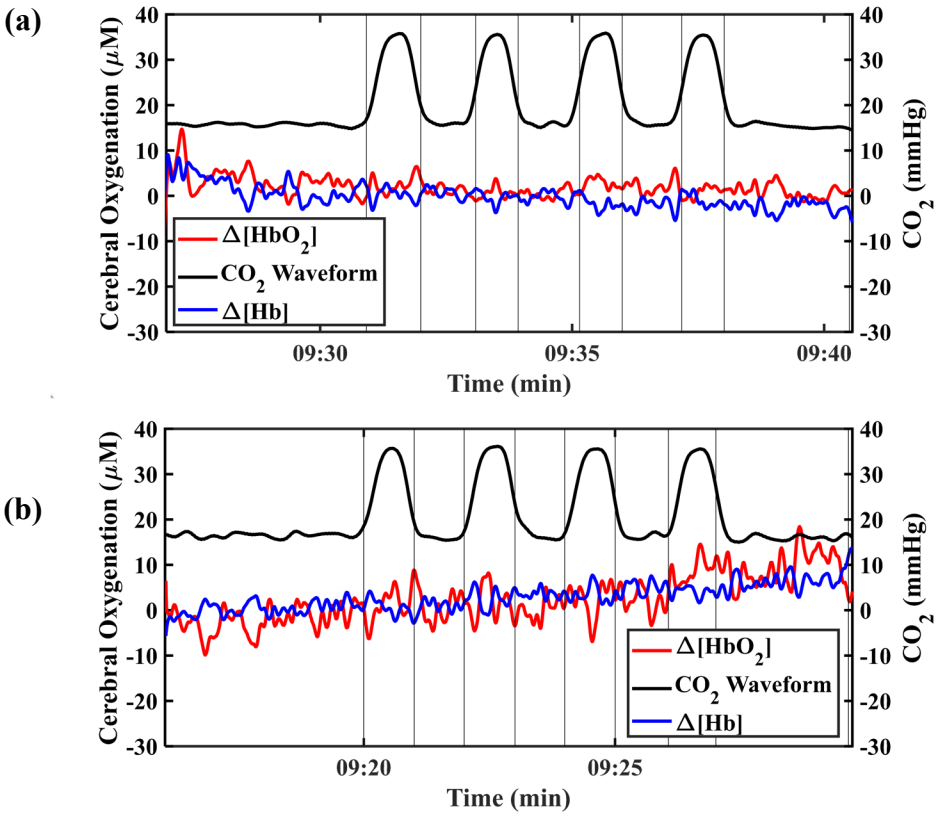

Figure 5-8: Time-course $[HbO_2]$ and [Hb] responses to CO_2 inhalations from two participants.

(a) Participant 1 (female, 77 years). **(b)** Participant 2 (male, 70 years).

5.3.4 Low-Frequency Oscillation Signals

Fig. 5-9 and **Fig. 5-10** show the calculated power spectral density (PSD) of rCBF, $[HbO_2]$ and [Hb] data, obtained from the two participants. The PSDs were computed at the resting baseline, combined CO_2 events, and combined room air events. The CO_2 and room air segments were combined respectively to get sufficient data for each event. The PSD results of the rCBF data show the heart rate component (~1 Hz) more obvious than the

oxygenation parameter due to the direct relationship between the blood flow and heart beating. Moreover, increasing the sampling rate enhanced the detections of low frequency oscillations, compared with our previous results (**Fig. 4-3** in **Chapter 4**).

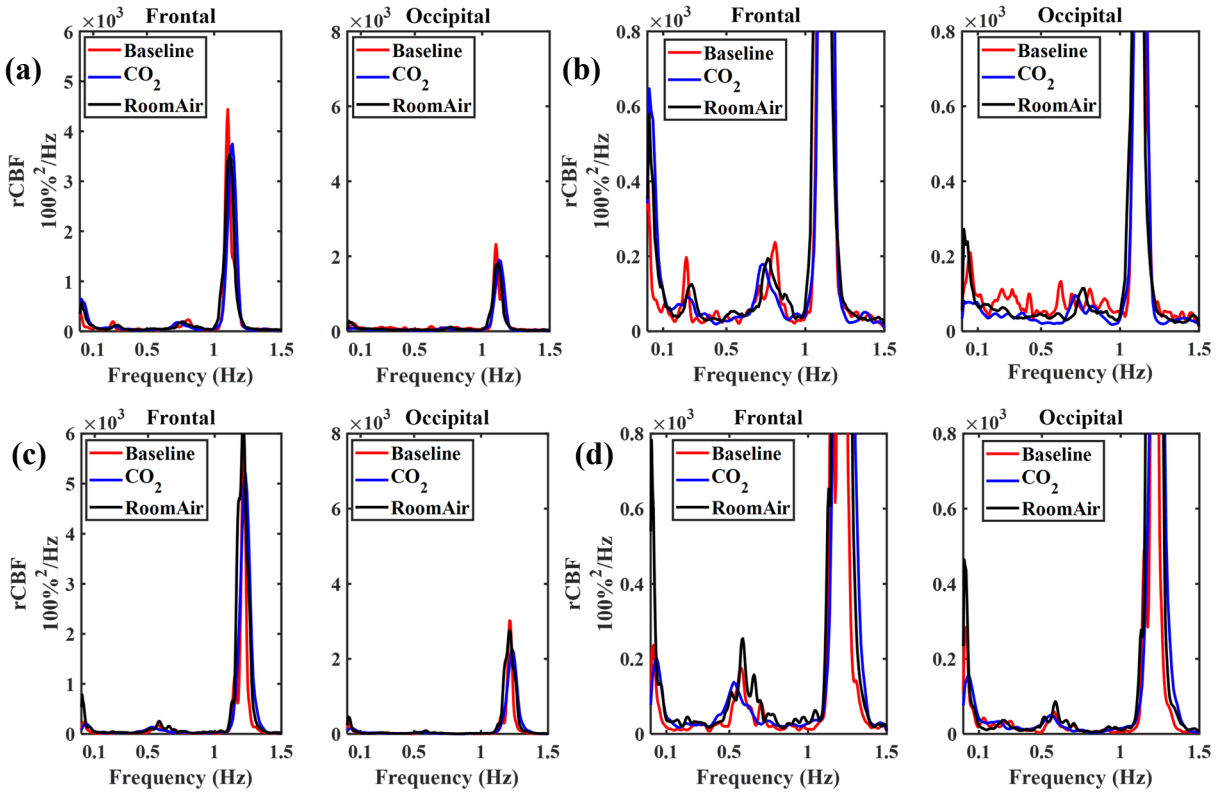

Figure 5-9: The power spectral density (PSD) data of rCBF extracted from the time course data shown in **Fig. 5-7**.

(a) and (b): Participant 1 (female, 77 years). (c) and (d) Participant 2 (male, 70 years). (b) and (d) are zoom-in view of (a) and (c), respectively to show LFOs.

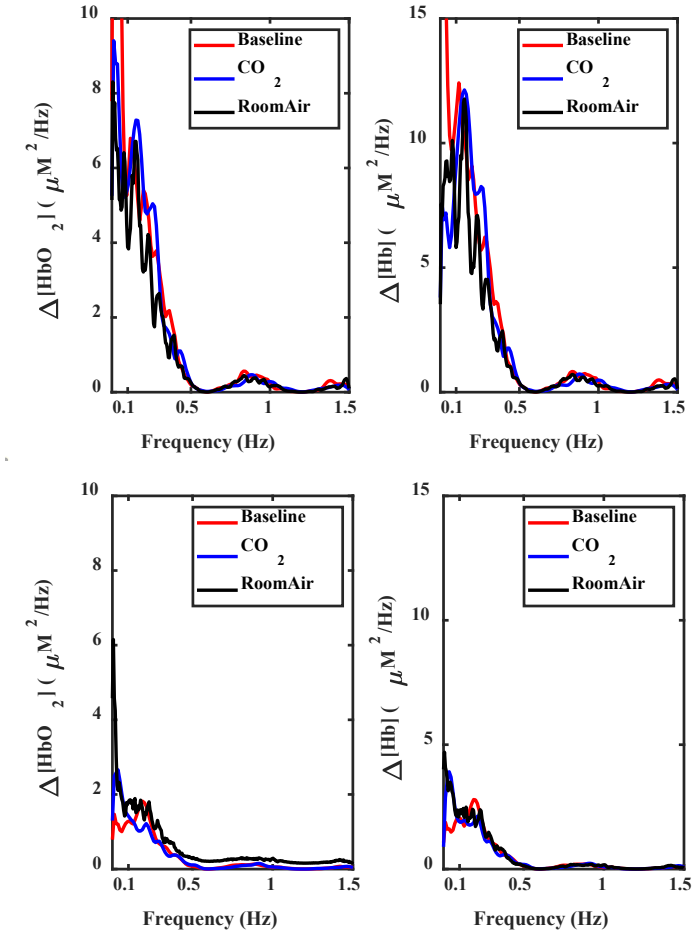

Figure 5-10: The power spectral density (PSD) data of [HbO_2] and [Hb] extracted from the time course data shown in **Fig. 5-8**.

(a) Participant 1 (female, 77 years). **(b)** Participant 2 (male, 70 years).

5.4 Discussions

5.4.1 Study Innovations

This chapter aims to improve the sampling rate of NIRS/DCS and investigate the adaption of DCS for measurements in the occipital lobe with hairs. The study innovations include: (1) adapting and optimizing an innovative software correlator to increase the sampling rate and the number of detection channels; (2) using new parallel synchronization for NIRS/DCS measurements to increase the sampling rate; (3) designing a new DCS probe

to measure CBF at the occipital lobe with hairs; and (4) measuring simultaneously CBF and cerebral oxygenation at both frontal and occipital lobes, for the first time.

5.4.2 Preliminary Result Interpretation

Our preliminary result from two participants demonstrate the improvement in the sampling frequencies for both DCS (using a software correlator) and hybrid NIRS/DCS (using the parallel detection). These improvements enable recording of a large range of frequencies including respiratory and heart beating events. The improvement also facilitates studying high-frequency component of the physiological activities along with low-frequency oscillations (LFOs). Notably, increasing the number of channels (N) of DCS with the fast software correlator also helps to improve the SNR by $\sqrt{N}$ times via averaging signals from multi-channels (N).

Another accomplishment enabled by using the multi-channel parallel detection and new probe is the ability to collect CBF data from discrete areas (i.e., the frontal and occipital lobes). The new occipital probe overcomes the restriction of DCS on glabrate (non-hirsute) areas with a new probe design. This probe can be also upgraded to a hybrid NIRS/DCS probe for simultaneous measurements of CBF and cerebral oxygenation at both the frontal and occipital lobes. Measurements of multiple areas are important to understand the origin and severity of neurodegenerative diseases. For example, cerebral amyloid angiopathy (CAA) in the early stages starts at the posterior part of the brain and then spread out to the front [138, 139].

The CO_2 inhalation causes hypercapnia that induces cerebral vessel dilation as a direct effect of the extracellular H+ on the vascular smooth muscle [140]. The time course data show the interaction between rCBF and CO_2 inhalation as a consequence of

vasodilation effect. Generally, rCBF increased during CO_2 inhalation and decreased during room air. However, we noted that CO_2 inhalation has an accumulative impact (especially within a short alteration time, **Fig. 5-1c**) on CBF, resulting in continuous increase of CBF for both cases (**Fig. 5-7**). By contrast, time course data of cerebral oxygenation in both participants showed relatively smaller changes in response to CO_2 inhalations. Previous studies have found similar CBF and oxygenation variations during CO_2 inhalations, measured by fMRI [141-143] and by manometric technique [144].

LFOs around 0.1 Hz were observed in all measured cerebral hemodynamic parameters (**Fig. 5-9** and **Fig. 5-10**). Due to our high sampling rate (3 Hz), LFOs of rCBF showed higher respiratory peaks at ~0.5 Hz and heart beating peaks at ~1 Hz (**Fig. 5-9**), compared to oxygenation oscillations (**Fig. 5-10**). This is not surprising as blood flow changes are directly related to blood pressure variations. In addition, LFOs of hemodynamic parameters were different at different physiological conditions. LFOs of rCBF decreased during CO_2 inhalation (**Fig. 5-9c** and **Fig. 5-9d**) compared to the baseline and room air inhalations, which are consistent with literature [145].

5.5 Conclusions

The improved NIRS/DCS technologies with parallel detection, high sampling rates, and new probe design allow us, for the first time, to measure both CBF and cerebral oxygenation at frontal and occipital lobes. In the future, more subjects will be studied with the improved technologies to detect cerebral hemodynamic alterations in subjects with cerebral diseases such as CSVD or at the risk for developing cerebral diseases.

CHAPTER 6. STUDY SUMMARY, LIMITATIONS AND FUTURE PERSPECTIVES

6.1 Study Summary

In this thesis work, I tested whether white matter hyperintensities (WMH) and cerebral hemodynamics quantified by the MRI (**Chapter 2**) and a hybrid NIRS/DCS instrument (**Chapter 4**) can be used as biomarkers to distinguish two groups of cognitive healthy older subjects with high or low risk for developing CVD. I found that regional WMH volumes based on associations with cortical and WM CBF values and LFO gains of cerebral hemodynamics based on associations with CAs are potential biomarkers for early detection of CVD.

The high spatial resolution, large penetration depth, and variety of imaging-sequences afforded by MRI make it an appealing imaging modality for evaluation of CSVD, although MRI requires expensive instrumentation and transfer of subjects from bed to imaging facility. By contrast, low-cost, portable, mobile diffuse optical technologies provide a compensatory alternative for early screening of CSVD and continuous monitoring of disease progress at the subject's bedside. In addition, I also developed a standardized protocol for optimizing the post-acquisition processing methods in the MRI to reduce the inter-rater variance (**Chapter 3**) and fast parallel detection technique in the NIRS/DCS to improve the sampling rate (**Chapter 5**). Most of these results have been published or submitted to peer-reviewed journals [20, 146, 147].

My major contributions of these studies are in following aspects. In **Chapter 2**, I participated in the design of the cross-sectional volumetric method for quantifying regional and global WMH and CBF using MRI techniques in cognitively healthy older subjects with high or low risk for developing CVD. I developed methods to segment the WMH and CBF

(ASL) into deep and periventricular regions. Moreover, I successfully registered CBF images to the T1-weighted images for regional segmentations. I ran the full protocol to analyze the data in the study cohort and found that WMHs at deep and periventricular regions had differential associations with CVD and demographic risk factors. Thus, the regional WMH volume is a potentially valuable biomarker for CVD.

In **Chapter 3**, I developed a standardized protocol for optimizing the post-acquisition processing methods in the MRI to reduce the inter-rater variance. I sought to systematically identify sources of variability in WMH-VQ techniques that created challenges for both inter and intra site studies in terms of data comparisons and inference. My study successfully identified the sources of variability, which included specifying the center of the image, software compatibility, method of intensity thresholding, and manual editing. Accordingly, a standardized protocol was presented to minimize the potential sources of bias and variability in WMH volume quantification. While the developed protocol was found to be optimal for use in the present dataset for the detection of subcortical white matter disease, many other protocols exist in the field. Therefore, this protocol may have unique attributes to other specific studies.

In **Chapter 4,** I participated in the data collection using the hybrid NIRS/DCS instrument in cognitive healthy older subjects with high or low risk for developing CVD. My major contribution was to analyze data, summarize results, and draw conclusions. I found that at resting baseline LFO gains in the high-risk group were relatively lower compared to the low-risk group. The lower baseline gains in the high-risk group may attribute to compensatory mechanisms to maintain stronger steady-state CAs. However, HUT resulted in smaller gain reductions in the high-risk group compared to the low-risk

group, suggesting weaker dynamic CAs. Based on these results, LFO gains are potentially valuable biomarkers for early detection of CSVD based on associations with CAs.

In **Chapter 5**, I successfully adapted and optimized a fast DCS technique with a software correlator to increase the sampling rate of DCS measurements up to 20 Hz. I also used a parallel detection technique to increase the sampling rate of NIRS/DCS measurements up to 10 Hz. In addition, I designed a new optical probe to overcome hair influence on DCS measurements for the quantification of CBF on the occipital lobe with hairs.

6.2 Study Limitations and Future Perspectives

There are some limitations in the present study that need to be addressed in future studies. In the current work, the MRI post-processing analysis is semi-automated and time-consuming. Accordingly, moving the method to a fully automatic used in distinct and large cohorts are needed to extend our findings and reduces the sources-of-variability. Moreover, we also need to apply our standardized method (**Chapter 3**) to longitudinal volumetric studies for tracking dynamic changes of WMHs for an advance understanding of the WM lesions.

Current fiber-optic probe on the occipital lobe enables collection of CBF data alone. We will explore integration of NIRS and DCS probes to measure multiple cerebral hemodynamic parameters simultaneously. While HUT creates orthostatic stress to challenge the CA, it may also cause syncope, as observed from one participant in our study. We will explore other noninvasive stimuli (e.g., memory tests, CO_2 inhalations) for challenging the CA to avoid the syncope during HUT.

Future work employing concurrent measurements could allow a comprehensive assessment capturing both MRI, which has a high spatial resolution and NIRS/DCS, which has a high temporal resolution. The optical techniques presented in this dissertation is the CA study, which used a tilting bed to induce CBF and MAP changes to enhance the optical measurement, that is simply incompatible with MRI machine. The technological developments in this dissertation have improved NIRS/DCS techniques to the point where compatible subject positioning is not an issue for simultaneous measurement. Our further experiments will expand on this to explore CSVD changes related to cerebral amyloid angiopathy using both techniques concurrently.

Finally, our studies represent preliminary pilot data that need to be considered with the caveats that the sample size was not large enough to draw definitive conclusions regarding physiological explanations for many of the findings presented. We plan to study more subjects with the improved instruments and experimental protocols in the future to draw solid conclusions.

APPENDIX: GLOSSARY

Notations/terms	Descriptions
3D	Three dimensional
[Hb]	Deoxy-hemoglobin concentration
[HbO_2]	Oxy-hemoglobin concentration
αDB	Blood flow index (BFI)
T	Correlation delay time
Ma	Absorption coefficient
μs’	Reduced scattering coefficient
ADNI	Alzheimer’s disease neuroimaging initiative
AD	Alzheimer’s disease
ADC	Alzheimer’s disease Center
APD	Avalanche photodiode
ASL	Arterial spin labeling
BET	Brain extraction tool
BOLD	Blood oxygen level-dependent signals
CA	Cerebral autoregulation system
CAA	Cerebral amyloid angiopathy
CCTS	Center for clinical and translational science
CBF	Cerebral blood flow
CBFV	Cerebral blood flow velocity

CO_2	Carbon dioxide
CoG	Center of gravity
CSF	Cerebral spinal fluid
CT-scan	Computed tomography scan
CVD	Cerebrovascular disease
CW	Continuous wave
DCS	Diffuse correlation spectroscopy
dWMH	Deep white matter hyperintensity
FA	Flip angle
FLAIR	Fluid-attenuated inversion recovery;
fMRI	Functional MRI
GM	Gray matter
H+	Hydrogen
Hb	Deoxy-hemoglobin
HbO_2	Oxy-hemoglobin
HUT	Head-up tilting
ICBM	International consortium for brain mapping
IR	Inversion recovery time
IRB	Institutional review board (IRB)
LFO	Low-frequency oscillation
MAP	Mean arterial pressure
MCI	Mild cognitive impairment

MIPAV	Medical image processing analysis and visualization
MPRAGE	Magnetization-prepared rapid-acquisition gradient echo
MRI	Magnetic resonance imaging
N_2	Nitrogen
NIRS	Near-infrared spectroscopy
PAD	Peripheral arterial disease
PASL	Pulsed arterial-spin-labeling
PD	Percentage difference
PET	Positron emission tomography
PSD	Power spectral density
pWMH	Periventricular white matter hyperintensity
rCBF	Relative changes in cerebral blood flow
ROI	Region of interest
S-D	Source-detector
SCVD	Small cerebrovascular disease
SD	Standard deviation
SE	Standard error of the mean
SPECT	Single positron emission computed tomography
SWI	Susceptibility-weighted imaging
SNR	Signal-to-noise ratio
TCD	Transcranial Doppler ultrasound

TE	Echo time
TIV	Total intracranial volume
TR	Repetition time
TTL	Transistor-transistor logic
UK	University of Kentucky
WM	White matter
WMHs	White matter hyperintensities
WMH-VQ	White matter hyperintensity volume quantification

REFERENCES

[1] L. Pantoni, Cerebral small vessel disease: from pathogenesis and clinical characteristics to therapeutic challenges, Lancet Neurol, 9 (2010) 689-701.

[2] K.D. Kochanek, S.L. Murphy, J. Xu, Elizabeth Arias, Deaths: Final Data for 2017, National Vital Statistics Reports, U.S. DEPARTMENT OF HEALTH AND HUMAN SERVICES, USA, 2019, pp. 1 - 77.

[3] M. Heron, Deaths: Leading Causes for 2017, 2019.

[4] E.J. Benjamin, P. Muntner, A. Alonso, M.S. Bittencourt, C.W. Callaway, A.P. Carson, A.M. Chamberlain, A.R. Chang, S. Cheng, S.R. Das, F.N. Delling, L. Djousse, M.S.V. Elkind, J.F. Ferguson, M. Fornage, L.C. Jordan, S.S. Khan, B.M. Kissela, K.L. Knutson, T.W. Kwan, D.T. Lackland, T.T. Lewis, J.H. Lichtman, C.T. Longenecker, M.S. Loop, P.L. Lutsey, S.S. Martin, K. Matsushita, A.E. Moran, M.E. Mussolino, M. O'Flaherty, A. Pandey, A.M. Perak, W.D. Rosamond, G.A. Roth, U.K.A. Sampson, G.M. Satou, E.B. Schroeder, S.H. Shah, N.L. Spartano, A. Stokes, D.L. Tirschwell, C.W. Tsao, M.P. Turakhia, L.B. VanWagner, J.T. Wilkins, S.S. Wong, S.S. Virani, E. American Heart Association Council on, C. Prevention Statistics, S. Stroke Statistics, Heart Disease and Stroke Statistics-2019 Update: A Report From the American Heart Association, Circulation, 139 (2019) e56-e528.

[5] A.J. Catto, P.J. Grant, Risk factors for cerebrovascular disease and the role of coagulation and fibrinolysis, Blood Coagul Fibrinolysis, 6 (1995) 497-510.

[6] E.V. Backhouse, C.A. McHutchison, V. Cvoro, S.D. Shenkin, J.M. Wardlaw, Early life risk factors for cerebrovascular disease: A systematic review and meta-analysis, Neurology, 88 (2017) 976-984.

[7] S. Shams Vahdati, A. Ala, S.A. Mousavi Aghdas, A. Adib, M. Mirza-Aghazadeh-Attari, F. Aliar, Association Between the Subtypes of Stroke and the Various Risk Factors of Cerebrovascular Accidents: A Cross-Sectional Study, Eurasian J Med, 50 (2018) 86-90.

[8] C. Hajat, R. Dundas, J.A. Stewart, E. Lawrence, A.G. Rudd, R. Howard, C.D. Wolfe, Cerebrovascular risk factors and stroke subtypes: differences between ethnic groups, Stroke, 32 (2001) 37-42.

[9] L.R. Mikael, A.M.G. Paiva, M.M. Gomes, A.L.L. Sousa, P. Jardim, P.V.O. Vitorino, M.B. Euzebio, W.M. Sousa, W.K.S. Barroso, Vascular Aging and Arterial Stiffness, Arq Bras Cardiol, 109 (2017) 253-258.

[10] R.N. Kalaria, T. Erkinjuntti, Small vessel disease and subcortical vascular dementia, J Clin Neurol, 2 (2006) 1-11.

[11] P. Yilmaz, M.K. Ikram, W.J. Niessen, M.A. Ikram, M.W. Vernooij, Practical Small Vessel Disease Score Relates to Stroke, Dementia, and Death, Stroke, 49 (2018) 2857-2865.

[12] D. A. Cohen, Sleep Disorders Associated with Dementia, Therapy in Sleep Medicine2012, pp. 656-665.

[13] B.B.L.a.J. Biller, Neurovascular System, Textbook of Clinical Neurology, Elsevier Inc2007, pp. 405-434.

[14] D. Renard, G. Castelnovo, A. Wacongne, A. Le Floch, E. Thouvenot, J. Mas, A. Gabelle, P. Labauge, S. Lehmann, Interest of CSF biomarker analysis in possible cerebral amyloid angiopathy cases defined by the modified Boston criteria, J Neurol, 259 (2012) 2429-2433.

[15] R.G. Abramson, K.R. Burton, J.P. Yu, E.M. Scalzetti, T.E. Yankeelov, A.B. Rosenkrantz, M. Mendiratta-Lala, B.J. Bartholmai, D. Ganeshan, L. Lenchik, R.M. Subramaniam, Methods and challenges in quantitative imaging biomarker development, Acad Radiol, 22 (2015) 25-32.

[16] K.J. Ferguson, V. Cvoro, A.M.J. MacLullich, S.D. Shenkin, P.A.G. Sandercock, E. Sakka, J.M. Wardlaw, Visual Rating Scales of White Matter Hyperintensities and Atrophy: Comparison of Computed Tomography and Magnetic Resonance Imaging, J Stroke Cerebrovasc Dis, 27 (2018) 1815-1821.

[17] J. Tamangani, Neuroimaging, Aust Fam Physician, 45 (2016) 788-792.

[18] T. Ssali, U.C. Anazodo, J.D. Thiessen, F.S. Prato, K. St Lawrence, A Noninvasive Method for Quantifying Cerebral Blood Flow by Hybrid PET/MRI, J Nucl Med, 59 (2018) 1329-1334.

[19] K. Farid, S. Petras, V. Ducasse, S. Chokron, G. Helft, J. Blacher, N. Caillat-Vigneron, Brain perfusion SPECT imaging and acetazolamide challenge in vascular cognitive impairment, Nucl Med Commun, 33 (2012) 571-580.

[20] A.A. Bahrani, D.K. Powell, G. Yu, E.S. Johnson, G.A. Jicha, C.D. Smith, White Matter Hyperintensity Associations with Cerebral Blood Flow in Elderly Subjects Stratified by Cerebrovascular Risk, J Stroke Cerebrovasc Dis, 26 (2017) 779-786.

[21] B.J. MacIntosh, N. Filippini, M.A. Chappell, M.W. Woolrich, C.E. Mackay, P. Jezzard, Assessment of arterial arrival times derived from multiple inversion time pulsed arterial spin labeling MRI, Magn Reson Med, 63 (2010) 641-647.

[22] J.C. Ferre, E. Bannier, H. Raoult, G. Mineur, B. Carsin-Nicol, J.Y. Gauvrit, Arterial spin labeling (ASL) perfusion: techniques and clinical use, Diagn Interv Imaging, 94 (2013) 1211-1223.

[23] B.L. Edlow, M.N. Kim, T. Durduran, C. Zhou, M.E. Putt, A.G. Yodh, J.H. Greenberg, J.A. Detre, The effects of healthy aging on cerebral hemodynamic responses to posture change, Physiol Meas, 31 (2010) 477-495.

[24] M. Marinoni, A. Ginanneschi, P. Forleo, L. Amaducci, Technical limits in transcranial Doppler recording: inadequate acoustic windows, Ultrasound Med Biol, 23 (1997) 1275-1277.

[25] E.M. Buckley, A.B. Parthasarathy, P.E. Grant, A.G. Yodh, M.A. Franceschini, Diffuse correlation spectroscopy for measurement of cerebral blood flow: future prospects, Neurophotonics, 1 (2014).

[26] T. Durduran, A.G. Yodh, Diffuse correlation spectroscopy for non-invasive, micro-vascular cerebral blood flow measurement, NeuroImage, 85 Pt 1 (2014) 51-63.

[27] M.N. Kim, T. Durduran, S. Frangos, B.L. Edlow, E.M. Buckley, H.E. Moss, C. Zhou, G. Yu, R. Choe, E. Maloney-Wilensky, R.L. Wolf, M.S. Grady, J.H. Greenberg, J.M. Levine, A.G. Yodh, J.A. Detre, W.A. Kofke, Noninvasive measurement of cerebral blood flow and blood oxygenation using near-infrared and diffuse correlation spectroscopies in critically brain-injured adults, Neurocrit Care, 12 (2010) 173-180.

[28] A.S. Go, D. Mozaffarian, V.L. Roger, E.J. Benjamin, J.D. Berry, M.J. Blaha, S. Dai, E.S. Ford, C.S. Fox, S. Franco, H.J. Fullerton, C. Gillespie, S.M. Hailpern, J.A. Heit, V.J. Howard, M.D. Huffman, S.E. Judd, B.M. Kissela, S.J. Kittner, D.T. Lackland, J.H. Lichtman, L.D. Lisabeth, R.H. Mackey, D.J. Magid, G.M. Marcus, A. Marelli, D.B.

Matchar, D.K. McGuire, E.R. Mohler, 3rd, C.S. Moy, M.E. Mussolino, R.W. Neumar, G. Nichol, D.K. Pandey, N.P. Paynter, M.J. Reeves, P.D. Sorlie, J. Stein, A. Towfighi, T.N. Turan, S.S. Virani, N.D. Wong, D. Woo, M.B. Turner, C. American Heart Association Statistics, S. Stroke Statistics, Heart disease and stroke statistics--2014 update: a report from the American Heart Association, Circulation, 129 (2014) e28-e292.

[29] K.A. Jellinger, The pathology of ischemic-vascular dementia: an update, J Neurol Sci, 203-204 (2002) 153-157.

[30] A.M. Brickman, A. Zahra, J. Muraskin, J. Steffener, C.M. Holland, C. Habeck, A. Borogovac, M.A. Ramos, T.R. Brown, I. Asllani, Y. Stern, Reduction in cerebral blood flow in areas appearing as white matter hyperintensities on magnetic resonance imaging, Psychiatry Res, 172 (2009) 117-120.

[31] A.J. Bastos-Leite, J.P. Kuijer, S.A. Rombouts, E. Sanz-Arigita, E.C. van Straaten, A.A. Gouw, W.M. van der Flier, P. Scheltens, F. Barkhof, Cerebral blood flow by using pulsed arterial spin-labeling in elderly subjects with white matter hyperintensities, AJNR. American journal of neuroradiology, 29 (2008) 1296-1301.

[32] L. Gootjes, S.J. Teipel, Y. Zebuhr, R. Schwarz, G. Leinsinger, P. Scheltens, H.J. Moller, H. Hampel, Regional distribution of white matter hyperintensities in vascular dementia, Alzheimer's disease and healthy aging, Dement Geriatr Cogn Disord, 18 (2004) 180-188.

[33] S. Debette, H.S. Markus, The clinical importance of white matter hyperintensities on brain magnetic resonance imaging: systematic review and meta-analysis, BMJ, 341 (2010) c3666.

[34] M.R. Raman, G.M. Preboske, S.A. Przybelski, J.L. Gunter, M.L. Senjem, P. Vemuri, M.C. Murphy, M.E. Murray, B.F. Boeve, D.S. Knopman, R.C. Petersen, J.E. Parisi, D.W. Dickson, C.R. Jack, Jr., K. Kantarci, Antemortem MRI findings associated with microinfarcts at autopsy, Neurology, 82 (2014) 1951-1958.

[35] J.M. Wardlaw, M. Allerhand, F.N. Doubal, M. Valdes Hernandez, Z. Morris, A.J. Gow, M. Bastin, J.M. Starr, M.S. Dennis, I.J. Deary, Vascular risk factors, large-artery atheroma, and brain white matter hyperintensities, Neurology, 82 (2014) 1331-1338.

[36] R.B. D'Agostino, P.A. Wolf, A.J. Belanger, W.B. Kannel, Stroke risk profile: adjustment for antihypertensive medication. The Framingham Study, Stroke, 25 (1994) 40-43.

[37] C.D.J. Smith, Eleanor S; Van Eldik,,Linda J; Jicha, Gregory A; Schmitt, Frederick A, Nelson, Peter T; Kryscio, Richard J; Murphy, Ronan R, Wellnitz, Clinton V Peripheral (deep) but not Periventricular MRI White Matter Hyperintensities are Increased in Clinical Vascular Dementia Compared to Alzheimer's Disease, DOI (2016).

[38] W.T. Longstreth, Jr., T.A. Manolio, A. Arnold, G.L. Burke, N. Bryan, C.A. Jungreis, P.L. Enright, D. O'Leary, L. Fried, Clinical correlates of white matter findings on cranial magnetic resonance imaging of 3301 elderly people. The Cardiovascular Health Study, Stroke, 27 (1996) 1274-1282.

[39] D. Erten-Lyons, R. Woltjer, J. Kaye, N. Mattek, H.H. Dodge, S. Green, H. Tran, D.B. Howieson, K. Wild, L.C. Silbert, Neuropathologic basis of white matter hyperintensity accumulation with advanced age, Neurology, 81 (2013) 977-983.

[40] A.A. Gouw, A. Seewann, W.M. van der Flier, F. Barkhof, A.M. Rozemuller, P. Scheltens, J.J. Geurts, Heterogeneity of small vessel disease: a systematic review of MRI

and histopathology correlations, Journal of neurology, neurosurgery, and psychiatry, 82 (2011) 126-135.

[41] B. Hooshmand, T. Polvikoski, M. Kivipelto, M. Tanskanen, L. Myllykangas, T. Erkinjuntti, M. Makela, M. Oinas, A. Paetau, P. Scheltens, E.C. van Straaten, R. Sulkava, A. Solomon, Plasma homocysteine, Alzheimer and cerebrovascular pathology: a population-based autopsy study, Brain : a journal of neurology, 136 (2013) 2707-2716.

[42] W.J. Jagust, L. Zheng, D.J. Harvey, W.J. Mack, H.V. Vinters, M.W. Weiner, W.G. Ellis, C. Zarow, D. Mungas, B.R. Reed, J.H. Kramer, N. Schuff, C. DeCarli, H.C. Chui, Neuropathological basis of magnetic resonance images in aging and dementia, Annals of neurology, 63 (2008) 72-80.

[43] B. Kaur, J.J. Himali, S. Seshadri, A.S. Beiser, R. Au, A.C. McKee, S. Auerbach, P.A. Wolf, C.S. DeCarli, Association between neuropathology and brain volume in the Framingham Heart Study, Alzheimer disease and associated disorders, 28 (2014) 219-225.

[44] C.D. Smith, D.A. Snowdon, H. Wang, W.R. Markesbery, White matter volumes and periventricular white matter hyperintensities in aging and dementia, Neurology, 54 (2000) 838-842.

[45] C.D. Smith, D. Snowdon, W.R. Markesbery, Periventricular white matter hyperintensities on MRI: correlation with neuropathologic findings, Journal of neuroimaging : official journal of the American Society of Neuroimaging, 10 (2000) 13-16.

[46] H.M. Abraham, L. Wolfson, N. Moscufo, C.R. Guttmann, R.F. Kaplan, W.B. White, Cardiovascular risk factors and small vessel disease of the brain: blood pressure, white

matter lesions, and functional decline in older persons, J Cereb Blood Flow Metab, DOI 10.1038/jcbfm.2015.121(2015).

[47] T. Gattringer, C. Enzinger, S. Ropele, F. Gorani, K.E. Petrovic, R. Schmidt, F. Fazekas, Vascular risk factors, white matter hyperintensities and hippocampal volume in normal elderly individuals, Dementia and geriatric cognitive disorders, 33 (2012) 29-34.

[48] T. Jeerakathil, P.A. Wolf, A. Beiser, J. Massaro, S. Seshadri, R.B. D'Agostino, C. DeCarli, Stroke risk profile predicts white matter hyperintensity volume: the Framingham Study, Stroke, 35 (2004) 1857-1861.

[49] K. Miwa, M. Tanaka, S. Okazaki, Y. Yagita, M. Sakaguchi, H. Mochizuki, K. Kitagawa, Multiple or mixed cerebral microbleeds and dementia in patients with vascular risk factors, Neurology, 83 (2014) 646-653.

[50] E. Rostrup, A.A. Gouw, H. Vrenken, E.C. van Straaten, S. Ropele, L. Pantoni, D. Inzitari, F. Barkhof, G. Waldemar, The spatial distribution of age-related white matter changes as a function of vascular risk factors--results from the LADIS study, NeuroImage, 60 (2012) 1597-1607.

[51] M. Vuorinen, G. Spulber, S. Damangir, E. Niskanen, T. Ngandu, H. Soininen, M. Kivipelto, A. Solomon, Midlife CAIDE dementia risk score and dementia-related brain changes up to 30 years later on magnetic resonance imaging, J Alzheimers Dis, 44 (2015) 93-101.

[52] R. Wang, L. Fratiglioni, E.J. Laukka, M. Lovden, G. Kalpouzos, L. Keller, C. Graff, A. Salami, L. Backman, C. Qiu, Effects of vascular risk factors and APOE epsilon4 on white matter integrity and cognitive decline, Neurology, 84 (2015) 1128-1135.

[53] R. Wang, L. Fratiglioni, A. Laveskog, G. Kalpouzos, C.H. Ehrenkrona, Y. Zhang, L. Bronge, L.O. Wahlund, L. Backman, C. Qiu, Do cardiovascular risk factors explain the link between white matter hyperintensities and brain volumes in old age? A population-based study, European journal of neurology : the official journal of the European Federation of Neurological Societies, 21 (2014) 1076-1082.

[54] P. Adib-Samii, W. Devan, M. Traylor, S. Lanfranconi, C.R. Zhang, L. Cloonan, G.J. Falcone, F. Radmanesh, K. Fitzpatrick, A. Kanakis, P.M. Rothwell, C. Sudlow, G.B. Boncoraglio, J.F. Meschia, C. Levi, M. Dichgans, S. Bevan, J. Rosand, N.S. Rost, H.S. Markus, Genetic architecture of white matter hyperintensities differs in hypertensive and nonhypertensive ischemic stroke, Stroke; a journal of cerebral circulation, 46 (2015) 348-353.

[55] P. Adib-Samii, N. Rost, M. Traylor, W. Devan, A. Biffi, S. Lanfranconi, K. Fitzpatrick, S. Bevan, A. Kanakis, V. Valant, A. Gschwendtner, R. Malik, A. Richie, D. Gamble, H. Segal, E.A. Parati, E. Ciusani, E.G. Holliday, J. Maguire, J. Wardlaw, B. Worrall, J. Bis, K.L. Wiggins, W. Longstreth, S.J. Kittner, Y.C. Cheng, T. Mosley, G.J. Falcone, K.L. Furie, C. Leiva-Salinas, B.C. Lau, M. Saleem Khan, C. Australian Stroke Genetics, C. Wellcome Trust Case-Control, Metastroke, P. Sharma, M. Fornage, B.D. Mitchell, B.M. Psaty, C. Sudlow, C. Levi, G.B. Boncoraglio, P.M. Rothwell, J. Meschia, M. Dichgans, J. Rosand, H.S. Markus, C. International Stroke Genetics, 17q25 Locus is associated with white matter hyperintensity volume in ischemic stroke, but not with lacunar stroke status, Stroke, 44 (2013) 1609-1615.

[56] D. Carmelli, C. DeCarli, G.E. Swan, L.M. Jack, T. Reed, P.A. Wolf, B.L. Miller, Evidence for genetic variance in white matter hyperintensity volume in normal elderly male twins, Stroke, 29 (1998) 1177-1181.

[57] C. Haffner, R. Malik, M. Dichgans, Genetic factors in cerebral small vessel disease and their impact on stroke and dementia, Journal of cerebral blood flow and metabolism : official journal of the International Society of Cerebral Blood Flow and Metabolism, DOI 10.1038/jcbfm.2015.71(2015).

[58] Q. Lin, W.Q. Huang, C.M. Tzeng, Genetic associations of leukoaraiosis indicate pathophysiological mechanisms in white matter lesions etiology, Reviews in the neurosciences, 26 (2015) 343-358.

[59] M.E. Gurol, A. Viswanathan, C. Gidicsin, T. Hedden, S. Martinez-Ramirez, A. Dumas, A. Vashkevich, A.M. Ayres, E. Auriel, E. van Etten, A. Becker, J. Carmasin, K. Schwab, J. Rosand, K.A. Johnson, S.M. Greenberg, Cerebral amyloid angiopathy burden associated with leukoaraiosis: a positron emission tomography/magnetic resonance imaging study, Ann Neurol, 73 (2013) 529-536.

[60] R.Y. Lo, W.J. Jagust, I. Alzheimer's Disease Neuroimaging, Vascular burden and Alzheimer disease pathologic progression, Neurology, 79 (2012) 1349-1355.

[61] H. Baezner, C. Blahak, A. Poggesi, L. Pantoni, D. Inzitari, H. Chabriat, T. Erkinjuntti, F. Fazekas, J.M. Ferro, P. Langhorne, J. O'Brien, P. Scheltens, M.C. Visser, L.O. Wahlund, G. Waldemar, A. Wallin, M.G. Hennerici, L.S. Group, Association of gait and balance disorders with age-related white matter changes: the LADIS study, Neurology, 70 (2008) 935-942.

[62] A.G. van Norden, K.F. de Laat, R.A. Gons, I.W. van Uden, E.J. van Dijk, L.J. van Oudheusden, R.A. Esselink, B.R. Bloem, B.G. van Engelen, M.J. Zwarts, I. Tendolkar, M.G. Olde-Rikkert, M.J. van der Vlugt, M.P. Zwiers, D.G. Norris, F.E. de Leeuw, Causes and consequences of cerebral small vessel disease. The RUN DMC study: a prospective cohort study. Study rationale and protocol, BMC Neurol, 11 (2011) 29.

[63] R.N. Kalaria, Vascular basis for brain degeneration: faltering controls and risk factors for dementia, Nutr Rev, 68 Suppl 2 (2010) S74-87.

[64] C. Blahak, H. Baezner, L. Pantoni, A. Poggesi, H. Chabriat, T. Erkinjuntti, F. Fazekas, J.M. Ferro, P. Langhorne, J. O'Brien, M.C. Visser, L.O. Wahlund, G. Waldemar, A. Wallin, D. Inzitari, M.G. Hennerici, Deep frontal and periventricular age related white matter changes but not basal ganglia and infratentorial hyperintensities are associated with falls: cross sectional results from the LADIS study, Journal of neurology, neurosurgery, and psychiatry, 80 (2009) 608-613.

[65] P. Kee Hyung, J.Y. Lee, D.L. Na, S.Y. Kim, H.K. Cheong, S.Y. Moon, Y.S. Shim, K.W. Park, B.D. Ku, S.H. Choi, H. Joo, J.S. Lee, S.M. Go, S.H. Kim, S. Kim, K.R. Cha, J. Lee, S.W. Seo, Different associations of periventricular and deep white matter lesions with cognition, neuropsychiatric symptoms, and daily activities in dementia, J Geriatr Psychiatry Neurol, 24 (2011) 84-90.

[66] M.S. Krishnan, J.T. O'Brien, M.J. Firbank, L. Pantoni, G. Carlucci, T. Erkinjuntti, A. Wallin, L.O. Wahlund, P. Scheltens, E.C. van Straaten, D. Inzitari, Relationship between periventricular and deep white matter lesions and depressive symptoms in older people. The LADIS Study, International journal of geriatric psychiatry, 21 (2006) 983-989.

[67] Y. Noh, Y. Lee, S.W. Seo, J.H. Jeong, S.H. Choi, J.H. Back, S.Y. Woo, G.H. Kim, J.S. Shin, C.H. Kim, H. Cho, J.S. Park, J.M. Lee, C.H. Hong, S.Y. Kim, J.H. Lee, S.Y. Kim, K.H. Park, S.H. Han, H.K. Cheong, D.L. Na, A new classification system for ischemia using a combination of deep and periventricular white matter hyperintensities, Journal of stroke and cerebrovascular diseases : the official journal of National Stroke Association, 23 (2014) 636-642.

[68] J.J. Soriano-Raya, J. Miralbell, E. Lopez-Cancio, N. Bargallo, J.F. Arenillas, M. Barrios, C. Caceres, P. Toran, M. Alzamora, A. Davalos, M. Mataro, Deep versus periventricular white matter lesions and cognitive function in a community sample of middle-aged participants, Journal of the International Neuropsychological Society : JINS, 18 (2012) 874-885.

[69] A. Spilt, R. Goekoop, R.G. Westendorp, G.J. Blauw, A.J. de Craen, M.A. van Buchem, Not all age-related white matter hyperintensities are the same: a magnetization transfer imaging study, AJNR. American journal of neuroradiology, 27 (2006) 1964-1968.

[70] J. De Reuck, The human periventricular arterial blood supply and the anatomy of cerebral infarctions, Eur Neurol, 5 (1971) 321-334.

[71] A. Vilar-Bergua, I. Riba-Llena, C. Nafria, A. Bustamante, V. Llombart, P. Delgado, J. Montaner, Blood and CSF biomarkers in brain subcortical ischemic vascular disease: Involved pathways and clinical applicability, J Cereb Blood Flow Metab, 36 (2016) 55-71.

[72] F. De Guio, E. Jouvent, G.J. Biessels, S.E. Black, C. Brayne, C. Chen, C. Cordonnier, F.E. De Leeuw, M. Dichgans, F. Doubal, M. Duering, C. Dufouil, E. Duzel, F. Fazekas, V. Hachinski, M.A. Ikram, J. Linn, P.M. Matthews, B. Mazoyer, V. Mok, B. Norrving, J.T. O'Brien, L. Pantoni, S. Ropele, P. Sachdev, R. Schmidt, S. Seshadri, E.E. Smith, L.A.

Sposato, B. Stephan, R.H. Swartz, C. Tzourio, M. van Buchem, A. van der Lugt, R. van Oostenbrugge, M.W. Vernooij, A. Viswanathan, D. Werring, F. Wollenweber, J.M. Wardlaw, H. Chabriat, Reproducibility and variability of quantitative magnetic resonance imaging markers in cerebral small vessel disease, J Cereb Blood Flow Metab, 36 (2016) 1319-1337.

[73] H.G. Schnack, N.E. van Haren, H.E. Hulshoff Pol, M. Picchioni, M. Weisbrod, H. Sauer, T. Cannon, M. Huttunen, R. Murray, R.S. Kahn, Reliability of brain volumes from multicenter MRI acquisition: a calibration study, Hum Brain Mapp, 22 (2004) 312-320.

[74] J. Ramirez, C.J. Scott, S.E. Black, A short-term scan-rescan reliability test measuring brain tissue and subcortical hyperintensity volumetrics obtained using the lesion explorer structural MRI processing pipeline, Brain Topogr, 26 (2013) 35-38.

[75] L. Pantoni, M. Simoni, G. Pracucci, R. Schmidt, F. Barkhof, D. Inzitari, Visual rating scales for age-related white matter changes (leukoaraiosis): can the heterogeneity be reduced?, Stroke, 33 (2002) 2827-2833.

[76] M. Iorio, G. Spalletta, C. Chiapponi, G. Luccichenti, C. Cacciari, M.D. Orfei, C. Caltagirone, F. Piras, White matter hyperintensities segmentation: a new semi-automated method, Front Aging Neurosci, 5 (2013) 76.

[77] M. Wu, C. Rosano, M. Butters, E. Whyte, M. Nable, R. Crooks, C.C. Meltzer, C.F. Reynolds, 3rd, H.J. Aizenstein, A fully automated method for quantifying and localizing white matter hyperintensities on MR images, Psychiatry Res, 148 (2006) 133-142.

[78] J. Ramirez, A.A. McNeely, C.J.M. Scott, M. Masellis, S.E. Black, I. Alzheimer's Disease Neuroimaging, White matter hyperintensity burden in elderly cohort studies: The

Sunnybrook Dementia Study, Alzheimer's Disease Neuroimaging Initiative, and Three-City Study, Alzheimers Dement, 12 (2016) 203-210.

[79] W.M. van der Flier, H.A. Middelkoop, A.W. Weverling-Rijnsburger, F. Admiraal-Behloul, A. Spilt, E.L. Bollen, R.G. Westendorp, M.A. van Buchem, Interaction of medial temporal lobe atrophy and white matter hyperintensities in AD, Neurology, 62 (2004) 1862-1864.

[80] W. Wen, P. Sachdev, The topography of white matter hyperintensities on brain MRI in healthy 60- to 64-year-old individuals, Neuroimage, 22 (2004) 144-154.

[81] K. Ambarki, A. Wahlin, R. Birgander, A. Eklund, J. Malm, MR imaging of brain volumes: evaluation of a fully automatic software, AJNR. American journal of neuroradiology, 32 (2011) 408-412.

[82] O. Carmichael, C. Schwarz, D. Drucker, E. Fletcher, D. Harvey, L. Beckett, C.R. Jack, Jr., M. Weiner, C. DeCarli, I. Alzheimer's Disease Neuroimaging, Longitudinal changes in white matter disease and cognition in the first year of the Alzheimer disease neuroimaging initiative, Arch Neurol, 67 (2010) 1370-1378.

[83] N. Promjunyakul, D. Lahna, J.A. Kaye, H.H. Dodge, D. Erten-Lyons, W.D. Rooney, L.C. Silbert, Characterizing the white matter hyperintensity penumbra with cerebral blood flow measures, Neuroimage Clin, 8 (2015) 224-229.

[84] D.M. van den Heuvel, V.H. ten Dam, A.J. de Craen, F. Admiraal-Behloul, A.C. van Es, W.M. Palm, A. Spilt, E.L. Bollen, G.J. Blauw, L. Launer, R.G. Westendorp, M.A. van Buchem, P.S. Group, Measuring longitudinal white matter changes: comparison of a visual rating scale with a volumetric measurement, AJNR. American journal of neuroradiology, 27 (2006) 875-878.

[85] F.A. Schmitt, P.T. Nelson, E. Abner, S. Scheff, G.A. Jicha, C. Smith, G. Cooper, M. Mendiondo, D.D. Danner, L.J. Van Eldik, A. Caban-Holt, M.A. Lovell, R.J. Kryscio, University of Kentucky Sanders-Brown healthy brain aging volunteers: donor characteristics, procedures and neuropathology, Curr Alzheimer Res, 9 (2012) 724-733.

[86] C.D. Smith, E.S. Johnson, L.J. Van Eldik, G.A. Jicha, F.A. Schmitt, P.T. Nelson, R.J. Kryscio, R.R. Murphy, C.V. Wellnitz, Peripheral (deep) but not periventricular MRI white matter hyperintensities are increased in clinical vascular dementia compared to Alzheimer's disease, Brain Behav, 6 (2016) e00438.

[87] F. Segonne, A.M. Dale, E. Busa, M. Glessner, D. Salat, H.K. Hahn, B. Fischl, A hybrid approach to the skull stripping problem in MRI, Neuroimage, 22 (2004) 1060-1075.

[88] P. Anbeek, K.L. Vincken, M.J. van Osch, R.H. Bisschops, J. van der Grond, Probabilistic segmentation of white matter lesions in MR imaging, Neuroimage, 21 (2004) 1037-1044.

[89] M.E. Caligiuri, P. Perrotta, A. Augimeri, F. Rocca, A. Quattrone, A. Cherubini, Automatic Detection of White Matter Hyperintensities in Healthy Aging and Pathology Using Magnetic Resonance Imaging: A Review, Neuroinformatics, 13 (2015) 261-276.

[90] H. Xue, L. Srinivasan, S. Jiang, M. Rutherford, A.D. Edwards, D. Rueckert, J.V. Hajnal, Automatic segmentation and reconstruction of the cortex from neonatal MRI, Neuroimage, 38 (2007) 461-477.

[91] D.W. Shattuck, G. Prasad, M. Mirza, K.L. Narr, A.W. Toga, Online resource for validation of brain segmentation methods, Neuroimage, 45 (2009) 431-439.

[92] I. Despotovic, B. Goossens, W. Philips, MRI segmentation of the human brain: challenges, methods, and applications, Comput Math Methods Med, 2015 (2015) 450341.

[93] K.S. M S. Atkins, B. Law, J. Orchard, W. Rosenbaum, Difficulties of T1 brain MRI segmentation techniques, Medical Imaging 2002, SPIE, San Diego, California, United States, 2002.

[94] K. Boesen, K. Rehm, K. Schaper, S. Stoltzner, R. Woods, E. Luders, D. Rottenberg, Quantitative comparison of four brain extraction algorithms, Neuroimage, 22 (2004) 1255-1261.

[95] S.M. Smith, A. Rao, N. De Stefano, M. Jenkinson, J.M. Schott, P.M. Matthews, N.C. Fox, Longitudinal and cross-sectional analysis of atrophy in Alzheimer's disease: cross-validation of BSI, SIENA and SIENAX, Neuroimage, 36 (2007) 1200-1206.

[96] A.N. Hegde, S. Mohan, N. Lath, C.C. Lim, Differential diagnosis for bilateral abnormalities of the basal ganglia and thalamus, Radiographics, 31 (2011) 5-30.

[97] C.C. Lim, Magnetic resonance imaging findings in bilateral basal ganglia lesions, Ann Acad Med Singapore, 38 (2009) 795-798.

[98] O.M. Al-Janabi, A.A. Bahrani, G.A. Jicha, Vascular Contributions to Alzheimer's Disease and Mixed Pathological Disease States, Alzheimer's Disease, Avid Science2017, pp. 2-61.

[99] R. Zhang, J.H. Zuckerman, K. Iwasaki, T.E. Wilson, C.G. Crandall, B.D. Levine, Autonomic neural control of dynamic cerebral autoregulation in humans, Circulation, 106 (2002) 1814-1820.

[100] J.D. Jordan, W.J. Powers, Cerebral autoregulation and acute ischemic stroke, Am J Hypertens, 25 (2012) 946-950.

[101] R. Aaslid, K.F. Lindegaard, W. Sorteberg, H. Nornes, Cerebral autoregulation dynamics in humans, Stroke, 20 (1989) 45-52.

[102] K. Tgavalekos, T. Pham, N. Krishnamurthy, A. Sassaroli, S. Fantini, Frequency-resolved analysis of coherent oscillations of local cerebral blood volume, measured with near-infrared spectroscopy, and systemic arterial pressure in healthy human subjects, PLoS One, 14 (2019) e0211710.

[103] J.R. Whittaker, I.D. Driver, M. Venzi, M.G. Bright, K. Murphy, Cerebral Autoregulation Evidenced by Synchronized Low Frequency Oscillations in Blood Pressure and Resting-State fMRI, Front Neurosci, 13 (2019) 433.

[104] J. Kwan, M. Lunt, D. Jenkinson, Assessing dynamic cerebral autoregulation after stroke using a novel technique of combining transcranial Doppler ultrasonography and rhythmic handgrip, Blood Press Monit, 9 (2004) 3-8.

[105] R. Cheng, Y. Shang, D. Hayes, Jr., S.P. Saha, G. Yu, Noninvasive optical evaluation of spontaneous low frequency oscillations in cerebral hemodynamics, NeuroImage, 62 (2012) 1445-1454.

[106] A. Vermeij, A.S. Meel-van den Abeelen, R.P. Kessels, A.H. van Beek, J.A. Claassen, Very-low-frequency oscillations of cerebral hemodynamics and blood pressure are affected by aging and cognitive load, Neuroimage, 85 Pt 1 (2014) 608-615.

[107] L. Bu, J. Li, F. Li, H. Liu, Z. Li, Wavelet coherence analysis of cerebral oxygenation signals measured by near-infrared spectroscopy in sailors: an exploratory, experimental study, BMJ Open, 6 (2016) e013357.

[108] R. Cui, M. Zhang, Z. Li, Q. Xin, L. Lu, W. Zhou, Q. Han, Y. Gao, Wavelet coherence analysis of spontaneous oscillations in cerebral tissue oxyhemoglobin concentrations and arterial blood pressure in elderly subjects, Microvasc Res, 93 (2014) 14-20.

[109] Q. Tan, M. Zhang, Y. Wang, M. Zhang, B. Wang, Q. Xin, Z. Li, Age-related alterations in phase synchronization of oxyhemoglobin concentration changes in prefrontal tissues as measured by near-infrared spectroscopy signals, Microvasc Res, 103 (2016) 19-25.

[110] G. Xu, M. Zhang, Y. Wang, Z. Liu, C. Huo, Z. Li, M. Huo, Functional connectivity analysis of distracted drivers based on the wavelet phase coherence of functional near-infrared spectroscopy signals, PLoS One, 12 (2017) e0188329.

[111] P. Kvandal, S.A. Landsverk, A. Bernjak, A. Stefanovska, H.D. Kvernmo, K.A. Kirkeboen, Low-frequency oscillations of the laser Doppler perfusion signal in human skin, Microvasc Res, 72 (2006) 120-127.

[112] Z. Li, M. Zhang, Q. Xin, S. Luo, W. Zhou, R. Cui, L. Lu, Assessment of cerebral oxygenation oscillations in subjects with hypertension, Microvasc Res, 88 (2013) 32-41.

[113] H. Obrig, M. Neufang, R. Wenzel, M. Kohl, J. Steinbrink, K. Einhaupl, A. Villringer, Spontaneous low frequency oscillations of cerebral hemodynamics and metabolism in human adults, Neuroimage, 12 (2000) 623-639.

[114] C.G. Riberholt, N.D. Olesen, M. Thing, C.B. Juhl, J. Mehlsen, T.H. Petersen, Impaired Cerebral Autoregulation during Head Up Tilt in Patients with Severe Brain Injury, PLoS One, 11 (2016) e0154831.

[115] M.H. Oudegeest-Sander, A.H. van Beek, K. Abbink, M.G. Olde Rikkert, M.T. Hopman, J.A. Claassen, Assessment of dynamic cerebral autoregulation and cerebrovascular CO2 reactivity in ageing by measurements of cerebral blood flow and cortical oxygenation, Exp Physiol, 99 (2014) 586-598.

[116] A.H. van Beek, J. Lagro, M.G. Olde-Rikkert, R. Zhang, J.A. Claassen, Oscillations in cerebral blood flow and cortical oxygenation in Alzheimer's disease, Neurobiol Aging, 33 (2012) 428 e421-431.

[117] M. Reinhard, E. Wehrle-Wieland, D. Grabiak, M. Roth, B. Guschlbauer, J. Timmer, C. Weiller, A. Hetzel, Oscillatory cerebral hemodynamics--the macro- vs. microvascular level, J Neurol Sci, 250 (2006) 103-109.

[118] J.A. Claassen, B.D. Levine, R. Zhang, Dynamic cerebral autoregulation during repeated squat-stand maneuvers, J Appl Physiol (1985), 106 (2009) 153-160.

[119] H.W. Schytz, A. Hansson, D. Phillip, J. Selb, D.A. Boas, H.K. Iversen, M. Ashina, Spontaneous low-frequency oscillations in cerebral vessels: applications in carotid artery disease and ischemic stroke, J Stroke Cerebrovasc Dis, 19 (2010) 465-474.

[120] D. Phillip, H.W. Schytz, Spontaneous Low Frequency Oscillations in Acute Ischemic Stroke ? A Near Infrared Spectroscopy (NIRS) Study, Journal of Neurology & Neurophysiology, 05 (2014).

[121] Y.L. Lian He, Yu Shang, Brent J. Shelton and Guoqiang Yu, Using optical fibers with different modes to improve the signal-to-noise ratio of diffuse correlation spectroscopy flow-oximeter measurements, Journal of Biomedical Optics, 18 (2013).

[122] W.B. Baker, A.B. Parthasarathy, D.R. Busch, R.C. Mesquita, J.H. Greenberg, A.G. Yodh, Modified Beer-Lambert law for blood flow, Biomed Opt Express, 5 (2014) 4053-4075.

[123] D. Irwin, L. Dong, Y. Shang, R. Cheng, M. Kudrimoti, S.D. Stevens, G. Yu, Influences of tissue absorption and scattering on diffuse correlation spectroscopy blood flow measurements, Biomed Opt Express, 2 (2011) 1969-1985.

[124] C. Huang, Y. Gu, J. Chen, A.A. Bahrani, E.G. Abu Jawdeh, H.S. Bada, K. Saatman, G. Yu, L. Chen, A Wearable Fiberless Optical Sensor for Continuous Monitoring of Cerebral Blood Flow in Mice, IEEE J Sel Top Quantum Electron, 25 (2019).

[125] C. Haddix, A.A. Bahrani, A. Kawala-Janik, W.G. Besio, G. Yu, S. Sunderam, Trial measurement of movement-related cortical dynamics using electroencephalography and diffuse correlation spectroscopy, 22nd International Conference on Methods and Models in Automation and Robotics (MMAR), IEEE, Miedzyzdroje, Poland, 2017, pp. 642-645.

[126] A.H. Van Beek, J.A. Claassen, The cerebrovascular role of the cholinergic neural system in Alzheimer's disease, Behav Brain Res, 221 (2011) 537-542.

[127] J.H.Z. RONG ZHANG, AND BENJAMIN D. LEVINE, Deterioration of cerebral autoregulation during orthostatic stress: insights from the frequency domain, J Appl Physiol, 85 (1998) 1113–1122.

[128] Z. Li, M. Zhang, Q. Xin, S. Luo, R. Cui, W. Zhou, L. Lu, Age-related changes in spontaneous oscillations assessed by wavelet transform of cerebral oxygenation and arterial blood pressure signals, J Cereb Blood Flow Metab, 33 (2013) 692-699.

[129] J. Li, C.S. Poon, J. Kress, D.J. Rohrbach, U. Sunar, Resting-state functional connectivity measured by diffuse correlation spectroscopy, J Biophotonics, 11 (2018).

[130] D. Wang, A.B. Parthasarathy, W.B. Baker, K. Gannon, V. Kavuri, T. Ko, S. Schenkel, Z. Li, Z. Li, M.T. Mullen, J.A. Detre, A.G. Yodh, Fast blood flow monitoring in deep tissues with real-time software correlators, Biomed Opt Express, 7 (2016) 776-797.

[131] G. Yu, T.F. Floyd, T. Durduran, C. Zhou, J. Wang, J.A. Detre, A.G. Yodh, Validation of diffuse correlation spectroscopy for muscle blood flow with concurrent arterial spin labeled perfusion MRI, Opt Express, 15 (2007) 1064-1075.

[132] Y. Shang, L. Chen, M. Toborek, G. Yu, Diffuse optical monitoring of repeated cerebral ischemia in mice, Opt Express, 19 (2011) 20301-20315.

[133] T. Durduran, G. Yu, M.G. Burnett, J.A. Detre, J.H. Greenberg, J. Wang, C. Zhou, A.G. Yodh, Diffuse optical measurement of blood flow, blood oxygenation, and metabolism in a human brain during sensorimotor cortex activation, Opt Lett, 29 (2004) 1766-1768.

[134] Y. Shang, T. Li, L. Chen, Y. Lin, M. Toborek, G. Yu, Extraction of diffuse correlation spectroscopy flow index by integration of Nth-order linear model with Monte Carlo simulation, Appl Phys Lett, 104 (2014) 193703.

[135] Y. Shang, G. Yu, A Nth-order linear algorithm for extracting diffuse correlation spectroscopy blood flow indices in heterogeneous tissues, Appl Phys Lett, 105 (2014) 133702.

[136] O. de Lacharriere, C. Deloche, C. Misciali, B.M. Piraccini, C. Vincenzi, P. Bastien, I. Tardy, B.A. Bernard, A. Tosti, Hair diameter diversity: a clinical sign reflecting the follicle miniaturization, Arch Dermatol, 137 (2001) 641-646.

[137] G. Loussouarn, I. Lozano, S. Panhard, C. Collaudin, C. El Rawadi, G. Genain, Diversity in human hair growth, diameter, colour and shape. An in vivo study on young adults from 24 different ethnic groups observed in the five continents, Eur J Dermatol, 26 (2016) 144-154.

[138] S. Thanprasertsuk, S. Martinez-Ramirez, O.M. Pontes-Neto, J. Ni, A. Ayres, A. Reed, K. Swords, M.E. Gurol, S.M. Greenberg, A. Viswanathan, Posterior white matter disease distribution as a predictor of amyloid angiopathy, Neurology, 83 (2014) 794-800.

[139] S.M. Greenberg, A. Charidimou, Diagnosis of Cerebral Amyloid Angiopathy: Evolution of the Boston Criteria, Stroke, 49 (2018) 491-497.

[140] M.J. Cipolla, Chapter 5, Control of Cerebral Blood Flow, The Cerebral Circulation, Morgan & Claypool Publishers, San Rafael (CA), 2009.

[141] D.A. Yablonskiy, Cerebral metabolic rate in hypercapnia: controversy continues, J Cereb Blood Flow Metab, 31 (2011) 1502-1503.

[142] H. Lu, Y. Ge, Quantitative evaluation of oxygenation in venous vessels using T2-Relaxation-Under-Spin-Tagging MRI, Magn Reson Med, 60 (2008) 357-363.

[143] F. Xu, J. Uh, M.R. Brier, J. Hart, Jr., U.S. Yezhuvath, H. Gu, Y. Yang, H. Lu, The influence of carbon dioxide on brain activity and metabolism in conscious humans, J Cereb Blood Flow Metab, 31 (2011) 58-67.

[144] S.S. Kety, C.F. Schmidt, The Effects of Altered Arterial Tensions of Carbon Dioxide and Oxygen on Cerebral Blood Flow and Cerebral Oxygen Consumption of Normal Young Men, J Clin Invest, 27 (1948) 484-492.

[145] B. Biswal, A.G. Hudetz, F.Z. Yetkin, V.M. Haughton, J.S. Hyde, Hypercapnia reversibly suppresses low-frequency fluctuations in the human motor cortex during rest using echo-planar MRI, J Cereb Blood Flow Metab, 17 (1997) 301-308.

[146] A.A. Bahrani, W. Kong, Y. Shang, C. Huang, C.D. Smith, D.K. Powell, Y. Jiang, A.O. Rayapati, G.A. Jicha, G. Yu, Diffuse Optical Assessment of Cerebral Autoregulation in Older Adults Stratified by Cerebrovascular Risk, J Biophotonics, DOI (2020).

[147] A.A. Bahrani, O.M. Al-Janabi, E.L. Abner, S.H. Bardach, R.J. Kryscio, D.M. Wilcock, C.D. Smith, G.A. Jicha, Post-acquisition processing confounds in brain

volumetric quantification of white matter hyperintensities, J Neurosci Methods, 327 (2019) 108391.

VITA

Ahmed A. Bahrani, Ph.D. Candidate

EDUCATION

Nahrain University, Baghdad, Iraq

Bachelor of Science in Medical Engineering (2003)

Master of Science in Medical Engineering (2006)

University of Kentucky, Kentucky, USA

Ph.D. in Biomedical Engineering, (Current)

PROFESSIONAL POSITIONS/ ACADEMIA

Nahrain University, Iraq

2005 – 2006, Teaching Assistant, Electrical Circuit Lab

University of Baghdad/Department of Biomedical Engineering,

2006-2007, External Lecturer

2007-2009, Faculty Member, Assistant Instructor

2010-2012, Chair of Exam Committee

2011-2012, Director of Students

2011-2012, Faculty Member, Instructor I

University of Kentucky:

2016, Teaching Assistant, College of Engineering

2017 - Current, Graduate Research Assistant, Neuroimaging Analysis, Sanders-Brown Center on Aging

PROFESSIONAL POSITIONS/ INDUSTRY

Al-Bahja Trading Company, Representative of Philips Healthcare Medical Systems/Iraq

2005 – 2007, Senior Sales Engineer

2007 – 2012, Chief of Logistics

SCHOLASTICS & PROFESSIONAL HONORS

Research/Teaching Assistantship/ University of Kentucky

2016, Teaching Assistant, Department of Electrical Engineering

2017, Research Assistant, Supported by NIH Grant

2018, ANA Travel Award, Atlanta, Georgia

2018, ANA Distinguishable Abstract Presentation Award, Atlanta, Georgia

2018, F. Joseph Halcomb III, M.D. Department of Biomedical Engineering Outstanding Graduate Student Award

2018, Research Assistant, Supported by NIH Grant

2019, Research Assistant, Supported by NIH Grant

Travel Awards:

2015, Student Travel Award to BMES Meeting, Graduate School, University of Kentucky

2016, Student Travel Award to BMES Meeting, Department of Biomedical Engineering, University of Kentucky

2017, Student Travel Award to BMES Meeting, Department of Biomedical Engineering, University of Kentucky

2018, Student Travel Award for the 143rd Annual Meeting of the American Neurological Association, ANA

Out of the University of Kentucky

2008 - 2011, (x6) Appreciation Letters from the Dean of Al-Khwarizmi College of Engineering/ University of Baghdad

2009, Jawharat Al-Rafdain Ins. Outstanding Faculty Award, Iraq

2010, Travel Award to the Iraqi-Egyptian Friendship Meeting Week/ Egypt, Ministry of Youth, Iraq

2010, Appreciation Letters from the President of the University of Baghdad

2010, The 4th Congress of Al-Seyada / Youth Ministry of Iraq, Young Researcher Award, 3rd Place

2011, Appreciation Letters from the Minister of Higher Education of Iraq

PEER-REVIEWED JOURNAL PUBLICATIONS

1. M. Dawood and **Ahmed A. Bahrani**, "Breast Tumor Diagnosis Using Diode Laser in Near Infrared Region" Al-Khwarizmi Engineering Journal, Vol. 5, No. 2, PP 20 -31 (2009). Master thesis paper.
2. S. Salman, **Ahmed A. Bahrani**. "Segmentation of Tumor Tissue in Gray Medical Images using Watershed Transformation Method". IJACT, 4, 3 (2010).
3. **Ahmed A. Bahrani**, D. Powell, G. Yu, E. Johnson, G. Jicha, C. Smith, "White Matter Hyperintensity Associations with Cerebral Blood Flow in Elder Subjects Stratified by Cerebrovascular Risk", Journal of Stroke and Cerebrovascular Diseases, 26 (4), 779–786 (2017).
4. O. Al-Janabi, **Ahmed A. Bahrani** and G. Jicha "Chapter 5: Vascular Contributions to Alzheimer's Disease and Mixed Pathological Disease States" Alzheimer's Disease, Avid Science, First Published August 16, (2017). Book Chapter.

5. N. Agochukwu, C. Huang, M. Zhao, **Ahmed A. Bahrani**, L. Chen, P. McGrath, G. Yu, L. Wong, "A Novel Noncontact Diffuse Correlation Spectroscopy for Assessing Blood Flow in Mastectomy Skin Flaps: a Prospective Study in Patients Undergoing Prosthetic Based Reconstruction," Plastic and Reconstructive Surgery, 140(1), 26 (2017).
6. C. Huang, Y. Gu, J. Chen, **A. Bahrani**, E. Abu Jawdeh, H. Bada, G. Yu, L. Chen "A Wearable Fibreless Optical Sensor for Continuous Monitoring of Cerebral Blood Flow in Mice", IEEE photonics, (2018).
7. O. Al-Janabi, C. Brown, **Ahmed A. Bahrani**, E. Abner, J. Barber, B. Gold, L. Goldstein, R. Murphy, P. Nelson, N. Johnson, L. Shaw, C. Smith, J. Trojanowski, D. Wilcock, and G. Jicha, "Distinct White Matter Changes Associated with Cerebrospinal Fluid Amyloid-β1-42 and Hypertension" Journal of Alzheimer's Disease, vol. 66, no. 3, pp. 1095-1104, (2018).
8. S. Mazdeyasna, C. Huang, M. Zhao, N. Agochukwu, **Ahmed A. Bahrani**, L. Wong, G. Yu "Noncontact Speckle Contrast Diffuse Correlation Tomography (scDCT) of Blood Flow Distributions in Tissues with Arbitrary Geometries", Journal of Biomedical Optics, J. of Biomedical Optics, 23(9), 096005 (2018). https://doi.org/10.1117/1.JBO.23.9.096005
9. O. Al-Janabi, P. Panuganti, E. Abner, **Ahmed A**. **Bahrani,** R**.** Murphy, S. Bardach, A. Caban-Holt, P. Nelson, B. Gold, C. Smith, D. Wilcock, and G. Jicha. "Global Cerebral Atrophy Detected by Routine Imaging: Relationship with Age, Hippocampal Atrophy, and White Matter Hyperintensities." Journal of Neuroimaging, (2018). doi:10.1111/jon.12494
10. **Ahmed A. Bahrani**, O. Al-Janabi, E. Abner, R. Kryscio, D. Wilcock, C. Smith, and G. Jicha, "Post-acquisition Processing Confounds in Brain Volumetric Quantification of White Matter Hyperintensities", Journal of Neuroscience Methods, 327, 108391, (2019).
11. N Johnson, **Ahmed A. Bahrani**, D. Powell, G. Jicha, B. Gold, 'Cardiorespiratory Fitness Diminishes the Effects of Age on White Matter Hyperintensity Volume", submitted, (2019).

12. O. Al-Janabi, C. Bauer, L. Goldstein, R. Murphy, **Ahmed A. Bahrani**, C. Smith, D. Wilcock, B. Gold, and G. Jicha, "White Matter Hyperintensity Regression: Comparison of Brain Atrophy and Cognitive Profiles with Progression and Stable Groups", Brain Science, *9*(7), 170, (2019). https://doi.org/10.3390/brainsci9070170.
13. **Ahmed A. Bahrani**, W. Kong, Y. Shang, C. Huang, C. Smith, D. Powell, Y. Jiang, E. Abner, G. Jicha, and G. Yu, "Diffuse Optical Assessment of Cerebral Autoregulation in Older Adults Stratified by Cerebrovascular Risk", Submitted (2020).
14. **Ahmed A. Bahrani**, C. Smith, O. Al-Janabi, D. Powell, A. Andersen, B. Gold, D. Wilcock, and G. Jicha, "Voxel-Wise Tracking of Longitudinal WMH Changes (Progression and Regression) on Aging Population", In the final process before submission, (2020).

CONFERENCE PAPERS and PRESENTATION

1. **TEDx Talk**: **Ahmed A. Bahrani,** Introducing an Image Processing Method to Detect the Brain Tumor Boundaries, TEDx Baghdad, Iraq, (2011).
2. **Conference Paper:** Chase Haddix, **Ahmed A. Bahrani**, A. Kawala-Janik, W. Besio, G. Yu, S. Sunderam, " Trial Measurement of Movement-Related Cortical Dynamics Using Electroencephalography and Diffuse Correlation Spectroscopy," International Conference on Methods and Models in Automation and Robotics (MMAR), Miedzyzdroje, (2017).
3. S. Mazdeyasna, C. Huang, M. Seong, J. Morgan, M. Zhao, **Ahmed A. Bahrani**, J. Kim, J. Hastings, G. Yu, A Novel Low-Cost Compact Diffuse Speckle Contrast Flowmeter for Contact Blood Flow Measurement, BMES Annual Scientific Meeting, Phoenix, AZ, (2017). (Oral).
4. G. Jicha, O. Al-Janabi, **Ahmed A. Bahrani**, E. Abner, P. Panuganti, R. Murphy, S. Bardach, A. Caban-Holt, ' Cerebrovascular Disease and Alzheimer's Disease, but not Age, are Associated with Moderate to Sever Global Cerebral Atrophy Seen on Clinical Brain Imaging Studies" Alzheimer's & Dementia: The Journal of the

Alzheimer's Association , Volume 13 , Issue 7 , P214 - P215 (2017). https://doi.org/10.1016/j.jalz.2017.07.089

5. G. Jicha, O. Al-Janabi, **Ahmed A. Bahrani**, S. Bardach, A. Caban-Holt, R. Murphy, E. Abner, P. Nelson, "Clinical Imaging, Cognitive, and Genetic Risk Profiles in Incident MCI for the Prediction of Ling-Term Neuropathological Outcomes at Autopsy", Alzheimer's & Dementia, Volume 13, Issue 7, P1313 (2017). https://doi.org/10.1016/j.jalz.2017.06.2010
6. **Presentation: Ahmed A. Bahrani, "**Assessing Longitudinal Change in WMH Volumes and Distributions**",** NIH Biomarkers Consortium for Vascular Contributions to Cognitive Impairment and Dementia (MarkVCID), Los Angeles, CA (2018).
7. M. Zhao, C. Huang, D. Irwin, S. Mazdeyasna, **Ahmed A. Bahrani**, N. Agochukwu, L. Wong, G. Yu, EMCCD-Based Speckle Contrast Diffuse Correlation Tomography of Tissue Blood Flow Distribution, Biophotonics Congress: Biomedical Optics, Hollywood, FL, (2018). (Oral)
8. S. Mazdeyasna, C. Huang, M. Zhao, **Ahmed A. Bahrani**, N. Agochukwu, L. Wong, G. Yu, Intraoperative Imaging of Blood Flow Distributions in Mastectomy Skin Flaps using Speckle Contrast Diffuse Correlation Tomography, UK CCTS Spring Conference, Lexington, KY, (2018). (Oral)
9. C. Huang, L. Chen, Y. Gu, J. Chen, **Ahmed A. Bahrani**, and G. Yu, "A Wearable Optical Sensor for Continuous Monitoring of Cerebral Blood Flow in Mice", UK CCTS Spring Conference, Lexington, KY, (2018).
10. D. Irwin, C. Huang, M. Zhao, S. Mazdeyasna, **Ahmed A. Bahrani**, G. Yu, Noncontact Imaging of Flow and Fluorescence Contrasts, UK CCTS Spring Conference, Lexington, KY, (2018). (Oral)
11. **Presentation: Ahmed A. Bahrani, "**WMH Penumbra: Tracking WMH Changes, Longitudinal Study"**,** NIH Biomarkers Consortium for Vascular Contributions to Cognitive Impairment and Dementia (MarkVCID), Boston, MA (2019).

CONFERENCE ABSTRACTS and SEMINARS:

1. C. Huang, **Ahmed A. Bahrani**, W. Kong, Y. Lin, G. Yu, "Noninvasive Evaluation of Cardiovascular Function by a Finger Blood Flow Sensor", University of Kentucky Muscle Biology Fall Retreat, Lexington, KY, (2013).
2. C. Huang, **Ahmed A. Bahrani**, W. Kong, Y. Lin, G. Yu, "Noninvasive Evaluation of Cardiovascular Function by a Finger Blood Flow Sensor", Gill Heart Cardiovascular Research Day, Poster Section, University of Kentucky, Lexington, KY, (2013).
3. **Ahmed A. Bahrani**, C. Smith, David K. Powell, E. Johnson, W. Kong, Y. Shang, Chong Huang, Yang Jiang, R. Kryscio, Peter Nelson, G. Jicha, G. Yu, "Quantification of Cerebral Blood Flow and White Matter Hyperintensity in Older Subjects with Low or High Risk for Cerebrovascular Disease using Functional MRI", BMES Annual Scientific Meeting, Tampa, FL, (2015).
4. **Ahmed A. Bahrani**, C. Smith, D. Powell, E. Johnson, W. Kong, Y. Shang, C. Huang, Y. Jiang, R. Kryscio, P. Nelson, G. Jicha, G. Yu, "Quantification of Cerebral Blood Flow and White Matter Hyperintensity in Older Adults with Low or High Risk for Cerebrovascular Disease using MRI", UK CCTS Spring Conference, Lexington, KY, (2015).
5. **Ahmed A. Bahrani**, O. Al-Janabi, D. Wilcock, C. Smith, and G. Jicha," MRI Quantification Method Source of Variability", Markesbery Symposium on Aging and Dementia, University of Kentucky, (2017).
6. O. Al-Janabi, C. Brown**, Ahmed A. Bahrani**, C. Smith, G. Jicha "Cerebrovascular and Alzheimer's Contribute to Subcortical Ischemic Injury via Independent Rather than Synergistic Mechanisms", ANNALS OF NEUROLOGY, 82, S51-S52 (2017)
7. O. Al-Janabi, C. Brown**, Ahmed A. Bahrani**, R. Murphy, D. Wilcock, B. Gold, L. Goldstien, C. Smith and G. Jicha, "Amyloid Pathology and Hypertension are Associated with White Matter Injury Through Different Mechanisms as Assessed by FLAIR and DTI MRI" Markesbery Symposium on Aging and Dementia, University of Kentucky, (2017).

8. S. Mazdeyasna, C. Huang, N. McGregor*, M. Zhao, **Ahmed A. Bahrani**, G. Yu, A Photometric Stereo Technique to Acquire Tissue Surface Geometry for 3D Imaging of Blood Flow Distributions in Mastectomy Skin Flaps, BMES Annual Scientific Meeting, Phoenix, AZ, (2017).
9. M. Zhao, C. Huang, N. Agochukwu, **Ahmed A. Bahrani**, S. Mazdeyasna, L. Wong, G. Yu, Noncontact Diffuse Correlation Spectroscopy Assessment of Tissue Blood Flow for the Prediction of Mastectomy Skin Flap Necrosis, BMES Annual Scientific Meeting, Phoenix, AZ, (2017).
10. **Ahmed A. Bahrani,** G. Yu, Detection of Resting Spontaneous Low Frequency Oscillations in Cerebral Blood Flow using a Fast Diffuse Correlation Spectroscopy, BMES Annual Scientific Meeting, Phoenix, AZ, (2017).
11. Chase Haddix, **Ahmed A. Bahrani**, A. Kawaka, G. Yu, S. Sunderam, Pilot Study Towards Characterization of Movement-Related Cortical Dynamics using Electroencephalography and Diffuse Correlation Spectroscopy, BMES Annual Scientific Meeting, Phoenix, AZ, (2017).
12. Chase Haddix, **Ahmed A. Bahrani**, A. Kawala-Janik, G. Yu, S. Sunderam, Towards Characterization of Movement-Related Cortical Dynamics using Electroencephalography and Diffuse Correlation Spectroscopy, UK CCTS Spring Conference, Lexington, KY, (2017).
13. **Ahmed A. Bahrani**, G. Yu, Low-frequency Oscillation in Resting Brain Detected by a Fast Diffuse Correlation Spectroscopy, UK CCTS Spring Conference, Lexington, KY, (2017).
14. **Ahmed A. Bahrani**, O. Al-Janabi, D. Wilcock, C. Smith, and G. Jicha, "Semi-Automated Volumetric Quantifying Method of Cerebral Microhemorrhage Using T2*-Weighted MRI Images", American Neurological Association's (ANA) 2018 Annual Meeting, Atlanta, (2018).
15. **Ahmed A. Bahrani**, O. Al-Janabi, D. Wilcock, C. Smith, and G. Jicha "Eliminating the Source of Variability in a Semi-Automated WMH Quantification Method" Alzheimer's Association International Conference, Chicago, (2018).

16. **Ahmed A. Bahrani**, O. Al-Janabi, D. Wilcock, C. Smith, and G. Jicha "WMH Longitudinal Study Analysis using Different Protocols" Alzheimer's Association International Conference, Chicago, (2018).
17. O. Al-Janabi, **Ahmed A. Bahrani**, R. Murphy, P. Nelson, C. Smith, D. Wilcock, G. Jicha," Parietal Lobe Cerebral Microbleeds are Associated with Lower Cerebrospinal Fluid Beta Mayloid$_{1-42}$ in Patients with Sporadic AD" AAIC, Chicago, (2018).
18. O. Al-Janabi, C. Brown, **Ahmed A. Bahrani**, R. Murphy, B. Gold, P. Nelson, D. Wilcock, L. Goldstein, C. Smith, G. Jicha," Amyloid and Hypertension are Independently Associated with White Matter Injury Assessed by FLAIR and DTI MRI", AAN, CA, (2018).
19. O. Al-Janabi, **Ahmed A. Bahrani**, R. Murphy, P. Nelson, C. Smith, D. Wilcock, G. Jicha," Distinct Spatial Distribution of White Matter Hyperintensities Associated with Alzheimer's Disease Pathology and Hypertension", AAN, CA, (2018).
20. **Ahmed A. Bahrani**, O. Al-Janabi, Guoqiang Yu, Donna M. Wilcock, Charles D. Smith, and Gregory A. Jicha, "Cerebral Microhemorrhage Volumetric Method using Susceptibility Weighted Imaging", UK CCTS Spring Conference, Lexington, KY, (2018).
21. L. Wong, M. Zhao, C. Huang, N. Agochukwu, S. Mazdeyasna, **Ahmed A. Bahrani**, L. Chen, J. Radabaugh, R. Aouad, G. Yu, "Perioperative Optical Assessment of Blood Flow Variations in Soft Tissues: Implications for Assessment & Management of Battlefield Injuries", Military Health System Research Symposium, Kissimee, FL, (2018).
22. S. Mazdeyasna, C. Huang, M. Zhao, **Ahmed A. Bahrani**, N. Agochukwu, L. Wong, G. Yu, Noncontact 3Dimensional Speckle Contrast Diffuse Correlation Tomography of Tissue Blood Flow Distribution, UK Markey Cancer Research Day, Lexington, KY, (2018).
23. T. Sudduth, E. Abner, R. Kryscio, S. Cheng, L. Goldstein, F. Schmitt, O. Al-Janabi, **Ahmed A. Bahraini**, P. Nelson, C. Smith, B. Gold, G. Jicha, D. Wilcock, "Assessment of Plasma and CSF for Angiogenic and Inflammatory Proteins in a

Clinical Cohort of Vascular Cognitive Impairment and Dementia Reveal Potential Biomarkers of Disease Severity", AAIC, LA, (2019).

24. **Ahmed A. Bahrani**, D. Rose, M. Mohtasebi, O. Al-Janabi, X. Liu, G. Jicha, G. Yu "Diffuse Correlation Spectroscopy for Investigating Cerebral Amyloid Angiopathy in Elderly Population: Pilot Study", CCTS, KY, (2019).
25. C. Brown, O. Al-Janabi, **Ahmed A. Bahrani**, N. Johnson, D. Powell, C. Smith, G. Jicha, B. Gold, "Network-Dependent Effects of Alzheimer's Pathology and Cerebrovascular Risk on White Matter Decline", CCTS, KY, (2019).
26. O. Al-Janabi, C. Bauer, C. Rupareliya, **Ahmed A. Bahrani**, L. Goldstein, R. Murphy, C. Smith, D. Wilcock, G. Jicha, B. Gold, "WMH Progression but not Regression is Associated with a Higher CSF tau/Aβ and Temporal Amyloid Concentration in The Amyloid PET Scan (P5. 1-031)", Neurology Supplement, 92(14), (2019).

Ahmed A. Bahrani.